Swansea University
Prifysgol Abertawe

HADRONS UNDER EXTREME CONDITIONS

By

Dawid L. Stasiak

Submitted to Swansea University
in fulfilment of the requirements for the Degree of
Doctor of Philosophy

January 2023

Abstract

At high temperature and density, strongly interacting matter experiences a phase transition from a hadronic phase to a quark-gluon plasma. Heavier hadrons are able to survive longer inside the quark-gluon plasma, but their properties change as they approach deconfinement. This thesis aims to investigate the onset of deconfinement and the properties of heavy hadrons as they approach this state, with a particular focus on baryons under extreme conditions. The research will utilise non-relativistic potential models and will build upon the method of Silvestre et al. (2020) [1], which utilises a variational approach to solve three-body potential models through expansion of the wave function in a simple harmonic oscillator basis. The project will also extend this method to solve spin-dependent baryon models. The main focus of this thesis is the application of this method to temperature-dependent baryon potential models. To this end, we will solve two such models that include a spin-spin interaction term. We find that the masses of heavy baryons decrease as temperature is increased, less so for the heavier baryons, for the heaviest baryons Ω_{bbb} we found its mass to actually increase as temperature was increased. We have also used our method to predict the dissociation points of some heavy baryons and have found that heavier baryons are able to survive for longer, as temperature is increased. Furthermore, all baryons grow quickly in size as temperature is increased, reaching infinite size at criticality.

This work has not previously been accepted in substance for any degree and is not being concurrently submitted in candidature for any degree.

- **Signed:** Dawid L. Stasiak
- **Date:** 3rd[rd], January 2023

This thesis is the result of my own investigations, except where otherwise stated. Other sources are acknowledged by giving explicit references. A bibliography is appended.

- **Signed:** Dawid L. Stasiak
- **Date:** 3[rd], January 2023

I hereby give consent for my thesis, if accepted, to be available for photocopying and for inter-library loan, and for the title and summary to be made available to outside organisations.

- **Signed:** Dawid L. Stasiak
- **Date:** 3[rd], January 2023

The University's ethical procedures have been followed and, where appropriate, that ethical approval has been granted.

- **Signed:** Dawid L. Stasiak
- **Date:** 3[rd], January 2023

Table of Contents

ACKNOWLEDGEMENTS

There are numerous people I would like to offer my thanks to, without whom this work would not have been possible:

To my supervisors, Prof. Gert Aarts and especially Dr. Timothy Burns for all his support and guidance over the last 4 years. Whose knowledge and advice has been invaluable for the work presented in this thesis.

To those closest to me, in particular, my mother Justyna Stasiak and my girlfriend Alina Pietruszewicz for their ongoing support.

Last but not least, I would like extend my thanks to all my friends who have made this entire experience enjoyable and worthwhile, especially Sergio Chaves García-Mascaraque, Paula Baliña Vieites and Mohammad Akhond.

I dedicate this work to mum

Justyna Stasiak.

List of Tables

List of Figures

Conventions

$\hbar = c = k_B = 1$

Acronyms

QCD - Quantum Chromo Dynamics

SHO - Simple Harmonic Oscillator

w.f(s). - wave function(s)

r.m.s. - root mean square

c.o.m. - centre of mass

Eq. - Equation

Sec. - Section

Ch. - Chapter

Fig. - Figure

Tab. - Table

1 Introduction

Hadrons are a class of subatomic particles that are composed of quarks and antiquarks. Although hadrons come in many different shapes and flavours, they mainly fall into one of two categories: baryons or mesons. Baryons are made up of three quarks, while mesons are made up of a quark and an antiquark. In this thesis, we will study hadrons under extreme conditions using non-relativistic potential models.

1.1 Potential Models and Quantum Field Theories

Potential models are mathematical representations of quantum mechanical systems. In general, they are based on the principles of quantum mechanics. They are an essential tool for understanding the behaviour of quantum mechanical systems and for predicting their properties. Potential models are, as the name suggests, models, usually, of an underlying quantum field theory, QCD in the case of strong interactions, and are often adapted to fit phenomenological results [2].

In particle physics, potential models and quantum field theories are used for slightly different purposes. Quantum field theories provide a more comprehensive and fundamental description of physical systems and are used to better understand the standard

model of particle physics and to explore new phenomena. Potential models, on the other hand, are simpler models that are often used to compliment QFT results or for phenomenology, such as analysing experimental data from particle collisions and predicting the energy spectra of excited hadron states, something QCD currently struggles with [3]. While potential models can be useful tools, they have their limitations and are not able to capture all of the phenomena described by quantum field theories.

1.2 Introduction to Hadron Potential Models

In the early 1970s, numerous authors used the principles of QCD along with phenomenological considerations to devise the form of a strongly interacting potential between a quark and an antiquark [4–6]. Since then, the most widely adapted non-relativistic potential model for describing the strong force is the Cornell potential. In its most basic form, the Cornell potential is a combination of a Coulomb type term and a linear term

$$V_{\text{Cornell}}(r) = -\frac{\alpha}{r} + \sigma r, \tag{1.1}$$

with r being the relative distance between the quark-antiquark pair. In the Cornell potential model, the linear term shown in Eq. (1.1) models the confinement of quarks. The linear term captures the effect of the attraction between quarks which increases with increasing separation. When two quarks are forced to separate, the energy stored up by the strong force will eventually reach a point where a new quark-antiquark pair can be created, effectively resetting the process. Currently, the only way to detect lone quarks is through indirect measurements of the quark gluon plasma where lone quarks roam freely. The potential between two quarks, rather than between a quark and an antiquark can be modelled by a potential similar to that of the Cornell potential, with the difference being a multiplicative factor in front of the potential which is called the colour factor. This factor, when calculated comes out to be 1/2. So, when we will be

dealing with baryons, we will have to use the appropriate potential which models the force between quarks, as opposed to mesons where the appropriate potential is given by Eq. (1.1).

Potential models have initially been used to study the heavy quarkonia, particularly focusing on the J/Ψ ($c\bar{c}$) and Υ ($b\bar{b}$) mesons, as the mass of their constituent particles is large enough, relative to the Λ_{QCD} scale, so that they are less dependent on relativistic effects and can be studied using simple non-relativistic potential models. The J/Ψ meson, with its relatively low mass, was of particular interest as it could be produced in early particle collision experiments, allowing for a comparison with predictions from simple non-relativistic potential models [5, 7] which are based on the Cornell potential shown in Eq. (1.1). Subsequently, other authors [7–10], used non-relativistic potential models to obtain observables of other mesons like the $b\bar{b}, t\bar{t}$ and even attempted to obtain observables of lighter mesons such as the $s\bar{s}$ states.

The second advancement in potential models was the addition of hyperfine corrections to non-relativistic models, some works can be found in Refs. [10–16]. Another step forward was the addition of relativistic corrections, which allowed for the study of lighter mesons and also more accurate study of the heavier states, these can be found in Refs. [17–21], some of which also include hyperfine interactions. As a result of these efforts, potential models have covered a large portion of the mesonic sector, potential models are able to predict the masses of most known mesons to a great detail where some models are only few MeVs shy off experimental meson masses, see for example Refs. [20, 21].

However, new hadrons are constantly being detected and better experimental results of current known hadrons are being produced, see Ref. [22] for example. One of the struggles of detecting particles is that although their mass can be determined, identifying their quantum numbers can sometimes be a challenge. In some cases potential models can be used to provide candidates for the detected particles. This has been done in the past, for example in Ref. [7], Eichten et al. (1979) used a

simple potential model to provide the candidates for the discovered $\psi'(3772)$ state whose mass was close to their predicted mass of 3.81 GeV for the 1D $c\bar{c}$ state. On top of that, Eichten et al. also computed the masses of various bottomonium states although no experimental results for the bottomonium states yet existed at the time. An example of a more recent challenge can be found in Ref. [23].

With such a large body of work around potential models, many different methods have been developed for solving them numerically. Some of the techniques have been mentioned in the introduction of Ref. [1] and although they were presented as techniques used to solve three-body potential models, same techniques can also used to solve two-body models. The numerical techniques mentioned are; quantum Monte Carlo method, Faddeev equations, hyperspherical formalism, stochastic variational method and expansion on orthogonal bases, for example harmonic oscillator (OH), where the last is the technique that we will be using to solve two and three-body potential models. We would also like to add the Gaussian expansion method to the list of techniques used to numerically solve potential models [23]. We note that, no one method is better as they have their advantages and disadvantages, for a short review see introduction of Ref. [1].

In a similar fashion as with mesons, there also exist many potential models used to study baryons. Although these were developed slightly later due to lesser initial interest and increased complexity of solving a baryon potential model, as it is a three-body problem. But just like for mesons, there exist naive baryon potential models which do not take into account relativistic nor hyperfine corrections, for example Ref. [2]. Then, there are also baryon models which include hyperfine corrections [1, 24–31]. Finally, models which consider relativistic corrections can be found in Refs. [32–34]. As such, there exists a vast body of literature devoted to studying baryons at zero-temperature using potential models. Similarly as for mesons, potential models are still being used to-date to analyse experimental results of detected baryons, see [23] for example.

During experiments, detectors are only able to directly study/detect Hadrons that have been ejected from the centre of collision and have had time to cool down. This means that our understanding of Hadrons at zero-temperature is more detailed than of hadrons at finite temperatures, as no direct probes currently exist for studying the dynamics of hadrons inside the quark-gluon plasma, we are thus forced to resort to indirect measurements of the QGP through processes such J/Ψ suppression, which will be discussed in the next section. Throughout the years, potential models served and continue to serve as great tools for identifying the detected particles in particle collision experiments. This is done based on analysis of quantum numbers and binding energies of detected particles and comparing them with the predictions of potential models. The Particle Data Group (PDG) currently holds data on hundreds of hadrons (mesons and baryons), storing various properties such as their mass, decay modes and many other properties. On the contrary, the PDG currently holds no information about the behaviour of hadrons at finite temperature, i.e. how their mass changes as a function of temperature or when certain hadrons become deconfined. This is because, the effects of temperature on hadrons are still in their exploration phase, many models and predictions do exist and efforts are being made to better understand the dynamics of hadrons under such extreme conditions.

1.3 Hadrons at Finite Temperature

One of the focuses in high energy particle physics, is on understanding the properties of hadrons at finite temperature and the mechanisms behind their phase transition. At finite temperature, quantum chromodynamics (QCD), predicts that hadrons undergo a phase transition from a hadronic phase, in which they are bound by the strong nuclear force, to a quark-gluon plasma phase, in which they are deconfined [35]. This phase transition has been studied through a variety of experimental and theoretical approaches, including lattice QCD simulations [36–40] and heavy-ion collision exper-

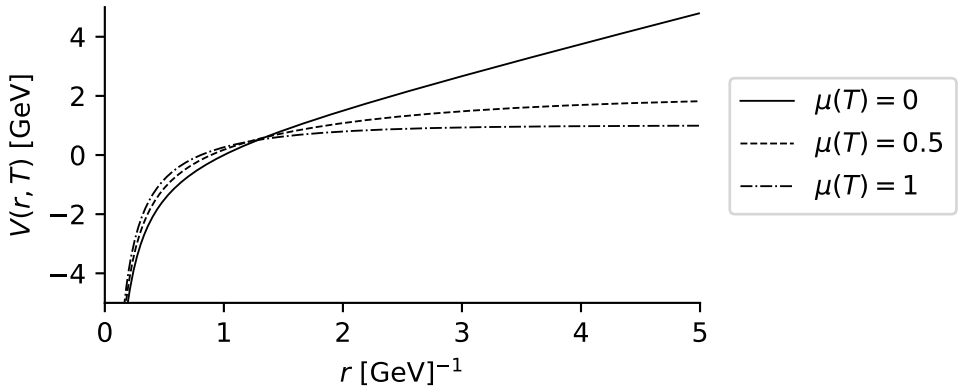

Figure 1.1: Plot of a screened quark-antiquark potential from Ref. [52] shown at different values of screening mass $\mu(T)$.

iments [41–47].

In 1986, Matsui and Satz first proposed a reliable probe for detecting the quark gluon plasma in particle collision experiments through the mechanism of J/ψ suppression [48]. The probe is based on the idea that at sufficiently high energies, the production rate of the J/ψ particle will be suppressed in the presence of a quark-gluon plasma, leading to a suppression of its production which can be detected in an experiment. A series of experiments were conducted to measure the predicted suppression and less than a year after their publication, J/ψ suppression has been observed at CERN [49, 50], suggesting the formation of a quark-gluon plasma.

The basic mechanism responsible for deconfinement of hadrons present in a dense and hot medium of quarks and gluons is the Debye screening of the quark colour charge [51]. Quarks become deconfined when the screening radius r_D becomes smaller than their binding radius r_H, i.e., smaller than the hadron radius [48].

Lattice QCD simulations can be used to motivate the form of a temperature dependent interquark potential, some examples include [52–56]. Those allow us to study hadrons at non-zero temperatures using potential models. Lattice QCD simulations find that the linear part of the potential between two quarks flattens when the bound state is present in a dense, strongly interacting medium at a high temperature. There

exist various parameterisations for the flattening of the potential due to the effects of colour charge screening. Karsch et al. (1988) propose one such parameterisation in Ref. [52], which has been illustrated in Fig. 1.1 for different values of the screening mass $\mu(T) = 1/r_D(T)$ (an effective temperature parameter).

The study of mesons at finite temperature via potential models has started relatively early, with one of the pioneering papers being the one by Karsch et al., (1988) [52], after which, more studies of mesons at finite temperature followed, some examples include [57–59]. However, a similar investigation for baryons only began recently. The only two publications that we have encountered in this area is the work by Peng Cheng et al., (2018) [60] where they have used the Gaussian expansion method to study the dissociation of nucleons. The second paper that has been found was by Abu Shady et al., (2020) [61] who use the Nikiforov-Uvarov method to study the dissociation of nucleons and heavy baryons but in an anisotropic hot and dense QCD medium. Our methods focus on isotropic media and on using the method of expanding the wavefunction on a SHO basis, which we will detail in future chapters.

1.4 Summary

In this work, we aim to expand the scope of research of baryons at finite temperature through the use of potential models. We will study baryons through two different temperature dependent potential models, previously only applied to study mesons at finite temperatures. For our numerical approach, we will use the variational method, which involves expanding the system's wavefunction on the SHO basis. During the development of our method, Silvestre et al. (2020) independently developed the same technique for solving three-body systems [1]. We will highlight some of the similarities and differences between our approaches in more detail in Ch. 4 and 6. Silvestre et al., used their technique to solve two different baryon potential models detailed in [14] and

[18] with the latter containing both a non-relativistic and a semi-relativistic baryon model. All models were spin-independent and dealt with baryons at zero temperature. In our work we will use techniques developed in [1] with slight differences to solve two different temperature-dependent and spin-dependent baryon potential models.

In summary, the achievement of this work will be two-fold. Firstly, will be using the techniques outlined by Silvestre et al. in [1] to solve two temperature-dependent baryon potential models. Secondly, we will be building upon the work in Ref. [1] by extending it to spin-dependent potentials.

This work is divided into 10 chapters, with the first one being the introduction. In Chapter 2, we will discuss the main difficulty of solving a three-body problem using the variational method. We will also introduce some general concepts and techniques used throughout this work, such as the variational method, the Jacobi coordinates, the SHO basis for two and three-body systems. We will also describe a method used to simplify the form of the two and three-body Hamiltonians as well as provide analytical solutions for relevant matrix elements of various operators encountered in our work. In Chapter 3, we will solve a two-body meson potential model with hyperfine interaction terms treated perturbatively and compare our results with literature. In Chapter 4, we will introduce the Talmi-Moshinsky transformations and describe how we can use them to obtain a matrix representation of a three-body potential. In Chapter 5, we will test our method for solving three-body potential models by solving the three-body simple harmonic oscillator, which can be solved analytically. This will serve as a benchmark for our numerical method. In Chapter 6, we will describe the procedure for obtaining symmetrized coupled SHO basis sets for solving the baryon potential model. In Chapter 7, we will solve the first baryon model proposed by Silvestre (1996) in Ref. [2] using the variational method and compare our results. In Chapter 8, we will solve two temperature-dependent meson potentials: a simple one motivated by a temperature-dependent string tension, and a more complex one proposed and solved by Karsch et al. (1988) [52]. In Chapter 9, we will use the temperature-dependent interquark potentials from Chapter 8 to motivate and solve two baryon models at

finite temperature. Finally, in Chapter 10 we will conclude our findings.

2

Overview of the Method

In this chapter, we will go over some of the general concepts, equations and operators which we will be using throughout this work. We will give details of our method for numerically solving the Schrödinger equation, namely the variational method. We will provide details of the basis wavefunctions used for solving the two and three-body systems as well as discuss the main issue when solving a three-body problem with this method. We will also give matrix representations of some of the key operators encountered in this work and more.

2.1 The Variational Method

In this section, we will describe the variational method as a tool for numerically solving the Schrödinger equation,

$$H|\Psi_i\rangle = E_i|\Psi_i\rangle. \tag{2.1}$$

The Schrödinger equation can be used to determine the spectrum of the model/system. A quantum mechanical system can be found in different states $|\Psi_i\rangle$ with energies E_i which are the eigenstates and eigenvalues of the Hamiltonian H, respectively. Mathe-

matically, the Schrödinger equation is a partial differential equation and unfortunately lacks analytical solutions for many potentials of interest. As a result, we must rely on numerical approximations to find its solutions.

There exist various methods for solving the Schrödinger equation numerically, the method we have chosen in this project is the variational method. The variational method is discussed by Griffiths and Schroeter in their book "Introduction to Quantum Mechanics" [62]. In this section, we will give the basic idea of the method.

Fundamentally, the variational method is based on guessing a trial wavefunction $|\tilde{\Psi}_i\rangle$ for a system in question, which is approximated using a linear combination of appropriate basis functions and a set of adjustable parameters called variational parameters, sometimes referred to as size parameters as they often determine the size of the basis functions. These parameters can be adjusted until the energy $\tilde{E}_i$ of the trial wavefunction is minimised [62]. The resulting trial wavefunction and its corresponding energy are approximations to the exact wavefunction and its energy. In general, the numerical value of of the energy will be equal or higher than the "true" energy of the system [62]. The energy will only be equal in the special cases where either the basis functions used, perfectly represent the system. For example, using the SHO basis functions to study the SHO quantum system would yield the exact energy of the system that would match the analytical result, we will show this in Ch. 5. If the basis functions do not perfectly represent the system but satisfy the completeness relation then the predicted energy will lie above the true energy of the system. In this case, we would only be able to obtain the exact energy if we utilise all the basis functions but unfortunately there are an infinite amount of them.

In this section, we will use the *tilde* symbol to denote approximations to the exact quantities. We can always expand the trial wavefunctions in a basis which form a complete set $\sum_{j=1}^{\infty} |\phi_j\rangle\langle\phi_j| = 1$, where $|\phi_j\rangle$ are placeholders for a generic basis wavefunction, with j representing a generic label for all the quantum numbers describing the basis state. We can represent a trial wavefunction in terms a of a truncated set

of basis functions, as follows:

$$|\tilde{\Psi}_i\rangle = \sum_{j=1}^{N_\phi} |\phi_j\rangle\langle\phi_j|\Psi_i\rangle, \tag{2.2}$$

where in the limit as $N_\phi \to \infty$, we recover $|\tilde{\Psi}\rangle \to |\Psi\rangle$. In Eq. (2.2), $\langle\phi_n|\Psi_i\rangle$ are the expansion coefficients and N_ϕ is the number basis functions used for the approximation, the larger the N_ϕ the better is the approximation. Due to limited computing power we can only consider a finite number of basis functions. Therefore, the degree of the approximation will depend on the number of basis functions used for the approximations and the choice of the size parameters of the basis functions.

Given the expansion in Eq. (2.2), the Schrödinger equation (2.1) becomes

$$\sum_{j=1}^{N} \langle\phi_{j'}|H|\phi_j\rangle\langle\phi_j|\Psi_i\rangle = E_i\langle\phi_{j'}|\Psi_i\rangle, \tag{2.3}$$

with $\langle\phi_{j'}|\phi_j\rangle = \delta_{j'j}$, i.e. the basis is orthonormal. The matrix representation of the Schrödinger equation in a generic basis $|\phi\rangle$ is given as:

$$\begin{pmatrix} \langle\phi_1|H|\phi_1\rangle & \langle\phi_1|H|\phi_2\rangle & \dots & \langle\phi_1|H|\phi_N\rangle \\ \langle\phi_2|H|\phi_1\rangle & \langle\phi_2|H|\phi_2\rangle & \dots & \langle\phi_2|H|\phi_N\rangle \\ \vdots & \vdots & \ddots & \vdots \\ \langle\phi_N|H|\phi_1\rangle & \langle\phi_N|H|\phi_2\rangle & \dots & \langle\phi_N|H|\phi_N\rangle \end{pmatrix} \begin{pmatrix} \langle\phi_1|\Psi_i\rangle \\ \langle\phi_2|\Psi_i\rangle \\ \vdots \\ \langle\phi_N|\Psi_i\rangle \end{pmatrix} = E_i \begin{pmatrix} \langle\phi_1|\Psi_i\rangle \\ \langle\phi_2|\Psi_i\rangle \\ \vdots \\ \langle\phi_N|\Psi_i\rangle \end{pmatrix}, \tag{2.4}$$

where the numerical values of the matrix elements $\langle\phi_{j'}|H|\phi_j\rangle$ can be obtained by projecting them onto the appropriate coordinate basis and computing integrals over all space. In section 2.5 we will compute the elements of some relevant operators in the SHO basis and show explicitly solutions to those integrals.

The variational method therefore relies on choosing a complete basis set of wavefunctions $|\phi_j\rangle$ in which we can express the trial wavefunction $|\Psi_i\rangle$, of the system in question. The basis set used to represent $|\Psi_i\rangle$ will be truncated, leading to an

approximated solution.

2.2 The Three-Body Problem

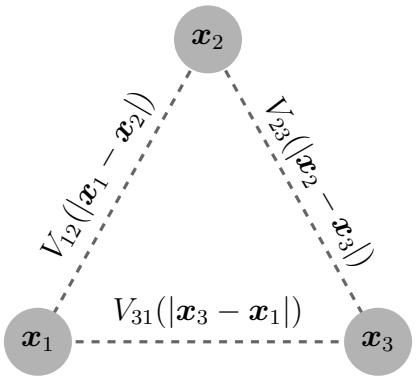

Figure 2.1: A depiction of three particles held together via a pair-wise central potential.

In this section, we will outline the main issues when solving the three-body potential using the variational method. In the two-body case the potential has the form

$$V_{\text{two-body}} = V(|\boldsymbol{x}_1 - \boldsymbol{x}_2|), \tag{2.5}$$

where $\boldsymbol{x}_i$ is the position of the i'th particle. However, in the three-body case we have three terms in the potential, each corresponding to a pair of quarks, i.e.

$$V_{\text{three-body}} = V_{12}(|\boldsymbol{x}_1 - \boldsymbol{x}_2|) + V_{23}(|\boldsymbol{x}_2 - \boldsymbol{x}_3|) + V_{31}(|\boldsymbol{x}_3 - \boldsymbol{x}_1|), \tag{2.6}$$

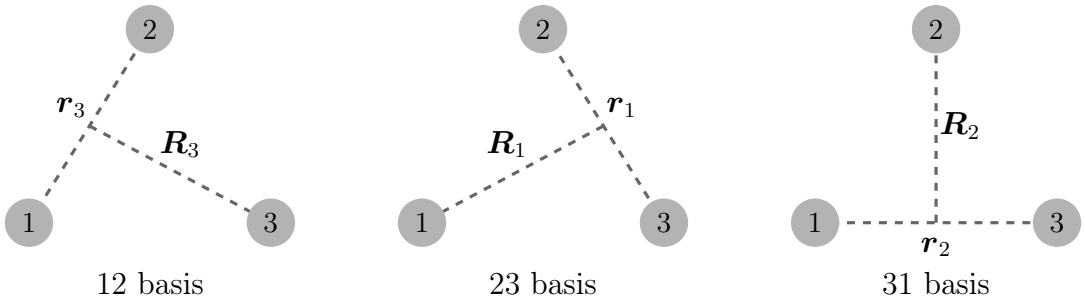

Figure 2.2: Diagram of different choices of basis of the Jacobi coordinates.

as depicted in Fig. 2.1. The problem lies in the fact that we have to choose a preference when defining our coordinate basis. Our choice of coordinates for the three-body problem are the Jacobi coordinates which are defined as follows,

$$\begin{aligned} \boldsymbol{r}_3 &= \boldsymbol{x}_1 - \boldsymbol{x}_2, \\ \boldsymbol{R}_3 &= \frac{m_1\boldsymbol{x}_1 + m_2\boldsymbol{x}_2}{m_1 + m_2} - \boldsymbol{x}_3, \\ \boldsymbol{\mathcal{R}} &= \frac{m_1\boldsymbol{x}_1 + m_2\boldsymbol{x}_2 + m_3\boldsymbol{x}_3}{m_1 + m_2 + m_3}, \end{aligned} \tag{2.7}$$

where m_i is the mass of the i'th particle. Descriptively, $\boldsymbol{r}_3$ is the distance between particles 1 and 2, $\boldsymbol{R}_3$ is the distance between particle 3 and the centre of mass of particles 1 and 2 and $\boldsymbol{\mathcal{R}}$ is the position of the centre of mass of the system. With this choice of Jacobi coordinates, we have expressed a preference for dealing with particles one and two. Using the Jacobi coordinate system, Eq. (2.6) becomes,

$$V_{\text{three-body}} = V_{12}(|\boldsymbol{r}_3|) + V_{23}\left(|\boldsymbol{R}_3 - \frac{m_2}{m_1 + m_2}\boldsymbol{r}_3|\right) + V_{31}\left(|-\boldsymbol{R}_3 - \frac{m_1}{m_1 + m_2}\boldsymbol{r}_3|\right). \tag{2.8}$$

The difficulty when solving the three-body problem arises from the terms V_{23} and V_{31}, even a simple Cornell potential seen before, becomes quite complicated in this basis. Since the basis wavefunctions for the three-body problem also require a commitment to a coordinate basis, we are left with two choices at this stage: Deal with the complicated potential and solve the three-body problem in a single basis or introduce two new frames to simplify the form of the potential at the cost of having to find a

way of expressing SHO basis wavefunctions in the new frames.

In our work and as has been done by Silvestre et al. [1], we choose the latter option where two more Jacobi frames are introduced with each frame preferring a single pair of particles, as shown in Fig. 2.2.

The seemingly strange choice of suffixes is used to ensure that cyclic permutations will hold throughout our equations. Using the newly introduced Jacobi frames, we can now express Eq. (2.8) simply as

$$V_{\text{three-body}} = V_{12}(r_3) + V_{23}(r_1) + V_{31}(r_2), \tag{2.9}$$

which looks much more manageable. But having the potential expressed in three different basis does not solve all our problems. It does allow us to treat each pair of quarks in a consistent manner. What we will find in later chapters is that rather than obtaining a one large matrix representation of the entire potential, we will be able to obtain three separate matrices, one for each term in the potential. Each term will be dealt with in their own Jacobi frame and the problem will very much resemble three copies of the two-body problem, rather than one large three-body problem. We find this approach to the three-body problem to be most pragmatic.

We have mentioned earlier that this method comes at the cost of finding a way of transforming the SHO basis wavefunctions between the different Jacobi frames. This transformation method will be detailed later in chapter 4.

2.3 Basis Functions

In this section, we will describe the complete sets of wavefunctions which we will use for constructing the trial wave function in the two-body and three-body problems.

2.3.1 Two-Body Basis

For the two-body problem in three-dimensional space we will use the simple harmonic oscillator (SHO) wavefunctions as our complete set of basis wavefunctions for constructing the trial wavefunctions. The SHO w.fs. are chosen as the basis not only because they are the standard choice of basis in the field but also this choice of basis is essential for our three-body treatment later on.

The SHO basis functions are obtained by solving the Schrödinger equation for the two-body simple harmonic oscillator potential

$$V_{\rm SHO}(r) = \frac{1}{2}kr^2 = \frac{1}{2}\mu\omega^2 r^2, \tag{2.10}$$

where $r = x_1 - x_2$ is the distance between the two particles and $\mu = \frac{m_1 m_2}{m_1+m_2}$ is their reduced mass, $\omega = (k/\mu)^{1/2}$ corresponds to the classical angular frequency of the oscillator [63]. The potential in Eq. (2.10) is one of very few potentials for which the Schrödinger equation can be solved exactly. The spectrum of the three dimensional isotropic harmonic oscillator in quantum mechanics is given as [63]

$$E_{\rm SHO} = \omega(2n + l + \frac{3}{2}), \tag{2.11}$$

where n is a radial quantum number and l represents the orbital angular momentum.

In our work, we will express the SHO wavefunctions using dimensionless variables

$$\boldsymbol{\rho} \equiv \alpha \boldsymbol{r}, \text{ with } \alpha \equiv \sqrt{\mu\omega}. \tag{2.12}$$

Note, the dimensions of $\boldsymbol{r}$ are GeV^{-1} and the dimensions of $\sqrt{\mu\omega}$ is GeV, making $\boldsymbol{\rho}$ a dimensionless variable. The harmonic oscillator wavefunctions are characterised by three quantum numbers n, l and m where m is the projection of the orbital angular

momentum. Mathematically they can be written as

$$\langle \rho, \theta, \phi | nlm \rangle = \psi_{nlm}(\boldsymbol{\rho}) = R_{nl}(\rho) Y_{lm}(\theta, \phi), \tag{2.13}$$

where $Y_{lm}(\theta, \phi)$ are the well known spherical harmonics and

$$\boxed{\begin{aligned} R_{nl}(\rho) &= c_{nl} \rho^l e^{-\rho^2/2} L_n^{l+1/2}(\rho^2), && \text{(2.14a)} \\ c_{nl} &= \left[\frac{2(n!)}{\Gamma(n+l+3/2)} \right]^{1/2}, && \text{(2.14b)} \\ L_n^{l+1/2}(\rho^2) &= \sum_{k=0}^{n} d_{nlk} \rho^{2k}, && \text{(2.14c)} \\ d_{nlk} &= \frac{(-1)^k \Gamma(n+l+3/2)}{(n-k)! \Gamma(k+l+3/2)(k)!}, && \text{(2.14d)} \end{aligned}}$$

where $L_n^{l+1/2}(\rho^2)$ are the associated Laguerre polynomials and Γ represents the Gamma function. The above expressions will serve as a basis for computing most integrals in this work, and in turn obtaining matrix elements of various operators in both the two and three-body problems.

The SHO wavefunctions form a complete set over the Hilbert space, i.e.

$$\sum_{nlm} |nlm\rangle\langle nlm| = \mathbb{1}, \tag{2.15}$$

and satisfy the following orthonormality conditions

$$\int d\rho \rho^2 R_{nl}(\rho) R_{n'l'}(\rho) = \delta_{n'n}, \tag{2.16}$$

$$\int d\Omega \; Y^*_{lm}(r) Y_{l'm'}(r) = \delta_{l'l} \delta_{m'm}, \tag{2.17}$$

$$\int d\rho \rho^2 \int d\Omega \; \psi^*_{nlm}(\rho, \theta, \phi) \psi_{n'l'm'}(\rho, \theta, \phi) = \delta_{n'n} \delta_{l'l} \delta_{m'm}, \tag{2.18}$$

where $d\Omega \equiv d\theta d\phi \sin\theta$ and the integrals are performed over all space.

Some radial functions have been plotted in Fig. 2.3, to highlight their symmetry

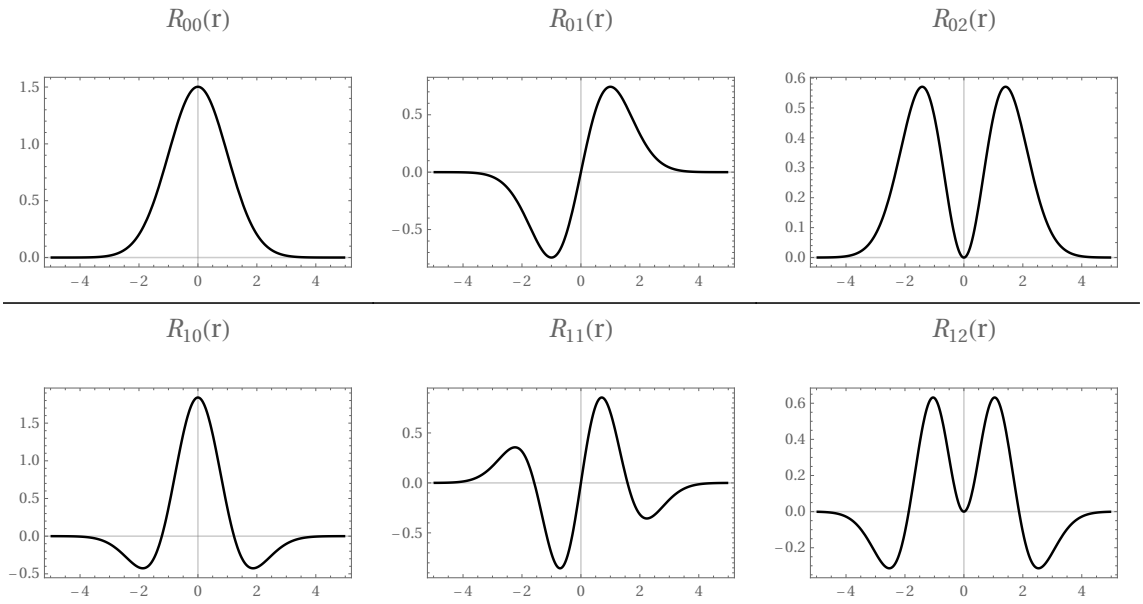

Figure 2.3: Radial functions $R_{nl}(\rho)$, see Eq. (2.14a). The radial functions are symmetric for even l and anti-symmetric for odd l.

properties. In general, they are symmetric(antisymmetric) when l is even(odd) under the transformation $r \to -r$, this will become an important fact later one when we come to Ch. 6.

2.3.2 Three-Body Basis

Since the three-body system is parameterised by the Jacobi coordinates $\boldsymbol{r}, \boldsymbol{R}$, defined in Eq. 2.7, the basis for a three-body system will be constructed from a Clebsch-Gordan sum of coupled SHO wavefunctions, where each SHO function belongs to a single degree of freedom[27],

However, similarly as in the two-body case, we will represent the coupled SHO functions in a dimensionless coordinate basis, therefore, we will introduce

$$\boldsymbol{\rho} \equiv \alpha \boldsymbol{r}, \quad \boldsymbol{\lambda} \equiv \beta \boldsymbol{R}, \tag{2.19}$$

where similarly as in Eq. (2.12) we have

$$\alpha \equiv \sqrt{\mu_r \omega_r}, \quad \beta \equiv \sqrt{\mu_{\rm R} \omega_{\rm R}}. \tag{2.20}$$

The form of μ_r and $\mu_{\rm R}$ will be given in section 2.4.2.

We note that in the two-body case, where each basis function consisted of a single SHO wavefunction, there was only a single size parameter ω. However, in the three-body case, each basis function will consist of *two* coupled SHO wavefunctions, therefore, we will have *two* size parameters ω_r and $\omega_{\rm R}$. Later in Ch. 4 we will restrict the two to be equal, such that $\omega_r = \omega_{\rm R} = \omega$, reducing the number of variational parameters to one.

Finally, the three-body basis functions will have the following form

$$\langle \boldsymbol{\rho}, \boldsymbol{\lambda} | nl, NL : \Lambda M_\Lambda \rangle = \sum_{mM} \langle lm, LM | \Lambda M_\Lambda \rangle \psi_{nlm}(\boldsymbol{\rho}) \psi_{NLM}(\boldsymbol{\lambda}), \tag{2.21}$$

where $\boldsymbol{\Lambda} = \boldsymbol{l} + \boldsymbol{L}$ is the vector sum of the orbital angular momenta coupled to each Jacobi coordinate, combining to give the total orbital angular momentum. The quantities, $\langle lm, LM | \Lambda M_\Lambda \rangle$ are the vector coupling constants otherwise known as, Clebsch-Gordan coefficients, $M_\Lambda = m + M$ and $\psi_{nlm}(\boldsymbol{\rho})$ and $\psi_{NLM}(\boldsymbol{\lambda})$ are the same SHO basis functions as encountered in the two-body problem in Eq. (2.13).

2.4 Two and Three-Body Hamiltonians

In this section, we will give a general description of the two and three-body Hamiltonians used throughout this work for general central potentials. The Hamiltonian for a general N-body system can be constructed by taking into account the total kinetic

and potential energy of the system,

$$H = T + V, \tag{2.22}$$

with T being the total kinetic energy and V the total potential energy. The general form for the kinetic energy of a relativistic N-body system is given as

$$T_{\text{rel}} = \sum_{i=1}^{N_P} \sqrt{m_i^2 + \boldsymbol{p}_i^2}, \tag{2.23}$$

with m_i being the mass of particle i and $\boldsymbol{p}_i$ being its momentum and where N_P is the number of particles in the system. In the non-relativistic limit where $p_i \ll m_i$, Eq. (2.23) can be expanded up to the leading term to give

$$T_{\text{non-rel}} = \sum_{i=1}^{N_P} \left[m_i + \frac{\boldsymbol{p}_i^2}{2m_i} \right]. \tag{2.24}$$

In this study, we will focus exclusively on non-relativistic models. This choice restricts our analysis to heavy hadrons that possess at least one charm quark or a quark of greater mass. The utilisation of non-relativistic models in investigating baryons at finite temperature can be supported by our primary interest in observing general trends and patterns within three-body temperature-dependent potential models. Additionally, we aim to develop a technique for solving three-body systems with hyperfine interactions using the variational method.

Although future investigations using relativistic potentials and more intricate temperature dependent potentials to achieve high precision results are worthwhile, it is currently justifiable to employ the non-relativistic approach. This is due to the absence of experimental data or high precision lattice QCD data for result comparison at this early stage of exploring baryons at finite temperature. Nonetheless, the techniques developed here pave the way for potential future exploration into the realm of high precision results using more intricate potential models.

From now on we will refer to $T_{\text{non-rel}}$ simply as T to save unnecessary notation. A general central potential for an N-body system is given as

$$V = \sum_{i<j}^{N_P} V(|\boldsymbol{x}_i - \boldsymbol{x}_j|), \tag{2.25}$$

where $\boldsymbol{x}_i$ is the particle position and N_P is number of particles. The sum then goes over all pairs of particles in the system, i.e., in a two-body system, there is only one pair of particles and in the three-body system there are three pairs, and so on.

2.4.1 Two-Body Hamiltonian

In this section, we will detail the form of the Hamiltonian for a two-body system sitting in a central potential. Moreover, we will use the fact that we are using SHO wavefunctions as the basis for finding the trial wavefunction $|\Psi\rangle$ to simplify the form of the two-body Hamiltonian.

Using Eq. (2.24) and (2.25), the two-body Hamiltonian can be expressed as

$$H_{\text{two-body}} = \sum_{i=1}^{2} \left[m_i + \frac{p_i^2}{2m_i} \right] + V(|\boldsymbol{x}_1 - \boldsymbol{x}_2|). \tag{2.26}$$

To simplify the Hamiltonian in Eq. (2.26), we will switch to Jacobi coordinates for two-bodies by performing a variable substitution where $\boldsymbol{r} = \boldsymbol{x}_1 - \boldsymbol{x}_2$ and $\boldsymbol{\mathcal{R}} = \frac{m_1\boldsymbol{x}_1 + m_2\boldsymbol{x}_2}{m_1+m_2}$, which is the centre of mass coordinate. We will also be working in spherical coordinates where $\boldsymbol{r} = \{r, \theta, \phi\}$. On top of that, we will choose the centre of mass of the system as our frame of reference, this yields us the following

$$H_{\text{two-body}} = \sum_{i=1}^{2} m_i + \frac{\boldsymbol{p}_r^2}{2\mu} + V(r), \tag{2.27}$$

where

$$\mu = \frac{m_1 m_2}{m_1 + m_2}. \tag{2.28}$$

Note that the centre of mass (c.o.m.) motion has been eliminated. To simplify Eq. (2.27), we can now take advantage of the fact that we use the SHO basis wavefunctions $|nlm\rangle$ as a basis for representing the trial wavefunction $|\Psi\rangle$. The spectrum of a three-dimensional isotropic harmonic oscillator is given as [63]

$$[T + V_{\text{SHO}}]|nlm\rangle = \omega(2n + l + \tfrac{3}{2})|nlm\rangle, \tag{2.29}$$

with V_{SHO} defined in Eq. (2.10). Using (2.29) we can write,

$$\begin{aligned} T|nlm\rangle &= [T + V_{\text{SHO}} - V_{\text{SHO}}]|nlm\rangle \\ &= [\omega(2n + l + \tfrac{3}{2}) - V_{\text{SHO}}]|nlm\rangle, \end{aligned} \tag{2.30}$$

allowing us to write the Hamiltonian in Eq. (2.27) as

$$\boxed{H_{\text{two-body}} = \sum_{i=1}^{2} m_i + \omega(2n + l + \tfrac{3}{2}) - \tfrac{1}{2}\mu\omega^2 r^2 + V(r),} \tag{2.31}$$

where we have effectively substituted

$$\frac{\boldsymbol{p}_r^2}{2\mu} \longleftrightarrow \omega(2n + l + \tfrac{3}{2}) - \tfrac{1}{2}\mu\omega^2 r^2. \tag{2.32}$$

2.4.2 Three-Body Hamiltonian

In a series of similar steps as (2.26) → (2.27) and using the Jacobi coordinates defined in Eqs. (2.7) to parameterise the three-body system, we can obtain

$$H_{\text{three-body}} = \sum_{i=1}^{3} m_i + \frac{\boldsymbol{p}_r^2}{2\mu_r} + \frac{\boldsymbol{p}_{\text{R}}^2}{2\mu_{\text{R}}} + V_{12}(r_3) + V_{23}(r_1) + V_{31}(r_2), \tag{2.33}$$

with,

$$\mu_r = \frac{m_1 m_2}{m_1 + m_2}, \text{ and } \mu_{\rm R} = \frac{m_3(m_1 + m_2)}{m_1 + m_2 + m_3}. \tag{2.34}$$

Note that the centre of mass motion has been implicitly set to zero and therefore there are only two terms for the kinetic energy. Using the same trick as in the two-body case (Eq. (2.32)), to replace the $\frac{\boldsymbol{p}^2}{2\mu}$ operators in the three-body Hamiltonian with the spectrum of a simple harmonic oscillator, we have

$$\boxed{\begin{aligned} H_{\text{three-body}} = \sum_{i=1}^{3} m_i &+ \omega_r(2n + l + \tfrac{3}{2}) - \tfrac{1}{2}\mu_r\omega_r^2 r^2 \\ &+ \omega_{\rm R}(2N + L + \tfrac{3}{2}) - \tfrac{1}{2}\mu_{\rm R}\omega_{\rm R}^2 R^2 \\ &+ V_{12}(r_3) + V_{23}(r_1) + V_{31}(r_2). \end{aligned}} \tag{2.35}$$

Note that in a special case when the potential between particles takes the form of the simple harmonic oscillator, the Hamiltonian can be reduced to

$$H^{\text{SHO}}_{\text{three-body}} = \sum_{i=1}^{3} m_i + \omega_r(2n + l + \tfrac{3}{2}) + \omega_{\rm R}(2N + L + \tfrac{3}{2}), \tag{2.36}$$

which is exactly the energy of a three-body harmonic oscillator. We will revisit this in more detail in Ch. 5.

2.5 Operators in the SHO basis

In this section, we will obtain expressions of matrix elements for relevant operators in the SHO basis. Since we are dealing with central potentials only, we will not encounter operators dependent on the angular degrees of freedom θ or ϕ, except for the $\delta(\boldsymbol{r})$ operator which will be treated as an isolated special case. As such, we will first give a solution to a general r dependant operator and later obtain explicit solutions to specific operators found in the two and three-body systems.

The element of a general operator $\mathcal{O}(r)$ in the SHO basis can be obtained by by computing the integral

$$\langle n'l'm'|\mathcal{O}(r)|nlm\rangle = \int_0^\infty d\rho\rho^2 R_{n'l}(\rho)\mathcal{O}(\frac{\rho}{\alpha})R_{nl}(\rho)\delta_{l'l}\delta_{m'm}, \tag{2.37}$$

where we have used the orthogonality of the spherical harmonics to obtain the delta functions. Note that on the right hand side, we have expressed the operator in the dimensionless coordinate basis so that we can perform the integration.

2.5.1 The Constant Operator

The constant operator will be important as there exist different constant operators, such as the quark mass m_i or other constant terms added to a potential. We will represent a general constant with the parameter c. We can use Eq. (2.37) to obtain the matrix element of c in the SHO basis giving us

$$\langle n'l'm'|c|nlm\rangle = c\delta_{n'n}\delta_{l'l}\delta_{m'm}, \tag{2.38}$$

which is simply the identity matrix multiplied by the constant c,

$$\hat{c} = c\begin{pmatrix} 1 & 0 & 0 & \dots & 0 \\ 0 & 1 & 0 & \dots & 0 \\ \vdots & \vdots & \vdots & \ddots & \vdots \\ 0 & 0 & 0 & \dots & 1 \end{pmatrix}. \tag{2.39}$$

Therefore, any constant term in the Hamiltonian will have a similar representation, it will consist of the identity matrix multiplied by the constant.

2.5.2 The r^y Operator

This operator will appear in all potential models encountered in this work, in multiple forms. The Cornell potential in Eq. (1.1) alone contains an r^{-1} term and a linear term r. Furthermore, we have seen the r^2 term appear in both the two and three-body Hamiltonians in Eqs. (2.31) and (2.35). Therefore, we will aim to obtain the general form for the element of an r^y operator with $y \in \mathbb{R}$. Using Eq. (2.37) we have

$$\langle n'l'm'|r^y|nlm\rangle = \int_0^\infty d\rho\rho^2 R_{n'l}(\rho)\frac{\rho^y}{\alpha^y}R_{nl}(\rho)\delta_{l'l}\delta_{m'm}, \tag{2.40}$$

Using the definition of $R_{nl}(\rho)$ given in Eq. (2.14a). we can rewrite (2.40) as

$$\langle n'l'm'|r^y|nlm\rangle = \frac{1}{\alpha^y}c_{n'l}c_{nl}\sum_{k',k=0}^{n',n} d_{n'lk'}d_{nlk}\int_0^\infty d\rho\ \rho^{2p+2+y}e^{-\rho^2}\delta_{l'l}\delta_{m'm}, \tag{2.41}$$

where $p = k' + k + l$. Rewriting the sums in terms of k and p one obtains,

$$\langle n'l'm'|r^y|nlm\rangle = \frac{1}{\alpha^y}c_{n'l}c_{nl}\sum_{p=l}^{l+n'+n}\sum_{k} d_{n'lp-k-l}d_{nlk}\int_0^\infty d\rho\ \rho^{2p+2+y}e^{-\rho^2}\delta_{l'l}\delta_{m'm}, \tag{2.42}$$

where the limits on k are $\{\mathrm{Max}[0, p-l-n'], \mathrm{Min}[n, p-l]\}$. The integral in Eq. (2.42) can be looked up in Ref. [64], the solution to that integral is given as

$$\int_0^\infty d\rho\ \rho^{2p+2+y}e^{-\rho^2} = \Gamma(p + \tfrac{1}{2}y + \tfrac{3}{2}). \tag{2.43}$$

The final equation reads:

$$\boxed{\langle n'l'm'|r^y|nlm\rangle = \frac{1}{\alpha^y}c_{n'l}c_{nl}\sum_{p,k} d_{n'lp-k-l}d_{nlk}\Gamma(p + \tfrac{1}{2}y + \tfrac{3}{2})\delta_{l'l}\delta_{m'm}.} \tag{2.44}$$

2.5.3 The Exponential Operator

This operator will appear in a temperature-dependent model given by Karsch et al. [52]. And since we will encounter it multiplied by the r operator, what we are interested in is the general operator,

$$\mathcal{O}(r) = r^y e^{-\xi r} = \frac{\rho^y}{\alpha^y} e^{-\frac{\xi}{\alpha}\rho}, \tag{2.45}$$

for $y \in \mathbb{R}$ and with $\xi > 0$ being a positive scaling parameter. Using Eq. (2.37) we have

$$\langle n'l'm'|r^y e^{-\xi r}|nlm\rangle = \frac{1}{\alpha^y} c_{n'l} c_{nl} \sum_{p,k} d_{n'lp-k-l} d_{nlk} \int_0^\infty d\rho \rho^{2p+2+y} e^{-\rho^2 - \frac{\xi}{\alpha}\rho} \delta_{l'l} \delta_{m'm}. \tag{2.46}$$

The integral in the above equation has an analytical solution that can be looked up in Ref. [64]. For the particular form here, the solution is given as:

$$\int_0^\infty d\rho \rho^{2p+2+y} e^{-\rho^2 - \frac{\xi}{\alpha}\rho} = 2^{-(\frac{2p+3+y}{2})} \Gamma(2p+3+y) e^{\frac{\xi^2}{8\alpha^2}} D_{-(2p+3+y)}(\tfrac{\xi}{\sqrt{2}\alpha}), \tag{2.47}$$

where $D_\nu(z)$ are the Parabolic Cylinder functions D. Combining these equations one gets

$$\langle n'l'm'|r^y e^{-\xi r}|nlm\rangle = \frac{1}{\alpha^y} e^{\frac{\xi^2}{8\alpha^2}} c_{n'l} c_{nl} \sum_{p,k} d_{n'lp-k-l} d_{nlk} (2^{-\frac{2p+3+y}{2}}) \Gamma(2p+3+y) D_{-(2p+3+y)}(\tfrac{\xi}{\sqrt{2}\alpha}) \delta_{l'l} \delta_{m'm}. \tag{2.48}$$

2.5.4 The Gaussian Operator

The Gaussian operator will be found in a hyperfine interaction term conjugate to the spin-spin term in a potential given by Silvestre [2] which we will aim to solve. In general, this operator can be written as

$$\mathcal{O}(r) = e^{-\sigma^2 r^2}, \tag{2.49}$$

with σ being a positive constant. Once again, we can use Eq. (2.37) to write

$$\langle n'l'm'|e^{-\sigma^2 r^2}|nlm\rangle = c_{n'l}c_{nl}\sum_{p,k} d_{n'lp-k-l}d_{nlk}\int_0^\infty dr r^{2p+2}e^{-(1+\frac{\sigma^2}{\alpha^2})\rho^2}\delta_{l'l}\delta_{m'm}, \tag{2.50}$$

The integral in the above equation has an analytical solution that can be looked up in Ref. [64]. For the particular form here, the solution is given as:

$$\int_0^\infty dr r^{2p+2}e^{-(1+\frac{\sigma^2}{\alpha^2})\rho^2} = \frac{\Gamma(\frac{2p+3}{2})}{2(1+\frac{\sigma^2}{\alpha^2})^{\frac{2p+3}{2}}}. \tag{2.51}$$

In full, the final equation for an element of a Gaussian operator in the SHO basis is given as:

$$\langle n'l'm'|e^{-\sigma^2 r^2}|nlm\rangle = c_{nl}c_{n'l}\sum_{p,k} d_{nlk}d_{n'lp-k-l}\frac{\Gamma(\frac{2p+3}{2})}{2(1+\frac{\sigma^2}{\alpha^2})^{\frac{2p+3}{2}}}\delta_{l'l}\delta_{m'm}. \tag{2.52}$$

2.5.5 The Delta Operator

The delta function is an important operator as it can be used to obtain the expectation value of the wavefunction at the origin. Also, this operator sometimes appears together with the spin-spin term in an interquark potential. The delta function in

spherical coordinates is defined as

$$\delta^{(3)}(\boldsymbol{r}) = \frac{1}{r^2 \sin\theta}\delta(r)\delta(\theta)\delta(\phi), \tag{2.53}$$

which is the only operator in this work that depends on variables θ and ϕ. We can transform the delta function to dimensionless variables, using the property $\delta(\alpha x) = \frac{1}{|\alpha|}\delta(x)$, where α is a scaling parameter. With the dimensionless variable $\boldsymbol{\rho}$ defined in Eq. (2.12) we can express the delta function in Eq. (2.53) as

$$\delta^{(3)}(\boldsymbol{r}) = \frac{\alpha^3}{\rho^2 \sin\theta}\delta(\rho)\delta(\theta)\delta(\phi). \tag{2.54}$$

An element of the delta function operator can be written as

$$\langle n'l'm'|\delta^{(3)}(\boldsymbol{r})|nlm\rangle = \alpha^3 R_{n'l'}(0)Y_{l'm'}(0,0)R_{nl}(0)Y_{lm}(0,0). \tag{2.55}$$

To evaluate this we need to look at the general expression for $R_{nl}(\rho)$ given in 2.14a. We can see that $R_{nl}(0)$ is only non-zero when $l = 0$, in which case we have $R_{n0}(0) = c_{n0}L_n^{1/2}(0)$. The value of the spherical harmonics for $l = 0$ is $Y_{00}(0,0) = 1/(2\sqrt{\pi})$. Putting all this together we have

$$\langle n'l'm'|\delta^{(3)}(\boldsymbol{r})|nlm\rangle = \frac{\alpha^3}{4\pi} c_{n'0}\, c_{n0}\, L_{n'}^{1/2}(0)L_n^{1/2}(0)\delta_{l'0}\delta_{l0}\delta_{m'm}, \tag{2.56}$$

where $L_n^{1/2}(0)$ are the generalised Laguerre polynomials evaluated at the origin.

2.6 Numerical Method

A large portion of this work was devoted to developing a computational framework for numerically solving the Schrödinger equation of three-body potential models. In this section, we will discuss the computational side of the method and some tricks

we have employed to speed up the calculations. For the computation, we have used Mathematica as a programming platform. In this discussion, we will be evaluating the computational side of the method from the point of view of solving the three-body rather than the two-body problem since it is an extension of the two-body problem.

On the technical side, the problem we are solving is the one outlined in Sec. 2.1. The main idea is to construct the Hamiltonian matrix of a system represented in the SHO basis, see Eq. (2.4) for reference. Once a Hamiltonian matrix is constructed we are able to obtain its `Eigenvalues` and `Eigenvectors` using the built-in Mathematica functions. The size of the Hamiltonian matrix is directly dependent on the number of SHO basis functions used for the calculation. The more basis functions the better the approximation but also the more matrix elements we have to compute. The bulk of the computational time is spent building the Hamiltonian matrix, rather than obtaining its eigenvalues or eigenvectors, which only takes a fraction of a second even when the matrix sizes are in the hundreds. On the other hand, computing the entire Hamiltonian matrix can take anywhere from few seconds to few minutes depending on the number of basis functions used. Each element of the Hamiltonian matrix is individually calculated, therefore, the more basis functions, the more elements there are to calculate. The number of elements to calculate goes as N^2 where N is the number of basis functions, however, the first few elements in the upper left part of the matrix take less time to be computed than the last elements towards the lower right part of the matrix due to sums such as one seen in Eq. (2.44), therefore, the time complexity of the algorithm is not simply $O(N^2)$.

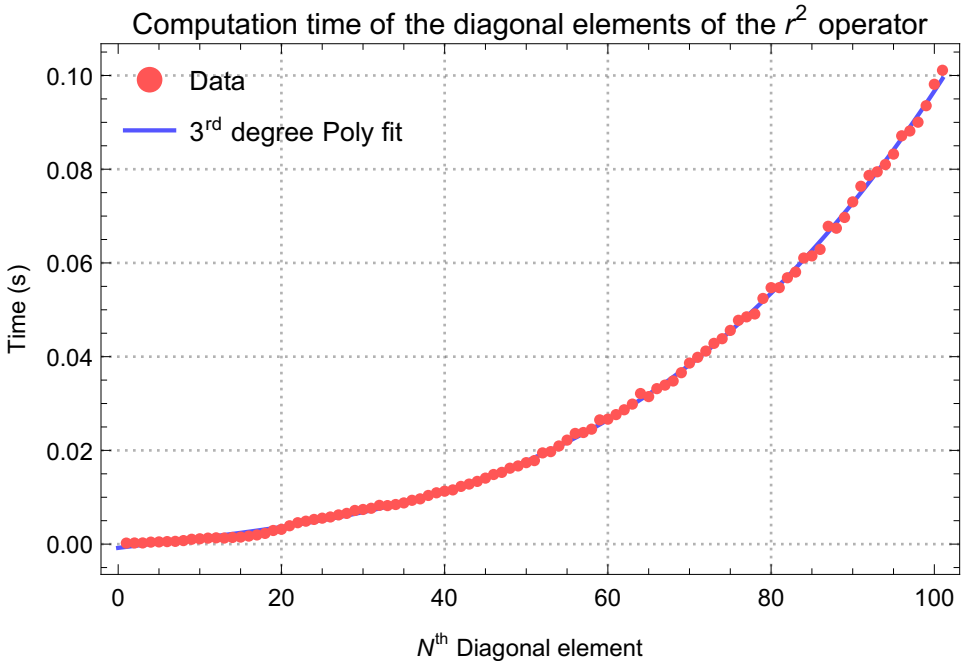

Figure 2.4: Showing the computation time of the diagonal elements of the r^2 operator with $l = 0$ as defined in Eq. (2.44), using our Mathematica code. The fitted line is a third degree polynomial.

In Fig. 2.4 we show the amount of time taken to compute the diagonal only elements of the r^2 operator as defined by Eq. (2.44) where we set $l = 0$. By fitting a third degree polynomial we find the relationship between the time taken to compute the N^{th} diagonal element seems to be cubic in nature. We therefore see that computing elements which are further down and to the right of the matrix take longer to compute than elements closer to the upper left part of the matrix, as mentioned previously. We also note that computations of individual elements for this operator take only fractions of seconds. This data serves as a good proxy for the time complexity for constructing the elements of other operators encountered in this work such as the exponential and Gaussian operators found in Eqs. (2.48) and (2.52), respectively, which share a similar mathematical fidelity with the r^y operator. We note that a third degree polynomial fit is only used when the second degree polynomial fit is not able to fit to the data.

For the rest of this analysis we will be pushing our code to include basis functions up

N_Q	Matrix Size ($n \times n$)
0	2
2	8
4	20
6	40
8	70
10	112
12	168

Table 2.1: Relationship between N_Q and matrix size of operators for the combination $J = \frac{1}{2}, P = +1, \Lambda = 0$ and $S = \frac{1}{2}$.

to $N_Q = 12$, where N_Q is defined as the energy of the coupled SHO basis functions. Mathematically, this is defined as

$$N_Q = 2n + l + 2N + L, \tag{2.57}$$

where the coupled SHO basis functions are denoted by $|nlNL : \Lambda\rangle$. However, we will show the relationship between computation time and matrix size rather than N_Q because matrix size is a better indicator of the number of computations that need to be performed than N_Q. The relation between matrix size and N_Q is dependent on the quantum numbers J, P, Λ and S. For this analysis we will be looking at the "lowest" possible combinations of these quantum numbers, ones we believe are trivial which are $J = 1/2, P = +1, \Lambda = 0$ and $S = 1/2$. For this combination of quantum number the relation between matrix size and N_Q can be found in Tab. 2.1.

Note that in Tab. 2.1 when $N_Q = 0$ the matrix size is 2. This may seem strange as there is only a single combination of the quantum numbers of $2n + l + 2N + L$ that equals 0, this is only possible when $n = l = N = L = 0$. However, the basis functions for spin-dependent models also include the spin degrees of freedom and there are two spin basis functions with total spin $S = \frac{1}{2}$, those are $|S, S_{12}\rangle = |\frac{1}{2}, 0\rangle$ or $|\frac{1}{2}, 1\rangle$. Therefore, even though only a single spatial basis function is allowed when $N_Q = 0$, there are two possible spin basis functions when $S = \frac{1}{2}$, yielding two separate total spin-space basis functions, one being $|0000 : 0\rangle|\frac{1}{2}, 0\rangle$ and the other being $|0000 : 0\rangle|\frac{1}{2}, 1\rangle$. Note, the same is true for $N_Q > 0$. This will be discussed in more

detail in Ch. 6.

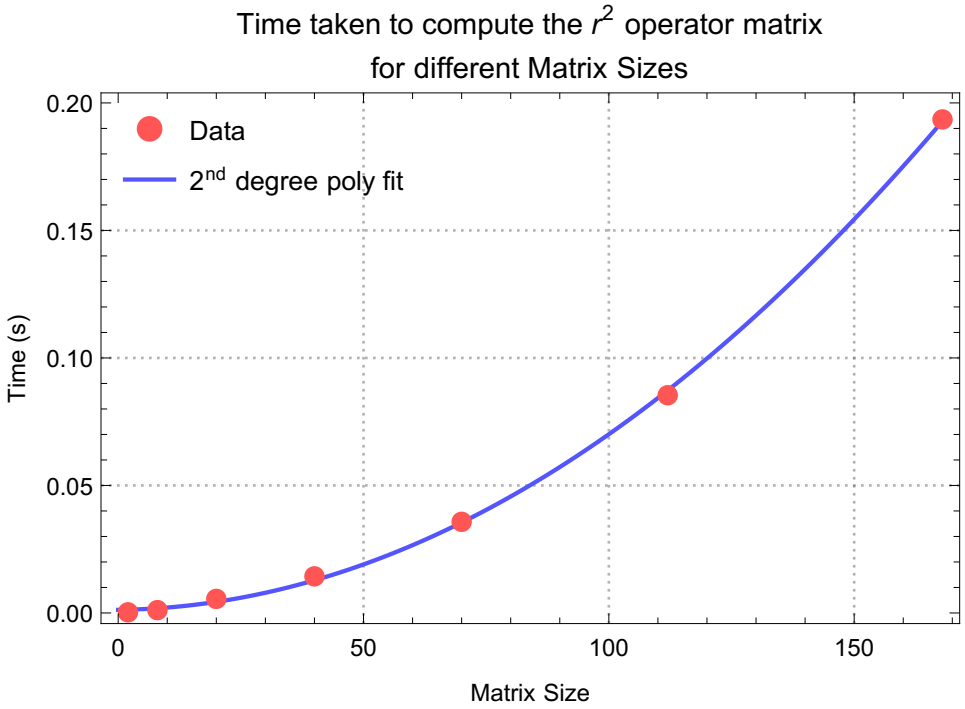

Figure 2.5: Showing the time taken to compute matrix representation of the r^2 operator in the SHO basis, defined in Eq. (2.44) with $l = 0$, using our Mathematica code. The fitted line is a second degree polynomial.

In the next series of figures; 2.5, 2.6 and 2.7, we show the time taken to compute the matrix representations of the r^2, exponential and Gaussian type operators in the SHO basis using our code. We find that the time complexity to compute the matrix representations of these operators is either quadratic or cubic with respect to the number of SHO basis functions used. We find that the exponential operator takes the most amount of time to be computed, over 10 seconds in the case of $N_Q = 12$ or Matrix Size $= 168$, equivalently. This is most likely due to the parabolic cylinder functions that need to be computed for this operator, see Eq. (2.48). The exponential operator will appear in most of the potential models which we will encounter in this work with the exception being the zero-temperature baryon model.

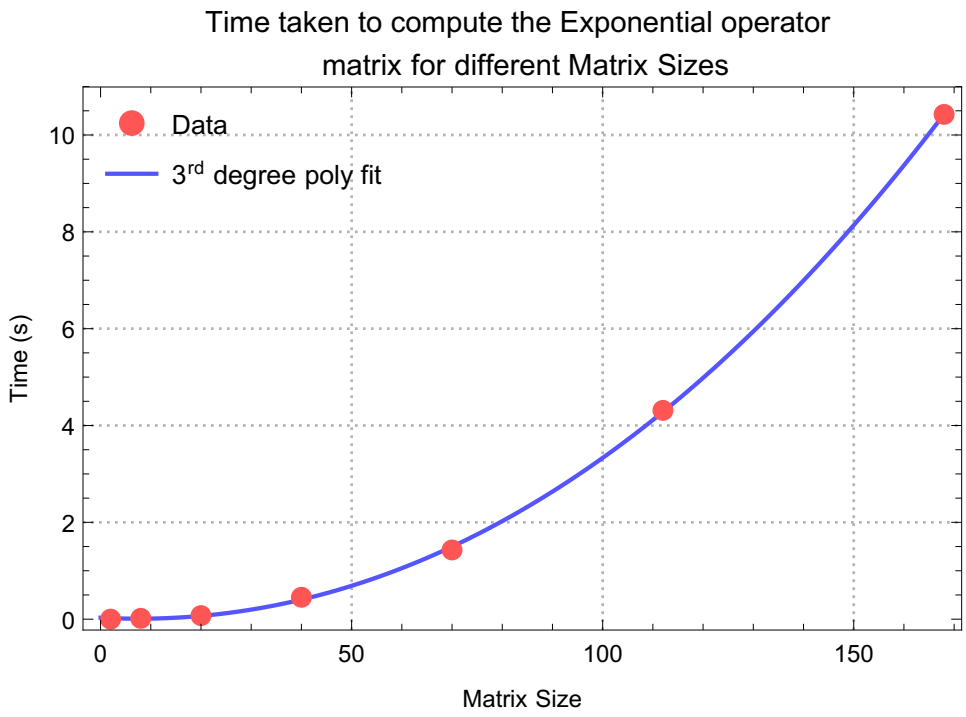

Figure 2.6: Showing the time taken to compute matrix representation of the exponential operator in the SHO basis, defined in Eq. (2.48), using our Mathematica code. The fitted line is a third degree polynomial.

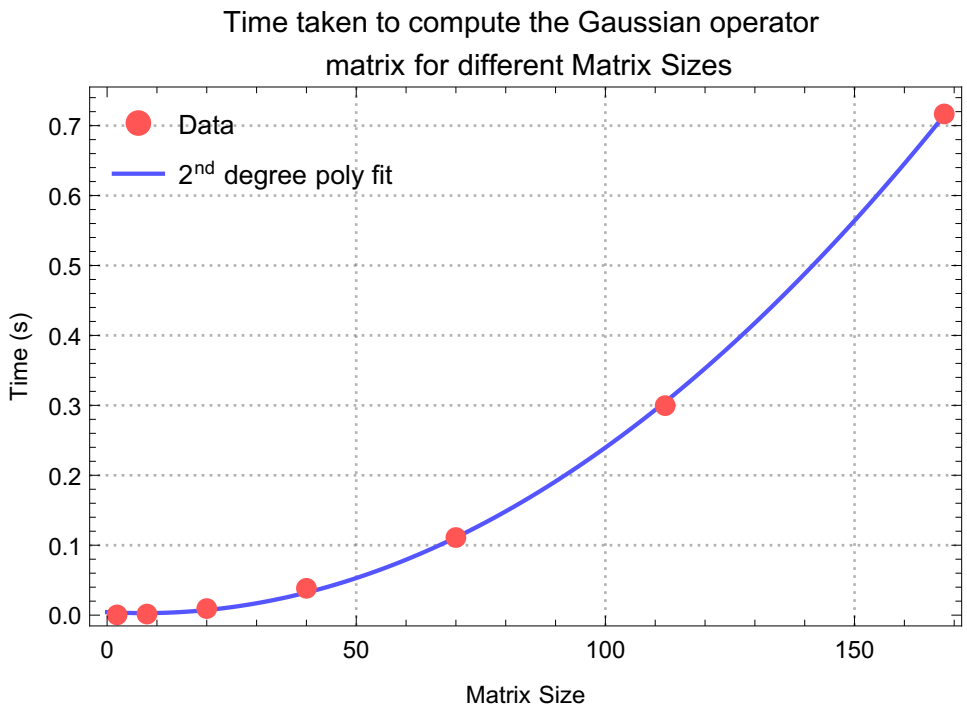

Figure 2.7: Showing the time taken to compute matrix representation of the Gaussian operator in the SHO basis, defined in Eq. (2.52), using our Mathematica code. The fitted line is a second degree polynomial.

To solve the three-body problem we also must compute the Talmi-Moshinsky coefficients [65], responsible for transforming coupled SHO basis functions from one Jacobi frame to another. In what follows, we will briefly discuss the amount of time taken to compute these coefficients as they are detrimental to solving the three-body problem and are a costly part of the calculation in terms of computation time. We will also discuss some tricks performed to avoid constantly recalculating these coefficients, significantly reducing computation time. In our work, we will be constructing matrices containing the Talmi-Moshinsky coefficients and using those to transform operators by sandwiching them between what we will call the generalised transformation matrices. The details of computing the generalised transformation matrices will be discussed in Sec. 6.2. In this part of the discussion, we are mostly interested in the time taken to compute the generalised transformation matrices, defined in Eq. (6.9). In Fig. 2.8 we illustrate the time taken to compute the generalised transformation matrices which involve the Talmi-Moshinsky coefficients. The matrices that

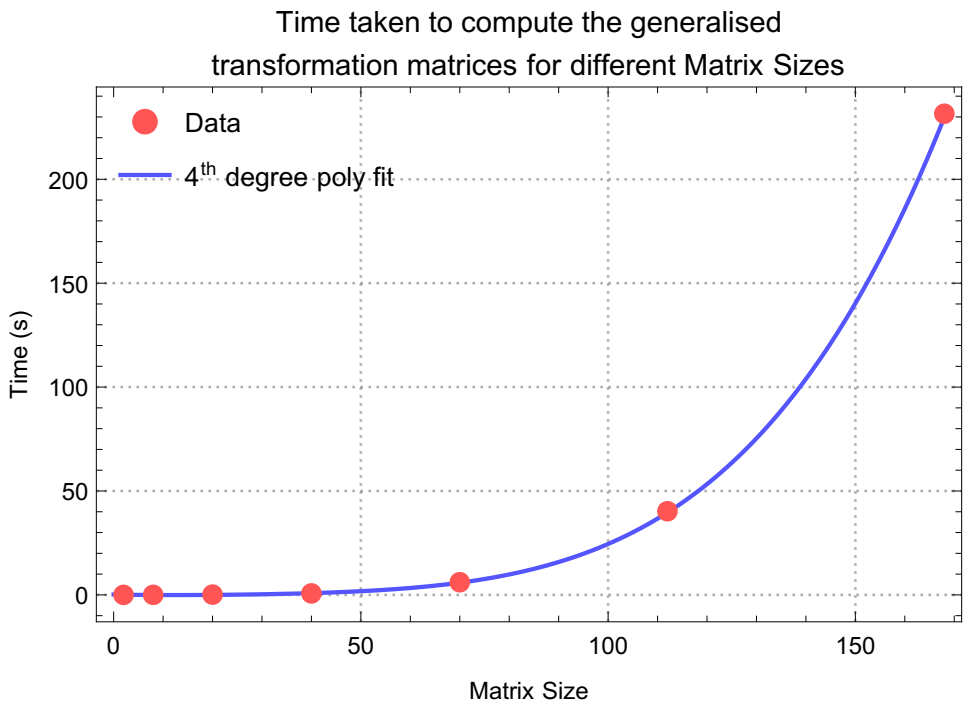

Figure 2.8: Showing the time taken to compute the generalised transformation matrices defined by Eq. (6.9), using our Mathematica code. The best fit is obtained by a fourth degree polynomial.

we have computed are responsible for transforming operators from the 12 to the 23 Jacobi frame, see Fig. 2.2 for reference. We find that the time taken to compute the generalised transformation matrix for $N_Q = 12$ takes over 200 seconds. We also find that to fit the computation time we need to use a polynomial fit to the 4^{th} degree to obtain a good fit, showing that the computation time grows very quickly as matrix size increases. We find that computing the generalised transformation matrices takes a significant amount of computation time.

We would like to preface the following discussion by saying that the Talmi-Moshinsky coefficients in our work are independent of the size (or variational) parameters that determine the size of the basis functions. The only dimensionful quantities that the Talmi-Moshinsky coefficients are dependent on are the quark masses. To alleviate some of the time spent on calculating the Talmi-Moshinsky coefficients we have separated the calculation into two parts, a part that does not depend on quark masses, such as obtaining summation variables which is a costly computation, and another

part which performs the summation and involves the quark masses. This allows us to pre-compute and store the results of the part of the computation that is independent of model parameters, such that when we want to compute specific coefficients, we can call back on the stored results and only compute the part which is dependent on model parameters. This trick allows us to save a significant amount of time during calculations. In computer language the process of pre-computing and storing results to save time in future calculations is called memoisation. We have also implemented memoisation for other parts of our calculation where possible, i.e. for parts of calculations that do not depend on any model parameters, in that way the amount of storage required for the "memoised" quantities is kept to a minimum, only taking up a few megabytes but saving a considerable amount of computational time. Whenever a new model is presented or any model parameters are changed, we only need to recalculate a small portion of the calculation rather than recalculating everything from scratch.

To see this process at work we will perform the same calculation of the generalised transformation matrices in two runs, the first run will generate the matrices using the quark masses $m_1 = m_2 = m_3 = 1$ GeV as if it was doing this calculation for the first time. During that run, parts of the calculation which are independent of model parameters will be automatically saved and on the second run we will change the quark masses to $m_1 = 1$ GeV, $m_2 = 2$ GeV and $m_3 = 3$ GeV and we will show that the second run will take significantly less time. The results are presented in Tab. 2.2. We see that on the second run, the same calculations take much less time, for instance the calculation which computes the elements of the 168×168 generalised transformation matrix in the first run takes 203 seconds where as in the second run for different quark masses only 0.5 seconds. Whenever the algorithm computes something it has not seen before, it will compute it and save the parts which do not need to be recalculated saving significant amount of time on all the runs after that.

Matrix Size	Run 1 (s)	Run 2 (s)
2	0.01	0.0008
8	0.02	0.004
20	0.08	0.02
40	0.56	0.04
70	4.97	0.09
112	33.30	0.23
168	203.59	0.50

Table 2.2: Time taken in seconds to calculate the generalised transformation matrices in the first run and second run of the calculation. During the first run, certain parts of the calculation are memorised such that they do not need to be recalculated again in the second run. We show this for different matrix sizes. In the first run we choose $\{m_1, m_2, m_3\} = \{1, 1, 1\}$ GeV and in the second run $\{m_1, m_2, m_3\} = \{1, 2, 3\}$ GeV

.

By this point in the discussion of the numerical method we have illustrated the computation time of various operators and the generalised transformation matrices. These form the key components for obtaining the Hamiltonian matrix. Therefore next, we will illustrate the time taken to compute the Hamiltonian matrix as a function of matrix size. We will be obtaining the Hamiltonian matrix while utilising the memoisation trick discussed earlier. This will show us the true performance of the code as it is used in practice. The model that we will be using in this discussion is a zero-temperature baryon model discussed in Sec. 7.1. We will be obtaining a Hamiltonian matrix for the Λ_c baryon system defined by the model parameters specified in Eq. 7.5 and by the quantum numbers $J = \frac{1}{2}, P = +1, \Lambda = 0$ and $S = \frac{1}{2}$ and we must specify the symmetry of the flavour wavefunction which is symmetric in the case of the Λ_c baryon, this in turn limits the number of basis functions used for the calculation, this is discussed in more detail in Ch. 6. For this calculation we have chosen an arbitrary value for the size of the basis functions, which is set by $\omega = 1$GeV.

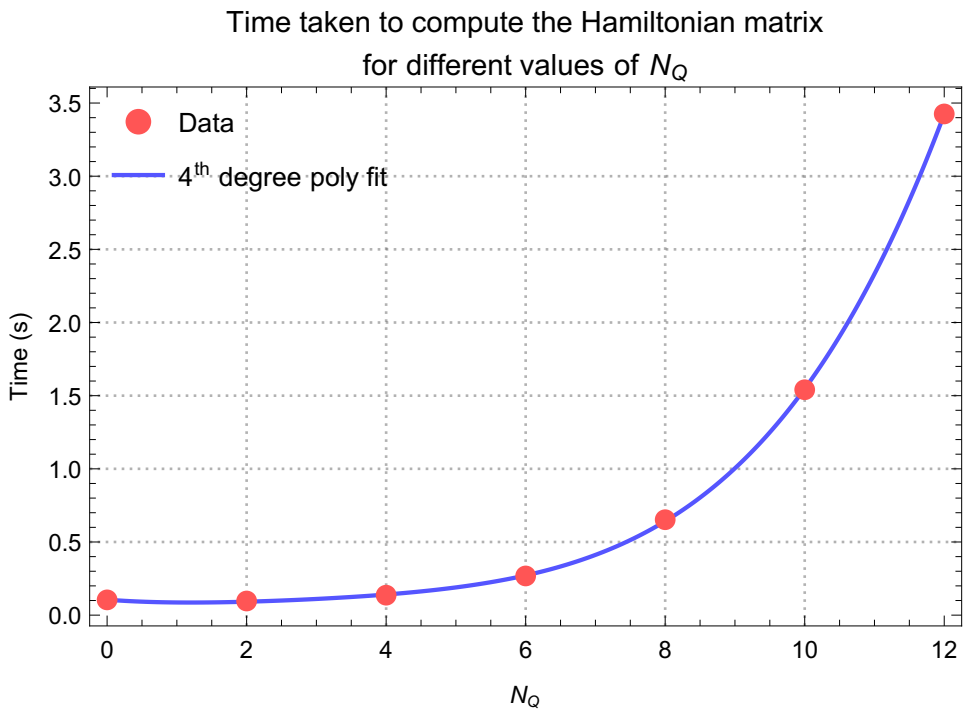

Figure 2.9: Showing the time taken to compute the Hamiltonian matrix defined by Eq. (7.2), using our Mathematica code. The best fit is obtained by a fourth degree polynomial.

In Fig. 2.9 we see that it takes just under 8 seconds to compute the entire three-body Hamiltonian matrix for $N_Q = 14$. This involved computing all the necessary operators, the Talmi-Moshinsky coefficients and performing the required manipulations to obtain the Hamiltonian matrix.

The remaining part of the calculation is to optimise the size of the basis functions, i.e. vary the ω parameter until we find a minimum of the energy of the excited state that we are interested in. For this discussion, we will focus on the ground state of the Λ_c baryon and therefore optimise the value of ω for that excited state. This involves setting a value of ω, computing the Hamiltonian, finding the lowest eigenvalue of the Hamiltonian matrix and rerunning the calculation with a different value of ω and repeating this process until we minimise the energy of the ground state. To help us do this we are using the golden section search algorithm which is designed to search for a minimum of a function. This algorithm works by choosing a lower and an upper

limit (a section) of the function, where a minimum is believed to exist and gradually narrowing down the limits and honing on the minimum, the search is ended once a chosen tolerance level is reached, given the two final limits, we choose the midpoint between them to give us a value of ω that we are satisfied with. This algorithm was chosen as it does not rely on computing gradients of a function which can be costly for this particular problem. Searching for the minimum takes up the most time of the calculation since the Hamiltonian needs to be recalculated multiple times with a different value of ω each time. Luckily thanks to memoisation, this process takes much less time than if we had to compute the Hamiltonian from scratch each time. Usually, we are able to obtain a good value of ω in under a minute, which of course depends on the value of N_Q. As we can see in Fig. 2.9 the time taken to compute the Hamiltonian matrix for $N_Q = 12$ is just under 4 seconds, this calculation will need to be performed multiple times with different values of ω until convergence is reached. In Fig. 2.10 we illustrate the time taken to optimise the ω parameter, for different values of N_Q using the golden section search algorithm. We find that it takes just under 40 seconds to find an optimum value of ω when $N_Q = 12$.

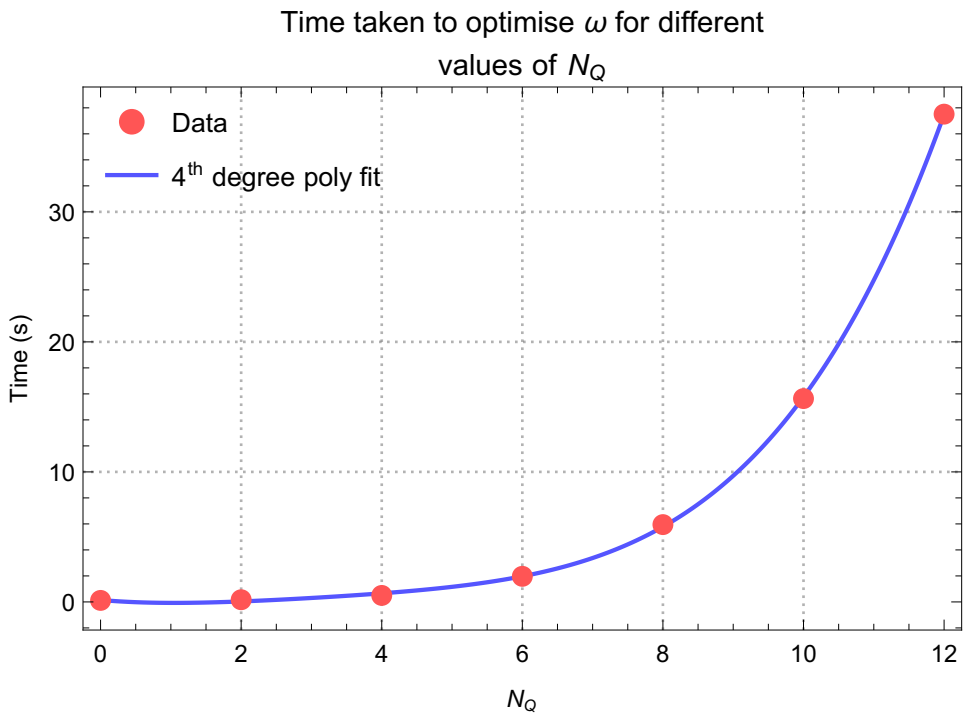

Figure 2.10: Showing the time taken to optimise ω for different values of N_Q, using the golden section search algorithm. The best fit is obtained by a fourth degree polynomial.

3

Two-Body Potential Model

In this chapter, will solve a two-body, spin-dependent meson model using the variational method. We will use perturbation theory to include the hyperfine contributions, splitting the spin-averaged states. The meson model that we will be solving has been proposed by Li et al. (2009) [16]. We will compare our results with the ones given in the paper in order to ensure that our numerical approach for solving potential models using the variational method works as intended before we move on to solving three-body systems.

In the following sections, we will outline the potential model and describe how perturbation theory can used to include the hyperfine corrections to the meson masses. Finally, we will compare the results of different meson states energies obtained by us to those obtained by Li.

3.1 Meson Potential

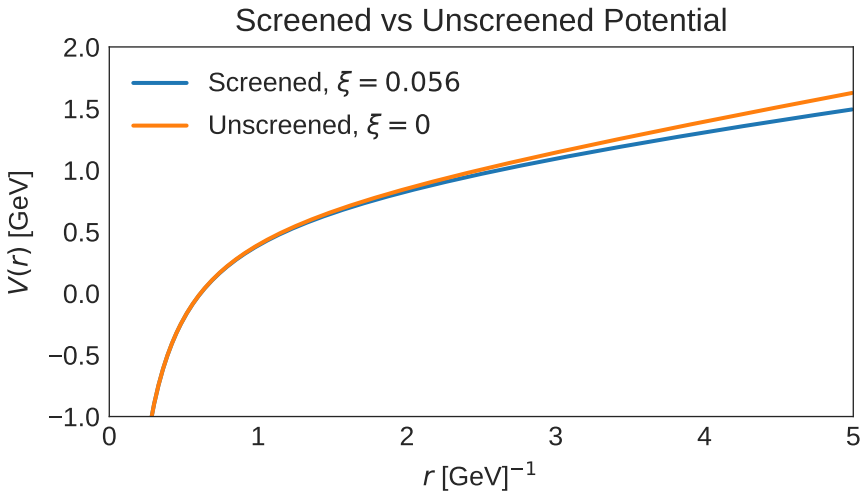

Figure 3.1: Plot of the spinless part of the potential (Eq. 3.1)). We compare the screened potential used in this chapter with a standard unscreened Cornell potential.

The potential used in [16] is a screened potential which differs slightly from the commonly used Cornell potential. In Fig. 3.1 we compare the screened potential used in this work with the standard Cornell potential. We see that the two are very similar and only begin to differ at large r. Therefore, the screening affects mostly larger states i.e. highly excited or very light meson states whose size is larger than that of heavy mesons or mesons in their ground states. Li et al. propose the screened potential to correct for the tendency of common potentials (such as the Cornell potential) to overestimate the energy values of highly excited states. They show that the screened potential gives better predictions for the highly excited states.

We will use the work produced by Li et al. to test our numerical method for solving models which include hyperfine interactions. We will ensure that we are able to solve hadron models which include spin as we are ultimately interested in solving baryon models with spin interactions. Solving two-body spin dependent models is simpler

α_C	ξ	C	m_b	σ	Λ
0.37	0.056GeV	0.677GeV	4.4GeV	3.3GeV	0.21GeV^2

Table 3.1: Table of parameters used in the Hamiltonian, obtained from Ref. [16].

than three-body spin-dependent models, hence, this is where we start. The full meson potential is defined in Ref. [16] as,

$$\begin{aligned} V_{\text{scr}}(r) &= V_V(r) + V_S(r), \\ V_V(r) &= -\frac{4}{3}\frac{\alpha_C}{r}, \\ V_S(r) &= \Lambda\left(\frac{1-e^{-\xi r}}{\xi}\right) + C, \end{aligned} \tag{3.1}$$

where $V_V(r)$ is the long-range vector like potential arising from one-gluon exchange and $V_S(r)$ is the scalar like potential responsible for short range interactions. The hyperfine interactions which will be treated perturbatively in this chapter are given as,

$$H_{SS} = \frac{32\pi\alpha_C}{9m_1m_2}\tilde{\delta}_\sigma(r)\boldsymbol{S}_1\cdot\boldsymbol{S}_2, \tag{3.2}$$

where $\boldsymbol{S}_1$ and $\boldsymbol{S}_2$ are the spins of quarks 1 and 2, respectively. Normally, the $\tilde{\delta}_\sigma(r)$ is taken to be the regular Dirac-delta function, however, Li et al. use a smeared delta function i.e. a Gaussian function defined as $\tilde{\delta}_\sigma(r) = (\sigma/\sqrt{\pi})^3 e^{-\sigma^2 r^2}$. The spin-orbit term is given as

$$H_{LS} = \frac{1}{2m_1m_2r}\left(3V_V'(r) - V_S'(r)\right)\boldsymbol{L}\cdot\boldsymbol{S}, \tag{3.3}$$

where $\boldsymbol{L}$ is the total orbital angular momentum of the meson state and $\boldsymbol{S}$ is the total spin of the meson. Finally, the tensor term is given as

$$H_T = \frac{1}{12m_1m_2}\left(\frac{1}{r}V_V'(r) - V_V''(r)\right)T. \tag{3.4}$$

The full Hamiltonian is then given as

$$H_{\text{tot}} = \sum_{i=1}^{2} m_i + V_{\text{scr}}(r) + H_{SS} + H_{LS} + H_T. \tag{3.5}$$

The parameters for this model are given in Tab. 3.1. We will give the expectation values of the spin-dependent terms. First, for the spin-spin term we have

$$\langle n'l'm'|\boldsymbol{S}_1 \cdot \boldsymbol{S}_2|nlm\rangle = \left(\frac{1}{2}S^2 - \frac{3}{4}\right)\delta_{n'n}\delta_{l'l}\delta_{m'm}. \tag{3.6}$$

For the spin-orbit term, we have

$$\langle n'l'm'|\boldsymbol{L} \cdot \boldsymbol{S}|nlm\rangle = \frac{1}{2}\left(J(J+1) - L(L+1) - S(S+1)\right)\delta_{n'n}\delta_{l'l}\delta_{m'm}, \tag{3.7}$$

where J is the total angular momentum of the meson defined as $\boldsymbol{J} = \boldsymbol{L}+\boldsymbol{S}$. Lastly, the tensor operator T has non-vanishing diagonal matrix elements for $L > 0$, spin-triplet states only, which are

$$\langle {}^3L_J|T|{}^3L_J\rangle = \begin{cases} -\frac{L}{6(2L+3)}, & J = L+1, \\ \frac{1}{6}, & J = L, \\ -\frac{(L+1)}{6(2L-1)}, & J = L-1. \end{cases} \tag{3.8}$$

3.2 Perturbative Treatment of Spin-Term Corrections

For the perturbative treatment, the Hamiltonian will be split into two parts

$$H = H_0 + H_I, \tag{3.9}$$

where H_0 is the unperturbed part of the Hamiltonian which can be expressed as

$$H_0 = \sum_{i=1}^{2} m_i + \omega(2n + l + \tfrac{3}{2}) - \tfrac{1}{2}\mu\omega^2 r^2 + V_{\text{scr}}(r), \tag{3.10}$$

where we have used the previously obtained general form for a two-body Hamiltonian, which can be found in Eq. (2.31). The potential term $V_{\text{scr}}(r)$ is defined in Eq. (3.1). The spin-averaged energies of the mesons are obtained by solving

$$H_0|\psi_0^{(n)}\rangle = E_0^{(n)}|\psi_0^{(n)}\rangle, \tag{3.11}$$

where n is a generic label describing the spin-averaged meson state. The hyperfine correction terms split the spin-averaged energies based on the four different combinations of S and J quantum states that a meson can be found in. The four combinations are presented in Tab. 3.2.

S	0	1	1	1
J	L	$L-1$	L	$L+1$

Table 3.2: Four different combinations of S and J quantum states that a meson can be found in.

Therefore, we have four different perturbative terms $H_I^{^{2s+1}L_J}$ each corresponding to a particular combination of $^{2s+1}L_J$ quantum numbers, they are defined as

$$H_I^{^{2s+1}L_J} = H_{SS}^{^{2s+1}L_J} + H_{LS}^{^{2s+1}L_J} + H_T^{^{2s+1}L_J}. \tag{3.12}$$

The energies of the four various states can be obtained as follows

$$E_{^{2s+1}L_J}^{(n)} = E_0^{(n)} + \langle\psi_0^{(n)}|H_I^{^{2s+l}L_J}|\psi_0^{(n)}\rangle, \tag{3.13}$$

which is the energy of the spin-averaged state plus one of the four possible perturbations. The equations in (3.13) are four separate equations which can be expressed in

matrix form as

$$\begin{pmatrix} E_{^1L_L} \\ E_{^3L_{L-1}} \\ E_{^3L_L} \\ E_{^3L_{L+1}} \end{pmatrix} = \begin{pmatrix} 1 & -3/4 & 0 & 0 \\ 1 & 1/4 & -(L+1) & \frac{L+1}{2L-1} \\ 1 & 1/4 & -1 & -1 \\ 1 & 1/4 & L & \frac{L}{2L+3} \end{pmatrix} \begin{pmatrix} E_0 \\ \Delta_{SS} \\ \Delta_{SO} \\ \Delta_T \end{pmatrix}, \tag{3.14}$$

where we have used Eqs. (3.6), (3.7) and (3.8), to obtain the 4×4 matrix containing the spin part of the hyperfine corrections. The vector on the right hand side contains the radial parts of the hyperfine corrections to the potential. For example $\Delta_{SS} = \frac{32\pi\alpha_C}{9m_1m_2}\langle\psi_0^{(n)}|\tilde{\delta}_\sigma(r)|\psi_0^{(n)}\rangle$.

To obtain matrix representation of the H_0 and H_I operators in the SHO basis we can use solutions obtained in Sec. 2.5. For instance, H_0 contains an operator m_i which is a constant, the matrix representation of m_i can be obtained using Eq. (2.38). Another operator found in H_0 is the r^2 operator found in the $-\frac{1}{2}\mu\omega^2 r^2$ term, to obtain the matrix representation of that operator in the SHO basis, we can use Eq. 2.44. Similarly, for the Gaussian operator found in H_{SS} term, we can use Eq. 2.52. Therefore, we have all the tools for constructing H_0 and H_I in the SHO basis, and we can use the matrix representations to diagonalise H_0 and obtain its eigenvalues and eigenvectors necessary for perturbative treatment. In the next section, we will present the results obtained using our numerical method for solving the meson model presented in this chapter.

3.3 Variational Parameter ω

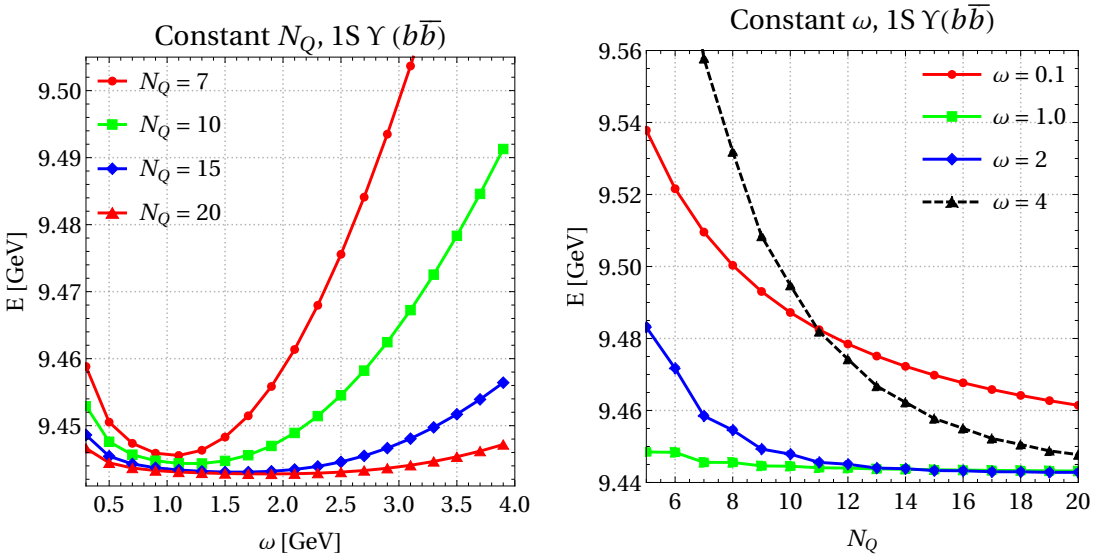

Figure 3.2: Energy of the spin-averaged $\Upsilon(b\bar{b})$ 1S ground state as function of the variational parameter ω on the left and number of basis functions N_Q on the right.

In this section, we will discuss the role of the variational parameter ω when obtaining various system observables. This is the first time in this work that we get to see the role of the variational parameter ω used in a specific example. The variational method depends on optimising the variational parameter ω such that the energy of a state is minimised, as discussed in Sec. 2.1. We used the Mathematica program to diagonalise the Hamiltonian, as described in the numerical method in Sec. 2.6, to obtain plots such as the ones seen in Fig. 3.2.

In Fig. 3.2 we plot the energy of the spin-averaged $b\bar{b}$ meson ground (1S) state as a function of the variational parameter ω on the left and as a function of the number of SHO basis functions used for the numerical approximation on the right. The first thing we see in the plot on the left is the presence of a minimum energy. The optimal ω value lies where the energy is minimum. Secondly, we see that as we include more SHO basis functions in our calculations, the minimum energy decreases but eventually

we reach a plateau where adding more basis functions results in very small changes to the minimum energy. This is most pronounced in the plot on the right. And lastly, we note that as we increase the number of basis functions N_Q used, the approximation becomes less dependant on ω. We see this through the flattening of the curves in the plot on the left. For example, for $N_Q = 20$ in the plot on the left, we see that the energy of the state varies very little in the range of $1\text{GeV} \leq \omega \leq 3\text{GeV}$. Comparing that with the curve generated using $N_Q = 7$ we see that the energy is more dependent on the variational parameter ω. This behaviour is expected since in the limit where an infinite set of basis functions is used ($N_Q \to \infty$), we expect no dependence on ω.

Lastly, the plot on the right in Fig. 3.2, demonstrates the stability condition for our calculations. We can see that for $\omega = 1\text{GeV}$ or 2GeV the energy of the state has stabilised, i.e. if we keep increasing N_Q, we will see very little improvement in the results (very little decrease in energy). However, in the case where $\omega = 0.1$ or 4, we can see that stability has not yet been reached, even when $N_Q = 20$.

From those two plots we can see that we do not only have to ensure to choose the optimum ω but we also need to ensure that our calculations reach stability, i.e. we must use enough basis functions such that increasing the number of basis functions decreases the minimum energy by very little. In the plot on the right in Fig. 3.2 we can see that 20 basis functions is enough to achieve stable results, given we choose an appropriate value of ω, in this case $1\text{GeV} \leq \omega \leq 2\text{GeV}$ would suffice.

All our results will be obtained by finding the minima of E vs. ω plots for sufficient number of basis functions. We will be using the golden section search algorithm for finding the minima of such curves. The golden section search algorithm has been discussed in more detail in Sec. 2.6

3.4 Comparing Results

In this section, we present the results obtained by our numerical method and compare them with the results obtained by Li et al. in Ref. [16]. We compute the energies of various excited bottomonium states and present them in tables below. The orbital excitations (S, P and D - wave states) have been split into three separate Tables 3.3, 3.4 and 3.5, respectively, within which we show the radial excitations of those states.

Using the variational method and solving the model perturbatively we find that we are able to reproduce the results found in the paper with largest discrepancy between energies being only 4 MeVs. In Tabs. 3.3, 3.4 and 3.5 we also record the value of the optimised variational parameter ω used for each state. The value of ω was determined using the optimisation procedure described in Secs. 2.1 and 2.6, i.e. by identifying the minimum of energy vs. ω plots.

We note that that the value of ω decreases for higher excited states. The value of ω is closely tied with the size of the basis functions used for the approximations. The smaller the ω the larger the size of the basis functions. This indicates that the states increase in size, as they become more excited. Later, for different hadron models we will investigate the size of a hadron through observables such as the root mean square radius between quarks for different excited states and find that higher excited states indeed increase in size.

This concludes the chapter, we have used the variational method and perturbation theory to solve a meson model with hyperfine interaction terms. We were able to successfully reproduce results found in the literature. We can conclude that our method for solving two-body hadron models with hyperfine interactions has been well developed. We are ready to move on to solving three-body models, including baryons, using similar techniques.

State		ω	Theor. of ours	Theor. of Ref. [16]
1S	$\eta_b(1\,^1S_0)$	1.9	9.389	9.389
	$\Upsilon(1\,^3S_1)$		9.461	9.460
2S	$\eta_b'(2\,^1S_0)$	0.9	9.988	9.987
	$\Upsilon(2\,^3S_1)$		10.016	10.016
3S	$\eta_b(3\,^1S_0)$	0.5	10.332	10.330
	$\Upsilon(3\,^3S_1)$		10.351	10.351
4S	$\eta_b(4\,^1S_0)$	0.4	10.597	10.595
	$\Upsilon(4\,^3S_1)$		10.612	10.611
5S	$\eta_b(5\,^1S_0)$	0.3	10.820	10.817
	$\Upsilon(5\,^3S_1)$		10.832	10.831
6S	$\eta_b(6\,^1S_0)$	0.23	11.014	11.011
	$\Upsilon(6\,^3S_1)$		11.024	11.023
7S	$\eta_b(7\,^1S_0)$	0.18	11.187	11.183
	$\Upsilon(7\,^3S_1)$		11.195	11.193

Table 3.3: Comparison of obtained masses for the $b\bar{b}$ S states using our model vs that of Ref. [16]

State		ω	Theor. of ours	Theor. Ref. [16]
1P	$h_b(1\,^1P_1)$	0.7	9.903	9.903
	$\chi_{b0}(1\,^3P_0)$		9.859	9.865
	$\chi_{b1}(1\,^3P_1)$		9.900	9.897
	$\chi_{b2}(1\,^3P_2)$		9.917	9.918
2P	$h_c(2\,^1P_1)$	0.5	10.256	10.256
	$\chi_{b0}(2\,^3P_0)$		10.221	10.226
	$\chi_{b1}(2\,^3P_1)$		10.254	10.251
	$\chi_{b2}(2\,^3P_2)$		10.268	10.269
3P	$h_b(3\,^1P_1)$	0.3	10.529	10.529
	$\chi_{b0}(3\,^3P_0)$		10.498	10.502
	$\chi_{b1}(3\,^3P_1)$		10.527	10.524
	$\chi_{b2}(3\,^3P_2)$		10.539	10.540
4P	$h_b(4\,^1P_1)$	0.257	10.757	10.757
	$\chi_{b0}(4\,^3P_0)$		10.729	10.732
	$\chi_{b1}(4\,^3P_1)$		10.755	10.753
	$\chi_{b2}(4\,^3P_2)$		10.766	10.767
5P	$h_b(5\,^1P_1)$	0.2	10.955	10.955
	$\chi_{b0}(5\,^3P_1)$		10.931	10.933
	$\chi_{b1}(5\,^3P_1)$		10.954	10.951
	$\chi_{b2}(5\,^3P_2)$		10.964	10.965

Table 3.4: Comparison of obtained masses for the $b\bar{b}$ P states using our model vs that of Ref. [16]

State		ω	Theor. of ours	Theor. of Ref. [16]
1D	$\eta_{c2}(1\,^1D_2)$	0.4	10.152	10.152
	$\psi(1\,^3D_1)$		10.144	10.145
	$\psi_2(1\,^3D_2)$		10.152	10.151
	$\psi_3(1\,^3D_3)$		10.155	10.156
2D	$\eta_{c2}(2\,^1D_2)$	0.3	10.439	10.439
	$\psi(2\,^3D_1)$		10.431	10.432
	$\psi_2(2\,^3D_2)$		10.439	10.438
	$\psi_3(2\,^3D_3)$		10.442	10.442
3D	$\eta_{c2}(3\,^1D_2)$	0.25	10.677	10.677
	$\psi(3\,^3D_1)$		10.670	10.670
	$\psi_2(3\,^3D_2)$		10.677	10.676
	$\psi_3(3\,^3D_3)$		10.680	10.680
4D	$\eta_{c2}(4\,^1D_2)$	0.2	10.883	10.883
	$\psi(4\,^3D_1)$		10.876	10.877
	$\psi_2(4\,^3D_2)$		10.883	10.882
	$\psi_3(4\,^3D_3)$		10.886	10.886
5D	$\eta_{c2}(5\,^1D_2)$	0.16	11.066	11.066
	$\psi(5\,^3D_1)$		11.059	11.060
	$\psi_2(5\,^3D_2)$		11.066	11.065
	$\psi_3(5\,^3D_3)$		11.069	11.069

Table 3.5: Comparison of obtained masses for the $b\bar{b}$ D states using our model vs that of Ref. [16]

4

Talmi-Moshinsky Transformations

To address the three-body problem in quantum mechanics using the variational method, we adopt the Jacobi coordinates as a natural coordinate basis to characterise the system. In Section 2.2, a brief summary is provided. Our primary choice is the 12 basis[1], as depicted in Figure 2.2. However, this choice introduces complexity in expressing potentials that depend on the distances between particle pairs 23 and 31. To overcome this challenge, we employ all three Jacobi coordinate bases, each representing the distance between one of the three particle pairs. This approach involves separating the three-body pair-wise potential into three distinct terms, effectively treating them as three individual two-body potentials. Subsequently, we solve each component of the potential within its respective Jacobi frame.

The next step involves expressing each of the two-body components of the three-body potential in their respective Simple Harmonic Oscillator (SHO) basis. As the 12 basis is the main choice, it is necessary to perform transformations that allow us to convert the coupled SHO basis wavefunctions from the 12 basis to the 23 and 31 bases. This is where the Talmi-Moshinsky transformations come into play. In this chapter, we will provide a comprehensive explanation of how these transformations can be effectively utilised to solve three-body potential models in the realm of quantum mechanics.

[1]This should be read as the 'one-two' basis rather than the 'twelve' basis, similarly for the 23 and 31 basis, these are the 'two-three' and 'three-one' basis.

During the course of this study, specifically in 2020, Silvestre et al. published a paper in which they applied the Talmi-Moshinsky transformations to solve a spin-independent baryon potential model [1]. It is important to acknowledge their contribution, as their utilisation of the Talmi-Moshinsky transformations enabled the resolution of the three-body problem. While our approach and implementation differ slightly from that presented in Ref. [1], the fundamental ideas remain the same. Towards the end of this chapter, we will delve into a discussion on the similarities and differences between our methods.

In our approach, we will employ the method proposed by Buck et al. (1996) [66] to obtain the expansion coefficients required for transforming coupled Simple Harmonic Oscillator (SHO) wavefunctions between different coordinate bases. This method is particularly effective when the coordinate bases are connected through orthogonal transformations, such as rotations.

However, since the Jacobi frames depicted in Figure 2.2 are generally not related by orthogonal transformations due to the potential variation in particle masses, we will introduce modified sets of Jacobi coordinate bases that satisfy this condition. Essentially, we will transition to utilising dimensionless Jacobi coordinates.

Once we have elaborated on the dimensionless Jacobi basis, we will explain the technique for transforming the coupled SHO basis functions between these bases. Lastly, we will elucidate the procedure for representing the complete three-body potential within the 12 SHO basis.

Throughout the subsequent discussion, we will occasionally refer to the 12 basis as frame 3, the 23 basis as frame 1, and the 31 basis as frame 2. This nomenclature is derived from how we label the Jacobi variables, where $\boldsymbol{r}_3 \equiv \boldsymbol{x}_1 - \boldsymbol{x}_2$ represents the distance between particles 1 and 2 in the 12 basis, and the same logic applies to the 23 and 31 bases.

4.1 Three Jacobi Frames

The dimensionful Jacobi frames illustrated in Fig. 2.2 can be mathematically defined as

$$\begin{aligned} \boldsymbol{r}_3 &= \boldsymbol{x}_1 - \boldsymbol{x}_2, \quad \boldsymbol{R}_3 = \frac{m_1\boldsymbol{x}_1 + m_2\boldsymbol{x}_2}{m_1+m_2} - \boldsymbol{x}_3, \\ \boldsymbol{r}_1 &= \boldsymbol{x}_2 - \boldsymbol{x}_3, \quad \boldsymbol{R}_1 = \frac{m_2\boldsymbol{x}_2 + m_3\boldsymbol{x}_3}{m_2+m_3} - \boldsymbol{x}_1, \\ \boldsymbol{r}_2 &= \boldsymbol{x}_3 - \boldsymbol{x}_1, \quad \boldsymbol{R}_2 = \frac{m_1\boldsymbol{x}_1 + m_3\boldsymbol{x}_3}{m_1+m_3} - \boldsymbol{x}_2, \end{aligned} \tag{4.1}$$

the c.o.m. coordinate is given as $\boldsymbol{\mathcal{R}} = (m_1\boldsymbol{x}_1 + m_2\boldsymbol{x}_2 + m_3\boldsymbol{x}_3)/M$ where $M = m_1 + m_2 + m_3$, which is equivalent in all frames. The $\boldsymbol{r}$ coordinate specifies the distance between two particles and the $\boldsymbol{R}$ coordinate is the distance from the centre of mass of the two particles to the position of the third particle. Note, cyclic permutation holds for this specific definition of our parameters.

To make this discussion more concise and clear we will describe the basis transformations using matrix notation. In this spirit, equations (4.1) can be expressed as

$$\boldsymbol{\mathcal{K}}_i = \boldsymbol{\Omega}_i \boldsymbol{X}, \quad \text{where, } \boldsymbol{\mathcal{K}}_i = \begin{pmatrix} \boldsymbol{r}_i \\ \boldsymbol{R}_i \\ \boldsymbol{\mathcal{R}} \end{pmatrix} \text{ and } \boldsymbol{X} = \begin{pmatrix} \boldsymbol{x}_1 \\ \boldsymbol{x}_2 \\ \boldsymbol{x}_3 \end{pmatrix}. \tag{4.2}$$

The $\boldsymbol{\Omega}_i$'s are the transformation matrices between the two coordinate systems. For example,

$$\boldsymbol{\Omega}_3 = \begin{pmatrix} 1 & -1 & 0 \\ \dfrac{m_1}{m_1+m_2} & \dfrac{m_2}{m_1+m_2} & -1 \\ \dfrac{m_1}{M} & \dfrac{m_2}{M} & \dfrac{m_3}{M} \end{pmatrix}. \tag{4.3}$$

Using Eq. (4.2), we can obtain the transformation relations between the different Jacobi coordinate systems,

$$\boldsymbol{\mathcal{K}}_i = \boldsymbol{\mathcal{W}}_{ij}\boldsymbol{\mathcal{K}}_j, \quad \text{where } \boldsymbol{\mathcal{W}}_{ij} = \boldsymbol{\Omega}_i\boldsymbol{\Omega}_j^{-1}. \tag{4.4}$$

Therefore, $\boldsymbol{\mathcal{W}}_{ij}$ is a transformation matrix relating frames i and j. As the three-body problem will be specified initially in the 12 basis, we will always want to express $\boldsymbol{\mathcal{K}}_3$ in terms of $\boldsymbol{\mathcal{K}}_1$ or $\boldsymbol{\mathcal{K}}_2$, thus we are mostly interested in matrices $\boldsymbol{\mathcal{W}}_{31}$ and $\boldsymbol{\mathcal{W}}_{32}$. Note, $\boldsymbol{\mathcal{W}}_{ij}$ are 3×3 square matrices with $\det(\boldsymbol{\mathcal{W}}_{ij}) = 1$, also $\boldsymbol{\mathcal{W}}_{ij}$ are not in general orthogonal. In the next section, we will find a set of scaled Jacobi coordinates, such that they will be related by orthogonal transformations.

4.2 Dimensionless Jacobi Coordinates

The dimensionless Jacobi coordinates will be defined as

$$\begin{pmatrix} \boldsymbol{\rho}_i \\ \boldsymbol{\lambda}_i \end{pmatrix} = \begin{pmatrix} \alpha_i & 0 \\ 0 & \beta_i \end{pmatrix} \begin{pmatrix} \boldsymbol{r}_i \\ \boldsymbol{R}_i \end{pmatrix}, \tag{4.5}$$

with α_i and β_i being scale factors having dimension of energy $[E] = \text{GeV}$, making $\boldsymbol{\rho}_i$ and $\boldsymbol{\lambda}_i$ dimensionless. These scale factors have previously been encountered in Eq. (2.20). Note, we are ignoring the c.o.m. coordinate $\boldsymbol{\mathcal{R}}$ which is not important for this discussion.

We now need to find appropriate scale factors α_i and β_i, such that

$$\begin{pmatrix} \boldsymbol{\rho}_i \\ \boldsymbol{\lambda}_i \end{pmatrix} = \boldsymbol{O}_{ij} \begin{pmatrix} \boldsymbol{\rho}_j \\ \boldsymbol{\lambda}_j \end{pmatrix}, \quad \text{where } \boldsymbol{O}_{ij} = \begin{pmatrix} \cos\varphi_{ij} & -\sin\varphi_{ij} \\ \sin\varphi_{ij} & \cos\varphi_{ij} \end{pmatrix}, \tag{4.6}$$

i.e. $\boldsymbol{O}_{ij}$ is an orthogonal transformation matrix relating the dimensionless Jacobi frames i and j. To find the appropriate scale factors α_i and β_i, we will start by truncating the transformation matrix $\boldsymbol{\mathcal{W}}_{ij}$ defined in Eq. (4.4), by removing the elements related to the c.o.m. coordinate, i.e. we will focus only on the upper left 2×2 quadrant of that matrix, which will be denoted as $\boldsymbol{W}_{ij}$. We can decompose $\boldsymbol{W}_{ij}$ as

$$\boldsymbol{W}_{ij} = \boldsymbol{D}_i^{-1} \boldsymbol{O}_{ij} \boldsymbol{D}_j, \tag{4.7}$$

where $\boldsymbol{D}_i$ are diagonal matrices and $\boldsymbol{O}_{ij}$ is the orthogonal matrix defined in (4.6). Using Eq. (4.4) we can write

$$\boldsymbol{K}_i = \boldsymbol{W}_{ij}\boldsymbol{K}_j, \quad \text{where } \boldsymbol{K}_i = \begin{pmatrix} \boldsymbol{r}_i \\ \boldsymbol{R}_i \end{pmatrix}. \tag{4.8}$$

Using the decomposition in Eq. (4.7), we can write (4.8) as

$$\boldsymbol{D}_i\boldsymbol{K}_i = \boldsymbol{O}_{ij}\boldsymbol{D}_j\boldsymbol{K}_j, \tag{4.9}$$

which has the same form as Eq. (4.6) with

$$\boldsymbol{D}_i = \begin{pmatrix} \alpha_i & 0 \\ 0 & \beta_i \end{pmatrix}. \tag{4.10}$$

We now have all the tools ready to obtain the scale factors α_i and β_i. Let us consider an example using the transformation matrix $\boldsymbol{W}_{31}$ to find D_1 and D_3. Using the definition of $\mathcal{W}_{ij}$ in Eq. (4.1), $\boldsymbol{W}_{31}$ is given as

$$\boldsymbol{W}_{31} = \begin{pmatrix} -\dfrac{m_3}{m_2+m_3} & -1 \\ \dfrac{m_2(m_1+m_2+m_3)}{(m_1+m_2)(m_2+m_3)} & -\dfrac{m_1}{m_1+m_2} \end{pmatrix}, \quad \det \boldsymbol{W}_{31} = 1. \tag{4.11}$$

Decomposing $\boldsymbol{W}_{31}$ as prescribed in Eq. (4.7) we have

$$\begin{aligned} \boldsymbol{W}_{31} &= \begin{pmatrix} \frac{1}{\alpha_3} & 0 \\ 0 & \frac{1}{\beta_3} \end{pmatrix} \begin{pmatrix} \cos\varphi_{31} & -\sin\varphi_{31} \\ \sin\varphi_{31} & \cos\varphi_{31} \end{pmatrix} \begin{pmatrix} \alpha_1 & 0 \\ 0 & \beta_1 \end{pmatrix} \\ &= \begin{pmatrix} \frac{\alpha_1}{\alpha_3}\cos\varphi_{31} & -\frac{\beta_1}{\alpha_3}\sin\varphi_{31} \\ \frac{\alpha_1}{\beta_3}\sin\varphi_{31} & \frac{\beta_1}{\beta_3}\cos\varphi_{31} \end{pmatrix}. \end{aligned} \tag{4.12}$$

Constraints:

- In order to preserve the determinant of $\boldsymbol{W}_{31}$ being 1 we require $\det(D_3^{-1}O_{31}D_1) = 1$, yielding the first constraint; $\alpha_1\beta_1 = \alpha_3\beta_3$.

- By interpreting $\boldsymbol{D}_i$ as re-scaling factors, we constrain $\alpha_i, \beta_i \geq 0$, with $i = 1$ and 3.

- By comparing the right hand side of (4.12) with Eq. (4.11) and paying special attention to the signs, we find that φ_{31} lies in the second quadrant, i.e. $\frac{\pi}{2} \leq \varphi_{31} \leq \pi$.

- Similarly, comparing the product of the cross terms in the rhs of Eq. (4.12) and Eq. (4.11) we get

$$\sin^2 \varphi_{31} = \frac{m_2 M}{(m_1 + m_2)(m_2 + m_3)}, \tag{4.13}$$

$$\cos^2 \varphi_{31} = \frac{m_1 m_3}{(m_1 + m_2)(m_2 + m_3)}, \tag{4.14}$$

$$\therefore \ \tan \varphi_{31} = -\sqrt{\frac{m_2 M}{m_1 m_3}}. \tag{4.15}$$

Equation (4.15) gives us a relation for the angle of rotation between frame 3 and frame 1 which is dependent on the masses of the particles.

We can compare the elements of Eq. (4.11) with those in the rhs of Eq. (4.12) to obtain expressions for α_1 and β_1 in terms of α_3, β_3 and the masses,

$$\alpha_1 = -\left(\frac{m_3}{(m_2 + m_3)\cos\varphi_{31}}\right)\alpha_3 = \left(\frac{m_2 M}{(m_1 + m_2)(m_2 + m_3)\sin\varphi_{31}}\right)\beta_3, \tag{4.16}$$

$$\beta_1 = \left(\frac{1}{\sin\varphi_{31}}\right)\alpha_3 = -\left(\frac{m_1}{(m_1 + m_2)\cos\varphi_{31}}\right)\beta_3. \tag{4.17}$$

Now, as long as α_1 and β_1 satisfy equations (4.16) and (4.17), this will ensure that equations (4.6) will also be satisfied, meaning that the transformation between the basis described by $\boldsymbol{\rho}_3$ and $\boldsymbol{\lambda}_3$ and basis described by $\boldsymbol{\rho}_1$ and $\boldsymbol{\lambda}_1$ will be orthogonal. We have mentioned previously that we have already encountered α_i and β_i in Eq. (2.20). Thus, for convenience and following the two-body prescription it will be natural to set

$$\alpha_3 = \sqrt{\mu_r \omega_r}, \quad \beta_3 = \sqrt{\mu_R \omega_R}, \tag{4.18}$$

with μ_r and $\mu_{_R}$ being defined in Eq. (2.34) and ω_r and $\omega_{\rm R}$ are the two size parameters related to the coupled SHO basis functions defined in Eq. (2.21). This choice of α_3 and β_3 fixes α_1 and β_1 via the conditions in Eqs. (4.16) and (4.17).

Following a similar set of steps for $\boldsymbol{W}_{32}$ as was done above for $\boldsymbol{W}_{31}$, we obtain

$$\alpha_2 = -\left(\frac{m_3}{(m_1+m_3)\cos\varphi_{32}}\right)\alpha_3 = -\left(\frac{m_1 M}{(m_1+m_2)(m_1+m_3)\sin\varphi_{32}}\right)\beta_3, \quad (4.19a)$$

$$\beta_2 = -\left(\frac{1}{\sin\varphi_{32}}\right)\alpha_3 = -\left(\frac{m_2}{(m_1+m_2)\cos\varphi_{32}}\right)\beta_3, \quad (4.19b)$$

$$\tan\varphi_{32} = \sqrt{\frac{m_1 M}{m_2 m_3}}, \quad \frac{\pi}{2} \leq \varphi_{32} \leq \pi. \quad (4.19c)$$

We can use any of the Eqs. (4.16), (4.17), (4.19a) or (4.19b) to obtain the relation

$$\left(\frac{\alpha_3}{\beta_3}\right)^2 = -\frac{m_1 m_2 M}{(m_1+m_2)^2 m_3}, \quad (4.20)$$

with the definition of α_3 and β_3 given in (4.18) we find that we must restrict the basis size parameters such that

$$\boxed{\omega_r = \omega_{_R}.} \quad (4.21)$$

We arrive at one of the key differences between our method and the method discussed in Ref. [1], where both parameters (ω_r and ω_R) are allowed to vary independently where as in our work they are constrained to be equal. In our work we will treat both the size parameters as a single parameter, $\omega_r = \omega_{_R} = \omega$. While this restriction may potentially impact the accuracy of our results for less symmetric systems (where particle masses are drastically different [1]), it does result in reduced computation time during optimisation of variational parameters as we only have a single parameter to optimise. In later chapters, we will find good agreement with results found in the literature, indicating that restricting both basis functions to a single size parameter does not significantly compromise accuracy.

To summarise, our main goal was to introduce new sets of Jacobi frames which will

be related by orthogonal transformations. We did this by introducing dimensionless frames described by the variables $\boldsymbol{\rho}_i$ and $\boldsymbol{\lambda}_i$ defined in Eq. (4.5) with α_i and β_i defined in Eqs. (4.16) $\rightarrow$ (4.19b). The angle of rotation that takes us from frame 3 to frame 1 is given by Eq. (4.15) and the angle of rotation from frame 3 to frame 2 is given by Eq. (4.19c).

4.3 Talmi-Moshinsky Transformations

In this section, we will outline the method of transforming any coupled SHO basis wavefunction expressed in the $\boldsymbol{\rho}_3$, $\boldsymbol{\lambda}_3$ basis into the $\boldsymbol{\rho}_i$, $\boldsymbol{\lambda}_i$ basis, with $i = 1, 2$. These are the only transformations we are interested in as we have limited our need to only "one-directional" transformations (from frame $3 \rightarrow 1$ and $3 \rightarrow 2$). In this section, we will drop the index corresponding to frame 3 in order to avoid cluttering. We will refer to $\boldsymbol{\rho}_3$ simply as $\boldsymbol{\rho}$ and to $\boldsymbol{\lambda}_3$ as $\boldsymbol{\lambda}$, in other words, we will drop any index which refers to the "parent" frame. The following is an expansion of an SHO basis function in frame 3 onto frames 1 or 2.

$$\langle \boldsymbol{\rho}, \boldsymbol{\lambda} | nl, NL : \Lambda \rangle = \sum_{n_i l_i N_i L_i} \underbrace{\langle n_i l_i, N_i L_i : \Lambda | nl, NL : \Lambda \rangle}_{\text{Talmi expansion coefficients}} \overbrace{\langle \boldsymbol{\rho}_i, \boldsymbol{\lambda}_i | n_i l_i, N_i L_i : \Lambda \rangle}^{\text{SHO w.f. in new frame}}, \quad (4.22)$$

where $i = 1$ or 2 corresponding to frame 1 and 2. The sum extends over all quantum numbers which are constraint by the condition

$$2n + l + 2N + L = \gamma = 2n_i + l_i + 2N_i + L_i. \quad (4.23)$$

Also, note that the total orbital angular momentum Λ is the same on both sides of Eq. (4.22). Due to these constraints the sum is finite. In Eq. (4.23), γ is proportional to the energy of the coupled SHO basis wavefunction.

The full expression for the Talmi expansion coefficients is given by Buck et al. found

in Ref. [66]. The expression for the Talmi coefficients is a relatively long equation involving many sums, sums over $9j$ symbols as well as Clebsch-Gordan coefficients. It is not so easy to efficiently implement this equation, however, some simplifications can be made by realising that a lot of the quantities are not dependent on any parameters of the coordinate system and thus can be calculated once and stored into memory. Another important fact about this implementation of the Talmi-Moshinsky coefficients is that they are independent of the variational parameter ω meaning they do not need to be recalculated every time the ω changes, this saves a lot of time when applying the variational method when looking for the minimum energy. This is not true in the method proposed in Ref. [1], which states that the Brody-Moshinsky coefficients need to be recalculated each time the size parameters change, costing considerable amount of time during optimisation.

4.4 Three-Body Potential

In this section, we will outline how we deal with the three-body potential by using the Talmi-Moshinsky transformations.

The three-body potential can be divided into three terms as previously seen in Eq. (2.9). Each term corresponds to a single pair of particles. Using the dimensionless Jacobi variables defined in Eq. (4.5), Eq. (2.9) can be expressed as

$$V(\rho, \rho_1, \rho_2) = V_{12}(\frac{\rho}{\alpha}) + V_{23}(\frac{\rho_1}{\alpha_1}) + V_{31}(\frac{\rho_2}{\alpha_2}). \tag{4.24}$$

Note, that ρ and α with no index refer to ρ_3 and α_3, respectively. Our main goal is

to obtain matrix representation of $V(\rho, \rho_1, \rho_2)$ in the 12 SHO basis, defined as

$$\langle \phi^{12}_{i'} | V(\rho_1, \rho_2, \rho_3) | \phi^{12}_{i} \rangle = \langle \phi^{12}_{i'} | V_{12}(\tfrac{\rho}{\alpha}) | \phi^{12}_{i} \rangle + \langle \phi^{12}_{i'} | V_{23}(\tfrac{\rho_1}{\alpha_1}) | \phi^{12}_{i} \rangle + \langle \phi^{12}_{i'} | V_{31}(\tfrac{\rho_2}{\alpha_2}) | \phi^{12}_{i} \rangle. \quad (4.25)$$

The element of $V_{12}(\frac{\rho}{\alpha})$ can be calculated relatively easily without any involvement of switching basis. The problem lies in the two remaining terms in the potential, to solve them we will require to switch basis. Let us take a look at how we can compute the element of $V_{23}(\frac{\rho_1}{\alpha_1})$ in the 12 basis. To do this we will define a basis transformation as

$$|\phi^{12}_{i}\rangle = \sum_{j} |\phi^{23}_{j}\rangle \langle \phi^{23}_{j} | \phi^{12}_{i} \rangle, \quad (4.26)$$

the expansion coefficients $\langle \phi^{23}_{j} | \phi^{12}_{i} \rangle$ are nothing else but the Talmi transformation coefficients defined earlier in Eq. (4.22). We would like to note here that in later chapters, when we come to include spin in our models, the basis functions $|\phi^{12}_{i}\rangle$ will in general be wavefunctions containing both spin and spatial degrees of freedom, thus the expansion coefficients $\langle \phi^{23}_{j} | \phi^{12}_{i} \rangle$, will be slightly more complicated than here, but for now they are simply the Talmi-Moshinsky coefficients. Using (4.26), we can write

$$\langle \phi^{12}_{i'} | V_{23}(\tfrac{\rho_1}{\alpha_1}) | \phi^{12}_{i} \rangle = \sum_{j'j} \langle \phi^{12}_{i'} | \phi^{23}_{j'} \rangle \langle \phi^{23}_{j'} | V_{23}(\tfrac{\rho_1}{\alpha_1}) | \phi^{23}_{j} \rangle \langle \phi^{23}_{j} | \phi^{12}_{i} \rangle, \quad (4.27)$$

we will next make use of the property of dummy indices, i.e.

$$\langle \phi^{23}_{i'} | V_{23}(\tfrac{\rho_1}{\alpha_1}) | \phi^{23}_{i} \rangle = \langle \phi^{12}_{i'} | V_{12}(\tfrac{\rho}{\alpha_1}) | \phi^{12}_{i} \rangle, \quad (4.28)$$

which is a simple index permutation, note that the index on the α remains the same, as it is a parameter and not a variable. Also, note that the ρ with no index is referring to ρ_3. We can use (4.28) to rewrite (4.27) as

$$\langle \phi^{12}_{i'} | V_{23}(\tfrac{\rho_1}{\alpha_1}) | \phi^{12}_{i} \rangle = \sum_{j'j} \langle \phi^{12}_{i'} | \phi^{23}_{j'} \rangle \langle \phi^{12}_{j'} | V_{12}(\tfrac{\rho}{\alpha_1}) | \phi^{12}_{j} \rangle \langle \phi^{23}_{j} | \phi^{12}_{i} \rangle. \quad (4.29)$$

We want to transform Eq. (4.29) into a matrix form. To do that, we will first write Eq. (4.26) in matrix form

$$\phi^{12} = t_1 \phi^{23}, \tag{4.30}$$

where

$$\phi^{12} \equiv \begin{pmatrix} |\phi_1^{12}\rangle \\ |\phi_2^{12}\rangle \\ \vdots \end{pmatrix}, \quad \phi^{23} \equiv \begin{pmatrix} |\phi_1^{23}\rangle \\ |\phi_2^{23}\rangle \\ \vdots \end{pmatrix}, \tag{4.31}$$

and

$$t_1 \equiv \begin{pmatrix} \langle\phi_1^{23}|\phi_1^{12}\rangle & \langle\phi_1^{23}|\phi_2^{12}\rangle & \dots \\ \langle\phi_2^{23}|\phi_1^{12}\rangle & \langle\phi_2^{23}|\phi_2^{12}\rangle & \dots \\ \vdots & \vdots & \end{pmatrix}, \tag{4.32}$$

where t_1 is the matrix containing the Talmi-Moshinsky coefficients defined in (4.22). Note that that the subscript on t_1 is chosen because it is the matrix which transforms the spatial basis functions from frame 3 to frame 1. This matrix will be referred to as the Talmi transformation matrix. By analogy, the Talmi transformation matrix which transforms the spatial basis functions from frame 3 to 2 will be denoted as t_2 and will have the form

$$t_2 \equiv \begin{pmatrix} \langle\phi_1^{31}|\phi_1^{12}\rangle & \langle\phi_1^{31}|\phi_2^{12}\rangle & \dots \\ \langle\phi_2^{31}|\phi_1^{12}\rangle & \langle\phi_2^{31}|\phi_2^{12}\rangle & \dots \\ \vdots & \vdots & \end{pmatrix}. \tag{4.33}$$

Lastly, we will define

$$V_{12}(\alpha) \equiv \begin{pmatrix} \langle\phi_1^{12}|V_{12}(\frac{\rho}{\alpha})|\phi_1^{12}\rangle & \langle\phi_1^{12}|V_{12}(\frac{\rho}{\alpha})|\phi_2^{12}\rangle & \dots \\ \langle\phi_2^{12}|V_{12}(\frac{\rho}{\alpha})|\phi_1^{12}\rangle & \langle\phi_2^{12}|V_{12}(\frac{\rho}{\alpha})|\phi_2^{12}\rangle & \dots \\ \vdots & \vdots & \end{pmatrix}, \tag{4.34}$$

which is the matrix representation of the potential between particles 1 and 2 in the $|\phi_i^{12}\rangle$ basis for a varying parameter α. Then we can use (4.30) and (4.34) to write

(4.29) in matrix form as

$$V_{23} = t_1^T V_{12}(\alpha_1) t_1, \tag{4.35}$$

where V_{23} is the matrix representation of $V_{23}(\frac{\rho_1}{\alpha_1})$ in the $|\phi_i^{12}\rangle$ basis. The Talmi transformation matrices t_1 are used to transform $V_{12}(\alpha_1)$ to V_{23}. Similarly, we can also obtain

$$V_{31} = t_2^T V_{12}(\alpha_2) t_2. \tag{4.36}$$

Altogether, the total potential in matrix form reads

$$V = V_{12}(\alpha) + t_1^T V_{12}(\alpha_1) t_1 + t_2^T V_{12}(\alpha_2) t_2. \tag{4.37}$$

Note, that the Talmi transformation matrices t_1 and t_2 are doing all the heavy-lifting. We only need to compute the matrix representation of the $V_{12}(\alpha)$ operator in the 12 SHO basis for different parameters; α, α_1 and α_2, and the matrices t_1 and t_2 take care of the rest. Since, V_{12} is a two-body potential, we have effectively turned a complicated three-body problem into three copies of the two-body problem.

Lastly, to obtain the 12 representation of a general operator element expressed in the 23 basis, we can use the Talmi-Moshinsky transformations as follows

$$\langle \phi_{i'}^{12} | \mathcal{O}(\rho_1, \lambda_1; \alpha_1, \beta_1) | \phi_i^{12} \rangle = \sum_{j'j} \langle \phi_{i'}^{12} | \phi_{j'}^{23} \rangle \langle \phi_{j'}^{12} | \mathcal{O}(\rho, \lambda; \alpha_1, \beta_1) | \phi_j^{12} \rangle \langle \phi_j^{23} | \phi_i^{12} \rangle, \tag{4.38}$$

where we have used similar logic that took us from Eq. (4.27) $\rightarrow$ (4.29), and where j' and j are the same summation variables present in Eq. (4.22) obeying the same conditions. Similarly, to obtain the 12 representation of an operator expressed in the 31 basis, its element can be obtained as follows,

$$\langle \phi_{i'}^{12} | \mathcal{O}(\rho_2, \lambda_2; \alpha_2, \beta_2) | \phi_i^{12} \rangle = \sum_{j'j} \langle \phi_{i'}^{12} | \phi_{j'}^{31} \rangle \langle \phi_{j'}^{12} | \mathcal{O}(\rho, \lambda; \alpha_2, \beta_2) | \phi_j^{12} \rangle \langle \phi_j^{31} | \phi_i^{12} \rangle. \tag{4.39}$$

For example, let us say we wanted to represent an element of the $r_1 = \frac{\rho_1}{\alpha_1}$ operator, in the 12 SHO basis. It is one of many operators which can appear in the $V_{23}(\frac{\rho_1}{\alpha_1})$ term

describing the force between particles 2 and 3. Using Eq. (4.38), we have

$$\langle \phi^{12}_{i'} | \frac{\rho_1}{\alpha_1} | \phi^{12}_{i} \rangle = \sum_{j'j} \langle \phi^{12}_{i'} | \phi^{23}_{j'} \rangle \langle \phi^{12}_{j'} | \frac{\rho}{\alpha_1} | \phi^{12}_{j} \rangle \langle \phi^{23}_{j} | \phi^{12}_{i} \rangle, \tag{4.40}$$

where the element $\langle \phi^{12}_{j'} | \frac{\rho}{\alpha_1} | \phi^{12}_{j} \rangle$ can be easily computed with the aid of Eq. (2.44). Similarly, for the $r_2 = \frac{\rho_2}{\alpha_2}$ operator, we can use Eq. (4.39) to get

$$\langle \phi^{12}_{i'} | \frac{\rho_2}{\alpha_2} | \phi^{12}_{i} \rangle = \sum_{j'j} \langle \phi^{12}_{i'} | \phi^{31}_{j'} \rangle \langle \phi^{12}_{j'} | \frac{\rho}{\alpha_2} | \phi^{12}_{j} \rangle \langle \phi^{31}_{j} | \phi^{12}_{i} \rangle. \tag{4.41}$$

All of the equations (4.38), (4.39), (4.40) and (4.41) can be expressed in matrix notation by "packaging" the Talmi-Moshinsky coefficients into a matrix as defined in Eqs. (4.32) and (4.33). So, instead of performing the transformations on individual elements, we can use the t_1 (t_2) matrix to obtain the 12 representation of an operator expressed in the 23 (31) basis. Such that,

$$\overbrace{\mathcal{O}^{12}(\rho_1, \lambda_1; \alpha_1, \beta_1)}^{\text{matrix}} = \overbrace{t_1^T \mathcal{O}^{12}(\rho, \lambda; \alpha_1, \beta_1) t_1}^{\text{product of three matrices}}, \tag{4.42}$$

where $\mathcal{O}^{12}(\rho_1, \lambda_1; \alpha_1, \beta_1)$ is the matrix representation of the $\mathcal{O}(\rho_1, \lambda_1; \alpha_1, \beta_1)$ operator in the 12 basis. Equation (4.42) is the matrix form of Eq. (4.38). And for an operator expressed in the 31 basis, we have

$$\mathcal{O}^{12}(\rho_2, \lambda_2; \alpha_2, \beta_2) = t_2^T \mathcal{O}^{12}(\rho, \lambda; \alpha_2, \beta_2) t_2. \tag{4.43}$$

4.5 Ordering of SHO Basis Functions

In this section, we will describe how we order the coupled SHO basis functions for the three-body problem. The scheme for which basis states will be used in the calculations depends on the properties of Talmi-Moshinsky transformations which conserve the

γ	$\{n,l,N,L\}$ combinations
0	{0,0,0,0}
2	{0,0,1,0}, {0,1,0,1}, {1,0,0,0}
4	{0,0,2,0}, {0,1,1,1}, {0,2,0,2}, {1,0,1,0}, {1,1,0,1}, {2,0,0,0}
⋮	⋮

Table 4.1: Possible n, l, N and L combinations given a value of γ for positive space parity ($P = +1$) states coupled to total orbital angular momentum $\Lambda = 0$.

γ	$\{n,l,N,L\}$ combinations
1	{0,0,0,1}, {0,1,0,0}
3	{0,0,1,1}, {0,1,0,2}, {0,1,1,0}, {0,2,0,1}, {1,0,0,1}, {1,1,0,0}
⋮	⋮

Table 4.2: Possible n, l, N and L combinations given a value of γ for negative space parity ($P = -1$) states coupled to total orbital angular momentum $\Lambda = 1$.

energy of the coupled SHO wavefunction $\gamma = 2n+2N+l+L$, space-parity $P = (-1)^{l+L}$ and total orbital angular momentum Λ. When generating a set of SHO basis functions for our computations, we must therefore, specify the spatial parity P, the total orbital angular momentum Λ and γ_{max} (the maximum energy of states we want to consider), and in return we receive all the basis functions which satisfy those criteria.

For example, if we want to generate a set of coupled SHO basis functions for a positive space-parity state with total orbital angular momentum $\Lambda = 0$, and we only want to use basis states up to $\gamma_{max} = 4$, this will give us all the states in Table 4.1 with $\gamma \leq 4$ which yields a total of 10 spatial basis functions.

On the contrary, for an odd parity state, with $\Lambda = 1$ and for $\gamma_{max} = 3$, we will have all the states found in Tab. 4.2 with $\gamma \leq 3$ yielding 8 spatial basis states.

Our basis functions will be ordered according to their γ value. If we want to include more basis states for our calculations we simply increase the value of γ_{max}. We must note that although, including more basis functions yields better approximations, it significantly increases computation time. Note also that the number of spatial basis

functions is "quantised", in the sense that we cannot use any number of spatial basis functions for our approximations but only fixed amounts which are dependent on the choice of P, Λ and γ_{max}, some examples are shown in Fig. 4.1.

P	Λ	γ_{max}	N_ϕ
+1	0	0	1
+1	0	2	4
+1	0	4	10
+1	0	6	20

P	Λ	γ_{max}	N_ϕ
-1	1	1	2
-1	1	3	8
-1	1	5	20
-1	1	7	40

Figure 4.1: Number of basis functions N_ϕ for various combinations of P, Λ and $\gamma_{\max}$. On the left are states with positive space-parity and on the right negative space-parity states.

You might also note that we always go up in steps of $\gamma = 2$, as in Fig. 4.1. This is because there are zero basis states with positive spatial parity and an odd γ value, and vice-versa for negative space-parity states. Hence, it only makes sense that γ values go up by two.

5

Simple Harmonic Oscillator Potential Tests

In this chapter, we will perform a series of tests to ensure the robustness of our method for solving three-body quantum mechanical systems. In this test case, we will be solving the three-body quantum harmonic oscillator potential model. We have chosen this as our test case due to its simple nature, and mainly because there exist analytical solutions for this system. We will solve this model both analytically and numerically using the techniques discussed in Ch. 4 to test our numerical method. The tests will consist of comparing our numerical predictions of various observables, such as the spectrum of the model, expectation values of the root mean square radii between different pairs of particles in the system and the expectation value of the wavefunction at the origin, against their analytical solutions. We will also investigate the eigenvectors predicted by our numerical method and we will check whether we are able to numerically satisfy the virial theorem.

Accurately predicting the analytical solutions for this system will serve as strong validation that our numerical method is effective, which will be useful as we move on to attempting to solve more complex three-body systems.

5.1 Three-Body Harmonic Oscillator Potential

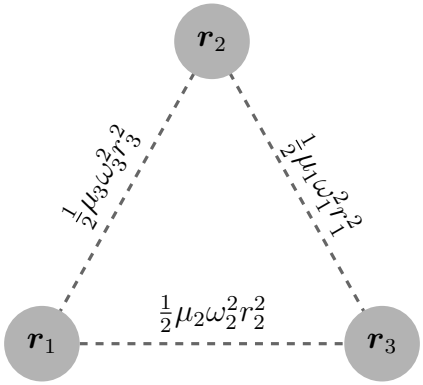

Figure 5.1: A system of three bodies held together by simple harmonic potentials where ω_1, ω_2 and ω_3 are allowed to have different values.

In this section, we will outline the Hamiltonian for the three-body simple harmonic oscillator and describe how we will solve it numerically as well as analytically.

Each pair of particles ij in the system will be joined by a simple harmonic oscillator potential defined as

$$V_{ij}^{\text{SHO}}(r_k) = \frac{1}{2}\mu_k \omega_k^2 r_k^2, \tag{5.1}$$

where,

$$\mu_k = \frac{m_i m_j}{m_i + m_j}. \tag{5.2}$$

The potential in Eq. (5.1) acts between each pair of particles as illustrated in Fig. 5.1. Note that ω_k can be different for different pairs of particles and that the ω_k's we see here are different from the ω previously seen, for example in Sec. 3.4, where it was used to denote the variational/size parameter of the SHO basis wavefunctions used for the numerical method. Here, the ω_k's are used to denote the "strength" of the "springs" holding the particles in the system together. The reason for allowing different ω_k's is because the model can be easily solved analytically when the ω_k's take up special values, more on this soon.

Previously, in Eq. (2.33) we have obtained the general form for a three-body Hamiltonian expressed in Jacobi coordinates. We can substitute the SHO potential specified in Eq. (5.1) to get the three-body SHO Hamiltonian, which reads

$$H_{\text{SHO}} = \sum_{i=1}^{3} m_i + \frac{\boldsymbol{p}_r^2}{2\mu_r} + \frac{\boldsymbol{p}_{\text{R}}^2}{2\mu_{\text{R}}} + \frac{1}{2}\Big(\mu_3\omega_3^2 r_3^2 + \mu_1\omega_1^2 r_1^2 + \mu_2\omega_2^2 r_2^2\Big), \tag{5.3}$$

where μ_r and μ_{R} are defined in Eq. (2.34).

For the purpose of solving the three-body SHO system analytically, we will modify Eq. (5.3) by expressing the potential in terms of the Jacobi coordinates r_3 and R_3, the reason for this will soon become clear. To do this let us introduce the following relations

$$\begin{aligned} \boldsymbol{r}_1 &= -\frac{m_1}{m_1+m_2}\boldsymbol{r}_3 + \boldsymbol{R}_3, \\ \boldsymbol{r}_2 &= -\frac{m_2}{m_1+m_2}\boldsymbol{r}_3 - \boldsymbol{R}_3. \end{aligned} \tag{5.4}$$

If we substitute in Eqs. (5.4) into Eq. (5.3) we see that cross terms proportional to $\boldsymbol{r}_3\boldsymbol{R}_3$ would arise due to the r_1^2 and r_2^2 terms in Eq. (5.3). What we would like is a Hamiltonian that can be expressed with out the cross-terms in the following way,

$$H_{\text{SHO}} = \sum_{i=1}^{3} m_i + \frac{\boldsymbol{p}_r^2}{2\mu_r} + \frac{\boldsymbol{p}_{\text{R}}^2}{2\mu_{\text{R}}} + \frac{1}{2}\mu_r w_r^2 r_3^2 + \frac{1}{2}\mu_{\text{R}} w_{\text{R}}^2 R_3^2, \tag{5.5}$$

where w_r and w_{R} are to be determined. The cross-terms can be eliminated by imposing the following constraint

$$\omega_2 = \omega_1 \left(\frac{m_1+m_3}{m_2+m_3}\right)^{1/2}, \tag{5.6}$$

note that there are no constraints on ω_3. This was the reason for introducing the three different ω_i's. Moving on, we can use Eqs. (5.4) together with the constraint in Eq. (5.6) to find that

$$w_r = \sqrt{\frac{2c_r}{\mu_r}}, \quad w_{\text{R}} = \sqrt{\frac{2c_{\text{R}}}{\mu_{\text{R}}}}, \tag{5.7}$$

where

$$c_r = \frac{m_1 m_2(m_3\omega_1^2 + (m_2+m_3)\omega_3^2)}{2(m_1+m_2)(m_2+m_3)}, \quad c_{\text{R}} = \frac{(m_1+m_2)m_3\omega_1^2}{2(m_2+m_3)}. \tag{5.8}$$

Having obtained the desired form of the Hamiltonian in Eq. (5.5), we see that it can be separated out into two separate two-body simple harmonic oscillators. Since the spectrum of a single two-body harmonic oscillator is given by Eq. (2.29), therefore, in this special case where the system is constrained by Eq. (5.6) the energy of the the three-body SHO system is simply given as a sum of two two-body SHO systems,

$$E_{\text{SHO}} = w_r(2n + l + \tfrac{3}{2}) + w_{\text{R}}(2N + L + \tfrac{3}{2}). \tag{5.9}$$

We can now use the analytically derived spectrum to produce a set of energies and test them against our numerical approach.

For the numerical approach, we will express the kinetic part of the Hamiltonian in Eq. 5.3 in terms of the SHO spectrum, similarly as has previously been done to arrive at Eq. (2.35). However, we can now use the property from Eq. (4.21), namely, $\omega_r = \omega_{\text{R}} = \omega$, to write (5.3) as

$$\begin{aligned} H_{\text{SHO}} = \sum_{i=1}^{3} m_i + \omega(2n + l + \tfrac{3}{2}) - \tfrac{1}{2}\mu_r\omega^2 r_3^2 \\ + \omega(2N + L + \tfrac{3}{2}) - \tfrac{1}{2}\mu_{\text{R}}\omega^2 R_3^2 \\ + \frac{1}{2}\Big(\mu_3\omega_3^2 r_3^2 + \mu_1\omega_1^2 r_1^2 + \mu_2\omega_2^2 r_2^2\Big), \end{aligned} \tag{5.10}$$

where ω is the variational parameter used for the variational method and is different from ω_i's which are parameters of the potential. This will be the Hamiltonian used for our numerical method which is just the three-body SHO Hamiltonian but expressed in a way that is more efficient for our code.

We can now use our variational method and see how well we are able to reproduce the analytical spectrum of the three-body SHO system.

m_1	m_2	m_3	ω_1	ω_3	Λ	w_r	w_{R}	E(1S1S)	E(1S2S)	E(1D1D)
1	1	1	1	1	0	$\sqrt{3/2}$	$\sqrt{3/2}$	3.67423	6.12372	8.57321

Table 5.1: Parameters for the three-body SHO Hamiltonian plus analytically obtained energies of some states. Λ is the total angular momentum.

5.2 Equal Mass Tests

In this section, we will start with the most trivial case, we will be investigating various three-body SHO observables when the masses of all particles are identical ($m_1 = m_2 = m_3 = 1$). For this section we will also set $\omega_1 = \omega_3 = 1$, note that ω_2 is fixed according to Eq. (5.6). Given this choice of parameters we find that $w_r = w_{\mathrm{R}} = \sqrt{3/2}$. The analytically derived energy spectrum as defined by Eq. (5.9) is then given as,

$$E_{\text{equal-mass}} = \sqrt{\frac{3}{2}}(2n + l + \frac{3}{2}) + \sqrt{\frac{3}{2}}(2N + L + \frac{3}{2}). \tag{5.11}$$

We have used the above equation to obtain a few bound state energies and have recorded them in Tab. 5.1. We will use our numerical method to compute the energies of the same states and see whether they agree. The accuracy of our predictions will depend mainly on the number of spatial basis functions N_Q. We expect that including more basis functions will result in more accurate predictions of observables. We will plot the energies as a function of the variational parameter ω and we expect there to be an optimum value of ω which minimises the energy.

5.2.1 Energy Tests

In this section we will be checking whether our numerical method can reproduce the analytically derived energies presented in Tab. 5.1. In Fig. 5.2 we plot our numerical

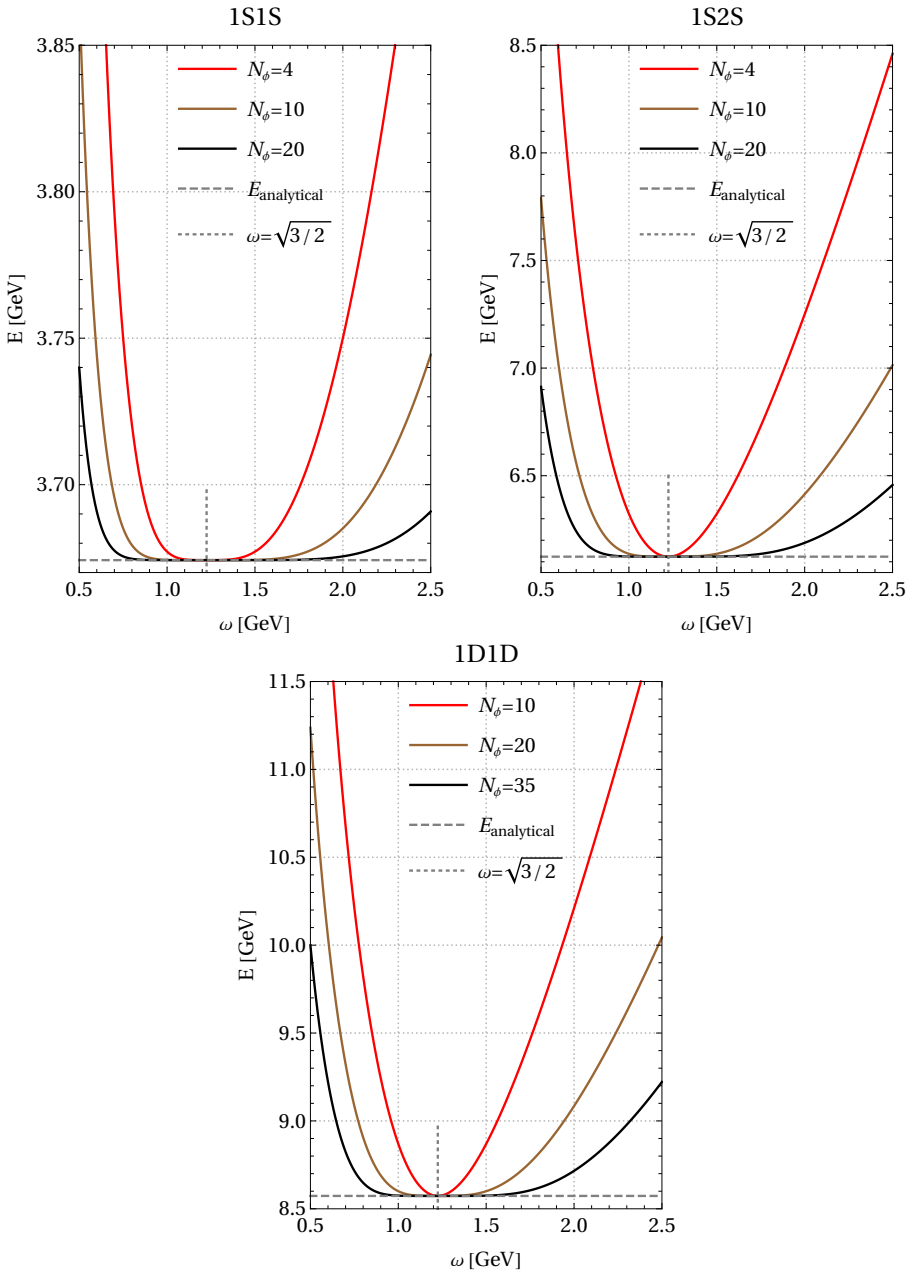

Figure 5.2: Plots of eigenvalues as obtained by the code as a function of ω for different numbers of basis functions N_Q. The more states we consider the better the approximation becomes and the less dependent on ω it is.

predictions of energies for the three different states as a function of ω for three different numbers of basis functions N_Q. In each state, we have also plotted a reference line that corresponds to the analytical value of that state's energy. We can see, that for each state our numerical method is able to reproduce the correct value of energy, i.e. the minimum energy coincides with the analytical value of the states energy. Moreover, when the variational parameter $\omega = \sqrt{3/2}$, we are able to exactly match the analytical solution. We can see that our predictions agree with the analytically derived energy around the region of $\omega = \sqrt{3/2}$, the region gets larger as we increase the number of basis functions. Therefore, the more basis functions we include in our calculation the less dependant the model is on the value of ω. This is in agreement with our expectations as for an infinite number of basis functions we expect the eigenvalues to be independent of ω.

5.2.2 Eigenvector Tests

In this section, we will investigate the behaviour of the components of eigenvectors produced by our numerical method. We obtain the eigenvectors by diagonalising the Hamiltonian matrix expressed in the SHO basis. The eigenvectors represent the components of each basis function used in the numerical approximation. For example, if we use ten basis functions to approximate the wavefunction of the 1S1S three-body SHO bound state we expect the contribution from the 1S1S basis function to be the largest and the contributions from other basis functions, such as the 1S2S or 1P1P to be significantly smaller. In Fig. 5.3, we plot the numerically obtained eigenvector components of the 1S1S three-body SHO bound state for different values of the variational parameter ω. In the final plot (bottom right) we focus on the 1S1S component of the eigenvector only, to see how its value depends on ω. In the figure, we can see how the Hamiltonian slowly becomes diagonal when $\omega \to \sqrt{3/2}$. Specifically, we see that the contribution of the 1S1S basis function is exactly 1 when

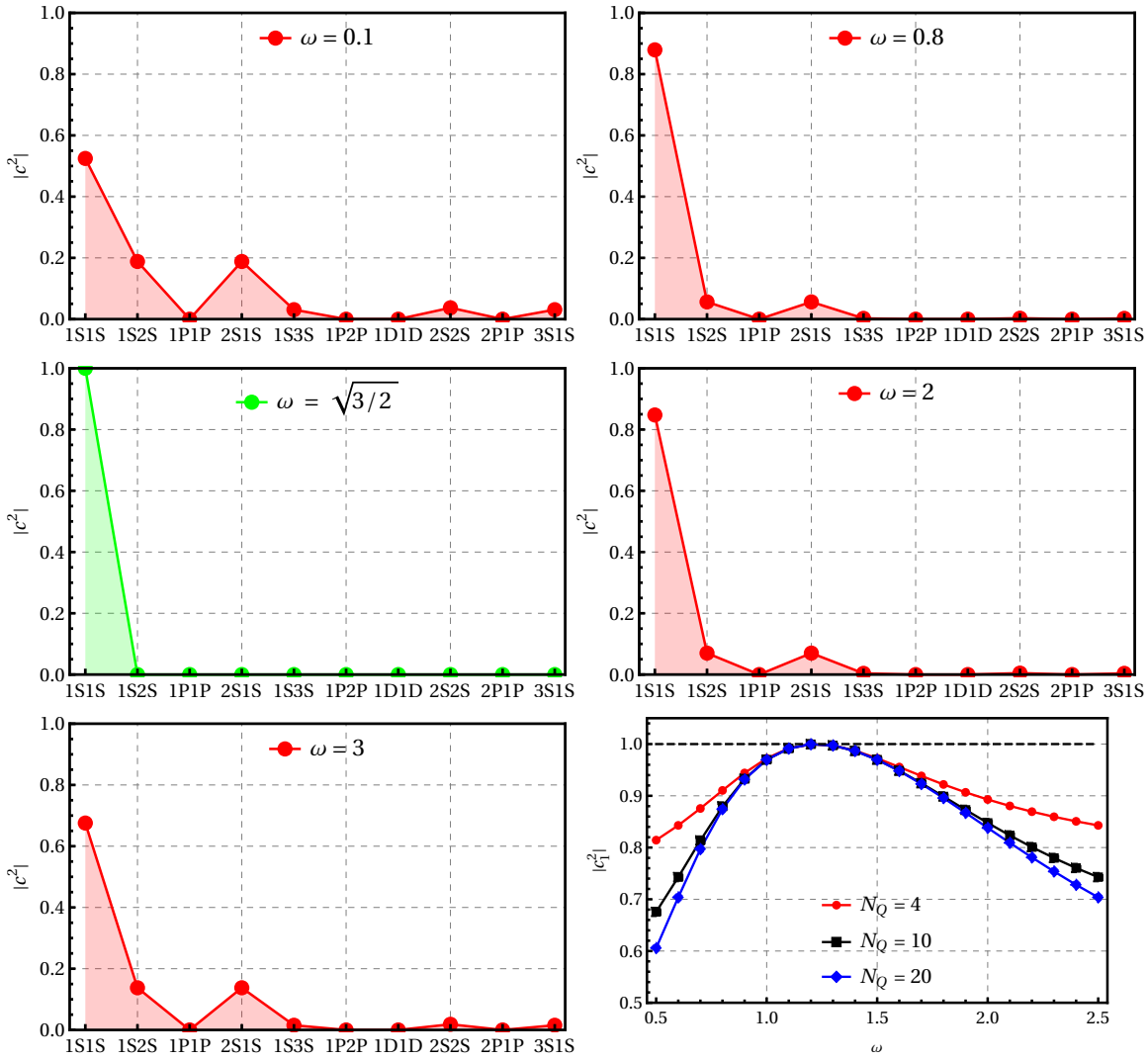

Figure 5.3: Eigenvector components of the 1S1S state as computed by the code. First five graphs plot all eigenvector components for specific values of ω. The last graph contains plots of only the first component as a function of ω for different numbers of basis functions.

the variational parameter $\omega = \sqrt{3/2}$, i.e. no other basis function contributes to the states eigenfunction (the Hamiltonian becomes diagonal at that point). In the plot where we focus only on the 1S1S component of the eigenvector we see that as we increase the number of basis functions, the curves become more sharply peaked about $\omega = \sqrt{3/2}$. This could be explained by the fact that there are more possible non-zero eigenvector components when we include more basis functions. In other words, had we only used a single basis function (the 1S1S basis function) then the contribution from it would of course be largest, but as we start adding more basis functions then the contribution from the 1S1S state must diminish given that the contribution from other basis functions are non-zero. This is why the curves in the last plot become sharper as we increase the number of basis states.

From the analysis of the 1S1S eigenvector and its components as illustrated in Fig. 5.3 we see that the eigenvector behaves as expected for varying values of ω and for increasing number of basis functions. However, same is not true for the excited states in the equal mass case. We would like to comment on an interesting observation when investigating the components of eigenvectors of excited states in the equal mass case. We find that the eigenvector components of the excited states fluctuate discontinuously as we vary ω. We believe this happens due to the degeneracy between the states when all particle masses are the same. We illustrate this behaviour in Fig. 5.4, where we plot the absolute square of the components of the 1S2S eigenvector as a function of the size-parameter ω. We only show the components whose energy matches the energy of the eigenfunction, i.e. only the contribution from the 1S2S, 1P1P and 2S1S SHO basis states. We also plot the sum of their components as a black line which we see is continuous. We also mark the point where $\omega = \sqrt{3/2}$ and where $|c^2| = 1$. In the plot we find that the 1S2S and 2S1S components, represented by the green and red dashed lines overlap and do not exceed $|c^2| = 0.5$ and the 1P1P component contributes most when the 1S2S and 2S1S components are contributing least. When we set $\omega = \sqrt{3/2}$ we find that the 1S2S component becomes equal to one and all other components become null, which is the expected behaviour. What is

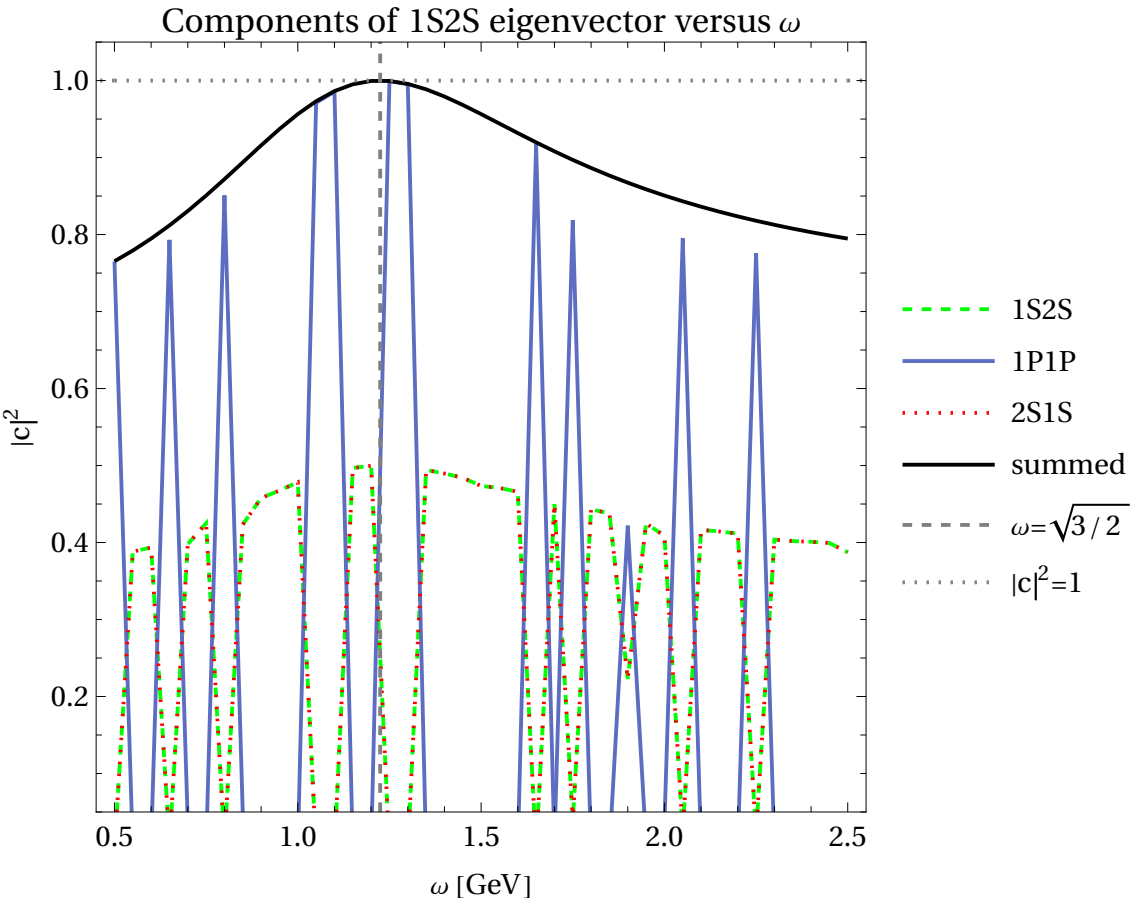

Figure 5.4: Plot of components of the 1S2S eigenvector as a function of ω for the equal mass case.

not expected is the discontinuity but as mentioned previously this behaviour is only found in the equal mass case and has no effect on the energy of excited states.

5.2.3 Root Mean Square Radius Test

In this section, we will be investigating the expectation value of the root mean square (r.m.s.) radius of the 12 pair of particles. We will obtain the expectation value analytically as well as numerically and see how the two compare. We define the r.m.s. radius of particles 1 and 2 as $\langle r_3^2 \rangle^{1/2}$. For a general observable, its expectation

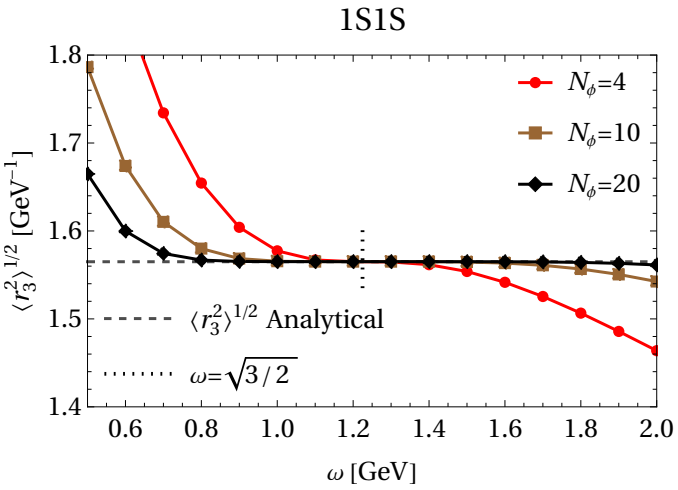

Figure 5.5: Plot of the expectation values of r.m.s. radius for the three identical pairs of particles in the system as a function of ω for the 1S1S state and for different numbers of quanta.

value is given by,

$$\langle \mathcal{O} \rangle = \langle \Psi | \mathcal{O} | \Psi \rangle = \sum_{\substack{n'l'N'L' \\ nlNL}} \langle \Psi | n'l'N'L' \rangle \langle n'l'N'L' | \mathcal{O} | nlNL \rangle \langle nlNL | \Psi \rangle, \tag{5.12}$$

which is the operator matrix represented in the SHO basis, sandwiched between the eigenvectors of the system's Hamiltonian also represented in the SHO basis. Numerically, we are able obtain the expectation value as a function of the variational parameter ω. Analytically, the expectation value of r_3^2 can be obtained using Eq. (2.44). For the 1S1S state, where $\omega_r = \sqrt{3/2}$ we get $\langle r_3^2 \rangle^{1/2} = 1.565\text{GeV}^{-1}$. In Fig. 5.5 we plot the analytical result as a dashed horizontal line. We find that our numerical method accurately predicts the expectation value. We also find that the approximation becomes less dependent on on the variational parameter as the number of basis functions N_ϕ increases.

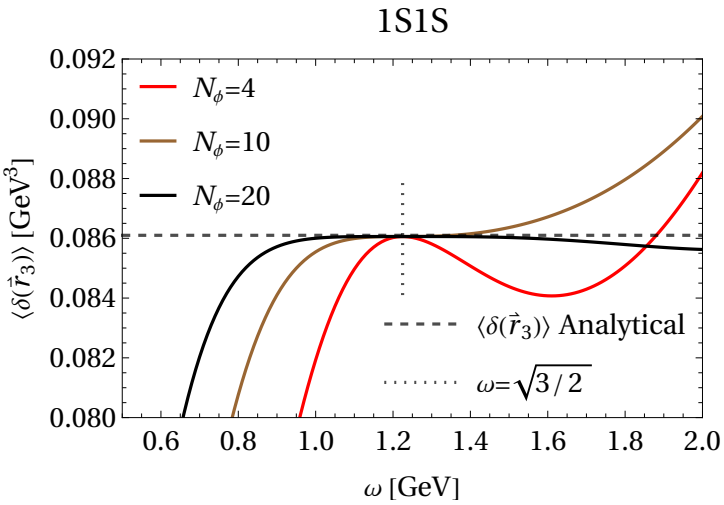

Figure 5.6: Plot of expectation value of the delta operator for the 1S1S state as function of ω and for different number of basis functions. This plot is conjugate to particle pair $\{1, 2\}$.

5.2.4 Wave Function at the Origin

In this section, we will test our numerical method to see if we can predict the correct value of the wave function at the origin for the 12 pair of particles defined as $\langle\delta^{(3)}(r_3)\rangle$. Analytically, we can obtain the expectation value of the δ operator using Eq. (2.56). In the equal mass case, for the 1S1S state $\delta^{(3)}(r_3) = 0.0861\text{GeV}^3$. In Fig. 5.6 we plot the analytical value as a horizontal dashed line along with the numerical predictions for different numbers of basis functions N_ϕ. We find that we are able to accurately reproduce the analytical result at the optimum value of the variational parameter $\omega = \sqrt{3/2}$.

5.3 Unequal Mass Tests

$$E_{\text{unequal-mass}} = 2\sqrt{\frac{2}{5}}(2n + l + \frac{3}{2}) + \sqrt{\frac{6}{5}}(2N + L + \frac{3}{2}). \tag{5.13}$$

m_1	m_2	m_3	ω_1	ω_3	ω_r	ω_{R}	E(1S1P)	E(1P1D)
1	2	3	1	1	$2\sqrt{2/5}$	$\sqrt{6/5}$	4.63598	6.99634

Table 5.2: Unequal mass simple harmonic oscillator potential parameters plus analytically determined energies of states 1S1P and 1P1D.

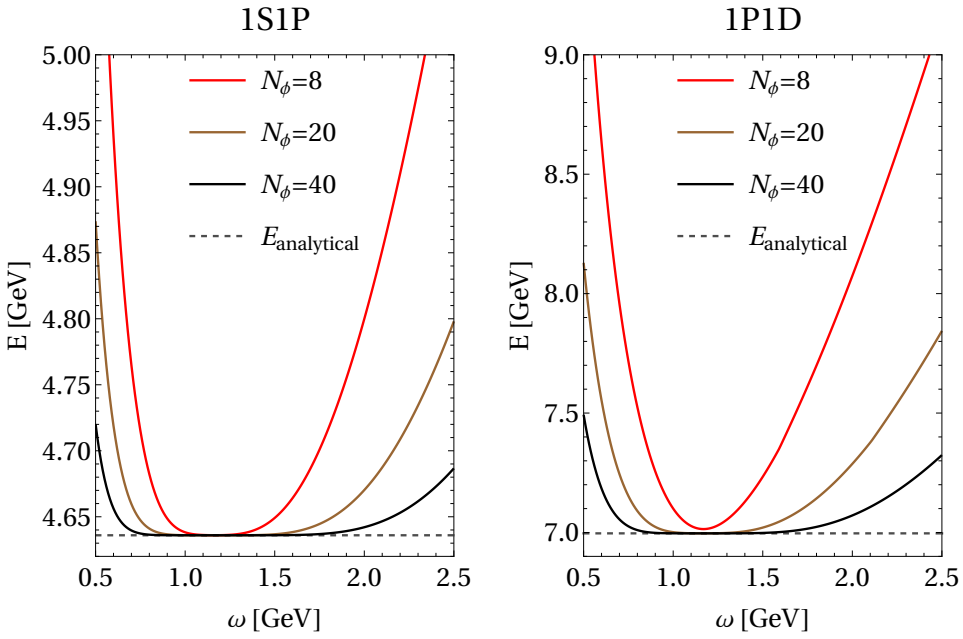

Figure 5.7: Plots of eigenvalues as computed by the code for states 1S1P and 1P1D as functions of ω and for different number of basis functions N_ϕ.

In this section, we will move away from the trivial, equal-mass case and test our numerical method when all the particle masses are different. The parameters that will be used for the unequal mass case are given in Tab. 5.2 along with computed values of ω_r, ω_{R} and the energies of two different bound states. We want to obtain the masses of those states using our numerical method and check how they compare with the analytical results. We will also be looking at various other observables like we did in the equal mass case and ensure that we are able to obtain expectation values that agree with analytical results in the unequal mass case.

5.3.1 Energy Tests

In this subsection, we compare the energies of two SHO bound states obtained numerically and analytically. In Fig. 5.9 we plot the energy of the states as a function of the variational parameter ω for different numbers of SHO basis functions N_ϕ. We also mark the analytical value of the energy for each state as a dashed line. We find that our numerical method is able to predict the correct energy of the state and its accuracy improves as we include more basis functions.

We want to comment on the plot on the right in Fig. 5.7. When we only use 8 basis functions we can see a small gap between the analytical and numerical predictions of the energy. In other words, there is no value of ω where the two are equal. If we recall back to the equal mass case we found that at the value of $\omega = \sqrt{3/2}$ our code was able to exactly reproduce the analytical result. However, in the unequal case this is no longer the case. Instead, we get an upper bound of the energy, we really see the variational method at play, where the numerical prediction lies above the true (analytical) value and as we increase the number of basis functions we get closer to the true value. The reason we see this here and not in the equal mass case is because in the equal mass case we had $\omega_r = \omega_{\mathrm{R}}$ and we were able to match that with our variational parameter ω, in the unequal mass case this is no longer possible since $\omega_r \neq \omega_{\mathrm{R}}$.

5.3.2 Eigenvector Test

In Fig. 5.8 we plot the 1S1P eigenvector component of the 1S1P SHO bound state for the unequal mass case as a function of ω for different numbers of basis functions. We find that, similarly as with the energy plots in previous subsection, none of the lines actually touch the horizontal dashed line corresponding to $|c_1^2| = 1$. This is expected

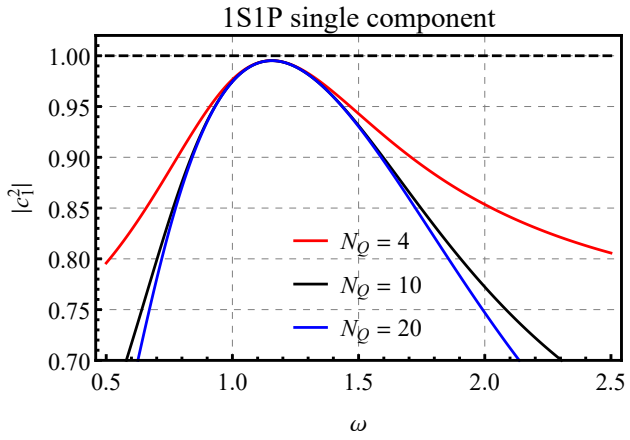

Figure 5.8: Dominating eigenvector component (1S1P) of the 1S1P SHO bound state as function of ω for different numbers of basis functions.

since, again, $\omega_r \neq \omega_{\mathrm{R}}$. Besides that, the component has similar behaviour as in the equal mass case, see Fig. 5.3.

5.3.3 Root Mean Square Radius

In this subsection, we will test our numerical method for obtaining the expectation value of the r.m.s. radius between particles 1 and 2 $\langle r_3^2 \rangle^{1/2}$ for the unequal mass case. To obtain the analytical value for this observable we can use Eq. (2.44). For the 1S1P state we have $\langle r_3^2 \rangle^{1/2} = 1.334\mathrm{GeV}^{-1}$ and for the 1P1D state $\langle r_3^2 \rangle^{1/2} = 1.722\mathrm{GeV}^{-1}$. These values have been marked on Fig. 5.9. We find that our code predicts the correct value of the observable.

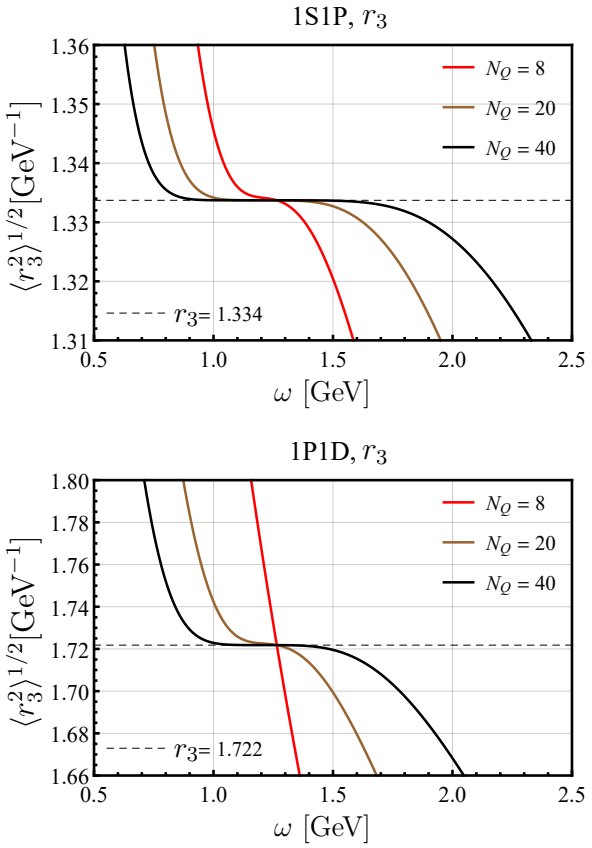

Figure 5.9: Plots of expectation values of the rms distance between the 12 pair of particles for the 1S1P and 1P1D states. Dashed horizontal line marks the analytical value.

5.3.4 Wave Function at the Origin

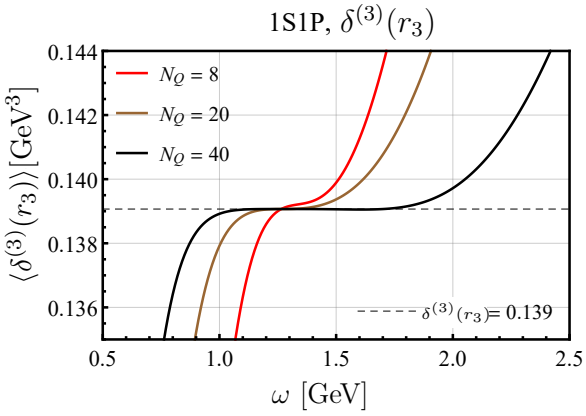

Figure 5.10: Expectation values of the delta function of states 1S1P as function of ω.

In this subsection, we will show that we can use our numerical approach for obtaining the expectation value of the wave function at the origin for particles 1 and 2, defined as $\langle\delta^{(3)}(r_3)\rangle$, for the unequal mass case. We will be comparing the prediction of our numerical method to the analytical value obtained using Eq. (2.56). For the 1S1P state $\langle\delta^{(3)}(r_3)\rangle = 0.139\text{GeV}^3$. We find that our method is able to correctly identify the value of the wave function at the origin as demonstrated in Fig. (2.56).

5.4 Virial Theorem Test

In this last section, we will show that our numerical method satisfies the virial theorem. Virial theorem states that for a system of particles in a simple harmonic potential the expectation value of the kinetic energy $\langle T\rangle$ should be equal to the expectation value of the potential energy $\langle V\rangle$,

$$\langle T\rangle = \langle V\rangle. \tag{5.14}$$

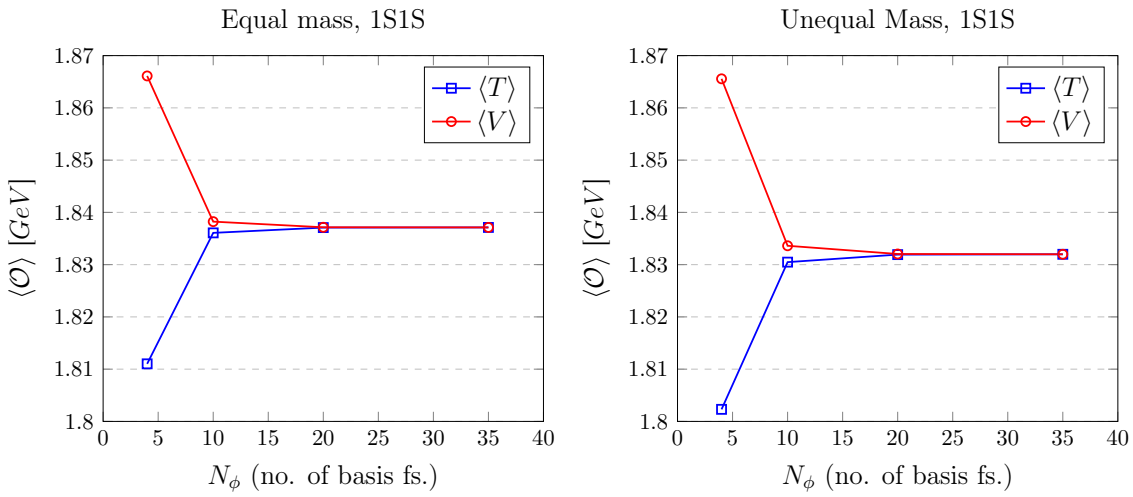

Figure 5.11: Plots of $\langle T \rangle$ and $\langle V \rangle$ for the 1S1S state for both the equal and unequal mass cases.

We will use our numerical method to obtain the expectation values of the kinetic and the potential energy and check if they are equal. From Eq. (5.10) we have

$$\begin{aligned} T &= \sum_{i=1}^{3} m_i + \omega(2n + l + \tfrac{3}{2}) - \tfrac{1}{2}\mu_r \omega^2 r_3^2 + \omega(2N + L + \tfrac{3}{2}) - \tfrac{1}{2}\mu_{\mathrm{R}} \omega^2 R_3^2, \\ V &= \frac{1}{2}\Big(\mu_3 \omega_3^2 r_3^2 + \mu_1 \omega_1^2 r_1^2 + \mu_2 \omega_2^2 r_2^2\Big). \end{aligned} \tag{5.15}$$

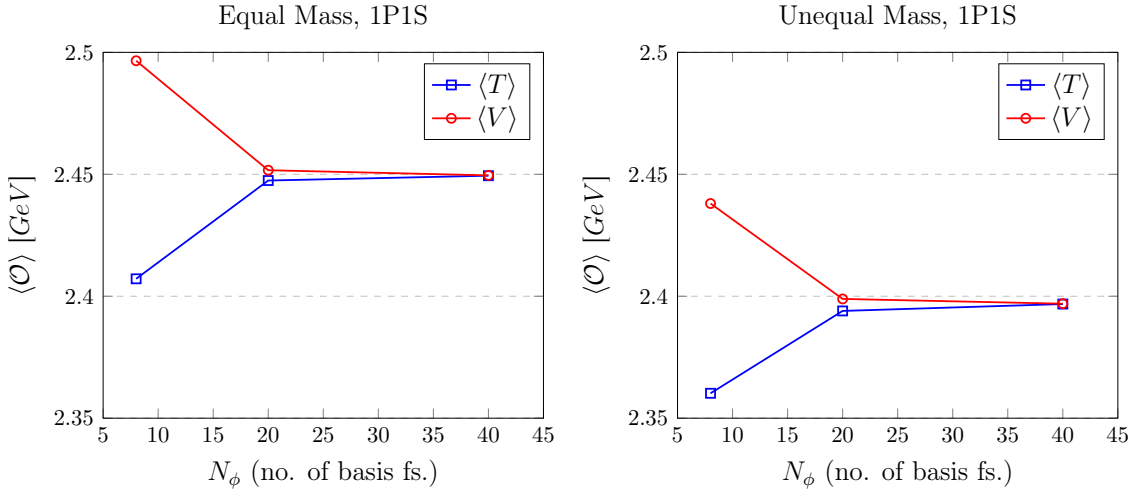

Figure 5.12: Plots of $\langle T \rangle$ and $\langle V \rangle$ for the 1P1S state for both the equal and unequal mass cases.

In Fig. 5.11, we plot the expectation values $\langle T \rangle$ and $\langle V \rangle$ for the 1S1S state for the equal mass case (left) and unequal mass case (right) as a function of the number of basis functions N_ϕ. We plot the same quantities for the 1P1S state in Fig. 5.12 and find that the virial theorem is satisfied for both states when sufficient number of basis functions are used for the calculations. For the equal mass case we have used model parameters specified in Tab. 5.1 and for the unequal mass case, we have used the parameters specified in Tab. 5.2.

This concludes the chapter, we have tested our numerical method against analytical results for the three-body SHO system and found that our method of solving three-body systems using Talmi-Moshinsky transformations is able to reproduce the analytical results to a high degree of accuracy. We have tested the model for an equal mass case where all particles had the same mass and for an unequal mass case where all particles had different masses. Our code was able to perform well in all cases and is able to correctly predict the expectation values of various observables such as the r.m.s. radius or the value of the wave function at the origin.

6

Baryon Spin-Space Basis Sets

Before we embark on solving baryon potential models, we will address the added complication in constructing the spin-space basis sets for a baryon system, which arises due to the Pauli exclusion principle.

In Ref. [1], Silvestre et al. described dealing with systems containing three identical quarks as "painful", due to the Pauli exclusion principle being imposed on all pairs of identical quarks. This requires the construction of symmetrised basis sets. While the task is relatively straightforward in cases with zero or two identical quarks, it becomes more complex in the case of three identical quarks where, the symmetrised spin-space basis functions will in general be given as linear combinations of coupled SHO wavefunctions.

In this chapter, we will describe our method for constructing the symmetrised spin-space basis, which will heavily rely on a previously developed framework for transforming SHO basis wavefunctions, described in Ch. 4. We will extend the concepts developed in that chapter to include the spin degrees of freedom. Generating the symmetrised spin-space basis sets will then come at very little extra cost as it will rely on techniques we are already familiar with.

6.1 Introduction to Spin-Space Basis Functions

The total baryon wavefunction will be described as the product of the colour, flavour, spin and space wavefunctions. When a baryon state contains pairs of identical quarks, in order to satisfy the Pauli exclusion principle, we must ensure that the total wavefunction will explicitly be made antisymmetric under the interchange of the identical pairs. Since the colour wavefunction is always *totally antisymmetric*, we will only need to ensure that the flavour-spin-space part of the wavefunction is made *symmetric* under the interchange of the identical pairs of quarks. For an (anti)symmetric flavour wavefunction we need to construct an (anti)symmetric spin-space wavefunction. We note that the only role of the flavour wavefunction, in this work, will be to fix the symmetry of the spin-space basis.

To construct the appropriately symmetrised spin-space basis for each type of baryon, we introduce the following different types of eigenstates which we will encounter in this chapter,

$$|\psi_n\rangle = |\psi_1\rangle, |\psi_2\rangle, \ldots, \tag{6.1}$$

$$|\varphi_a\rangle = |\varphi_1\rangle, |\varphi_2\rangle, \ldots, \tag{6.2}$$

$$|\phi_i\rangle = |\phi_1\rangle, |\phi_2\rangle, \ldots, \tag{6.3}$$

where n, a and i are generic labels representing all the quantum numbers describing that state. The wavefunctions $|\psi_n\rangle$ represent the total spin-space wavefunctions corresponding to a particular baryon state, they are defined as the eigenstates of the Hamiltonian

$$H|\psi_n\rangle = E_n|\psi_n\rangle. \tag{6.4}$$

The eigenstates $|\psi_n\rangle$ will be expanded on the *symmetrised* spin-space basis denoted as $|\varphi_a\rangle$ which will be specially crafted to obey the Pauli exclusion principle for a given

baryon

$$|\psi_n\rangle = \sum_a |\varphi_a\rangle\langle\varphi_a|\psi_n\rangle. \tag{6.5}$$

The expansion coefficients $\langle\varphi_a|\psi_n\rangle$ are obtained by diagonalising the Hamiltonian in the $|\varphi_a\rangle$ basis denoted as H_φ. The symmetrised basis functions $|\varphi_a\rangle$ are in turn constructed out of the spin-space basis functions $|\phi_i\rangle$ which are agnostic to the Pauli exclusion principle

$$|\varphi_a\rangle = \sum_i |\phi_i^{12}\rangle\langle\phi_i^{12}|\varphi_a\rangle, \tag{6.6}$$

most of this chapter will be devoted to constructing the $|\varphi_a\rangle$ wavefunctions out of the $|\phi_i^{12}\rangle$ spin-space basis functions. i.e. determining the expansion coefficients $\langle\phi_i^{12}|\varphi_a\rangle$. Lastly, the spin-space basis functions $|\phi_i^{12}\rangle$ are defined as the Clebsch-Gordan sum of a spatial and a spin basis function with a combined angular momentum $\boldsymbol{J} = \boldsymbol{\Lambda} + \boldsymbol{S}$, expressed in the 12 basis

$$|\phi_i^{12}\rangle = \sum_{M_\Lambda M_S} \langle JM_J|\Lambda M_\Lambda S M_S\rangle\langle\boldsymbol{\rho},\boldsymbol{\lambda}|nlNL:\Lambda M_\Lambda\rangle|S_{12}SM_S\rangle, \tag{6.7}$$

where, $\boldsymbol{\Lambda} = \boldsymbol{l} + \boldsymbol{L}$ is the states total orbital angular momentum and $\boldsymbol{S} = \boldsymbol{S}_{12} + \boldsymbol{S}_3$ is its total spin. Therefore, we have a hierarchical structure of eigenstates where, the total spin-space wavefunction $|\psi_n\rangle$ is constructed out of symmetrised basis functions $|\varphi_a\rangle$ which are in turn constructed out of the $|\phi_i^{12}\rangle$ basis functions.

6.2 Generalised Transformation Matrices

Similarly as in Sec. 4.4, we will define here the relation between the spin-space basis functions in the 12 basis, denoted as $|\phi_i^{12}\rangle$, and the spin-space basis functions in the two remaining basis $|\phi_i^{23}\rangle$ and $|\phi_i^{31}\rangle$. In Sec. 4.4, we have described such transformations only for the spatial basis functions, using the matrices t_i defined in Eqs. (4.32) and (4.33) In this section, we will obtain the analogue of these, which will now also

include the spin degrees of freedom.

The transformation of the spin-space basis functions from the 12 to the 23 coordinate basis can be expressed as

$$|\phi_i^{12}\rangle = \sum_j |\phi_j^{23}\rangle\langle\phi_j^{23}|\phi_i^{12}\rangle. \tag{6.8}$$

Then the generalised transformation matrix will be defined as

$$T_1 = \begin{pmatrix} \langle\phi_1^{23}|\phi_1^{12}\rangle & \langle\phi_1^{23}|\phi_2^{12}\rangle & \dots \\ \langle\phi_2^{23}|\phi_1^{12}\rangle & \langle\phi_2^{23}|\phi_2^{12}\rangle & \dots \\ \vdots & \vdots & \end{pmatrix}, \tag{6.9}$$

which is a matrix of expansion coefficients defined in Eq. (6.8). We will now show how we can obtain the elements of the T_1 matrix. To do this let us write out $|\phi_i^{12}\rangle$ in full. Since $|\phi_i^{12}\rangle$ is a combination of the spatial and spin basis functions it is described by the following quantum numbers

$$|\phi_i^{12}\rangle = |nlNL:\Lambda\rangle|S_{12}S\rangle, \tag{6.10}$$

where we have separated out the spatial and spin wavefunctions. In a similar fashion, the spin-space basis function in the 23 basis is given as

$$|\phi_i^{23}\rangle = |n_1l_1N_1L_1:\Lambda\rangle|S_{23}S\rangle, \tag{6.11}$$

The expansion in Eq. (6.8), can now be written as

$$|nlNL:\Lambda\rangle|S_{12}S\rangle = \sum_{\substack{n_1,l_1N_1L_1 \\ S_{23}}} |n_1l_1N_1L_1:\Lambda\rangle|S_{23}S\rangle\langle n_1l_1N_1L_1:\Lambda|nlNL:\Lambda\rangle\langle S_{23}S|S_{12}S\rangle, \tag{6.12}$$

where $\langle n_1l_1N_1L_1:\Lambda|nlNL:\Lambda\rangle$ are the familiar Talmi coefficients and $\langle S_{23}S|S_{12}S\rangle$

are the expansion coefficients related to the basis transformation of the spin wave-functions. The necessary expansion coefficients for the transformations of spin basis functions are given as

$$|S_{12}, S\rangle \equiv |0, \tfrac{1}{2}\rangle_{12} = -\tfrac{1}{2}|0, \tfrac{1}{2}\rangle_{23} - \tfrac{\sqrt{3}}{2}|1, \tfrac{1}{2}\rangle_{23}, \tag{6.13}$$

$$|1, \tfrac{3}{2}\rangle_{12} = |1, \tfrac{3}{2}\rangle_{23}, \tag{6.14}$$

Similarly for the 12 to 31 basis transformation, we have

$$|0, \tfrac{1}{2}\rangle_{12} = -\tfrac{1}{2}|0, \tfrac{1}{2}\rangle_{31} + \tfrac{\sqrt{3}}{2}|1, \tfrac{1}{2}\rangle_{31}, \tag{6.15}$$

$$|1, \tfrac{3}{2}\rangle_{12} = |1, \tfrac{3}{2}\rangle_{31}. \tag{6.16}$$

The factors of $-\frac{1}{2}$ and $\pm\frac{\sqrt{3}}{2}$ (expansion coefficients) can be looked up in Ref. [67] and involve the use of $6-j$ symbols. The elements of the T_1 matrix are thus products of Talmi coefficients and the appropriate spin transformation coefficients found in Eqs. (6.13) through to (6.16). The same steps can be followed to obtain the generalised transformation matrix T_2 which is defined as

$$T_2 = \begin{pmatrix} \langle \phi_1^{31} | \phi_1^{12} \rangle & \langle \phi_1^{31} | \phi_2^{12} \rangle & \dots \\ \langle \phi_2^{31} | \phi_1^{12} \rangle & \langle \phi_2^{31} | \phi_2^{12} \rangle & \dots \\ \vdots & \vdots & \end{pmatrix}, \tag{6.17}$$

which is responsible for the 12 to 31 transformation of the spin-space basis functions. We can use the generalised transformation matrices to obtain matrix representations of operators expressed in the 23 and 31 coordinate basis using the same prescription as in Eq. (4.38), i.e.

$$\mathcal{O}_{ij} = T_k^T \mathcal{O}_{12}(\alpha_k) T_k, \tag{6.18}$$

with $ij = 23$ or 31, and O_{ij} is a general operator matrix represented in the $|\phi_i^{12}\rangle$ basis. For example, if we wanted to obtain the matrix representation of the operator $\boldsymbol{S}_2 \cdot \boldsymbol{S}_3$ in the $|\phi_i^{12}\rangle$ basis. Which is an operator that appears in the spin-spin interaction term

between quarks 2 and 3, we can use the T_1 matrix, to get

$$\begin{pmatrix} \langle\phi_1^{12}|\boldsymbol{S}_2\cdot\boldsymbol{S}_3|\phi_1^{12}\rangle & \langle\phi_1^{12}|\boldsymbol{S}_2\cdot\boldsymbol{S}_3|\phi_2^{12}\rangle & \dots \\ \langle\phi_2^{12}|\boldsymbol{S}_2\cdot\boldsymbol{S}_3|\phi_1^{12}\rangle & \langle\phi_2^{12}|\boldsymbol{S}_2\cdot\boldsymbol{S}_3|\phi_2^{12}\rangle & \dots \\ \vdots & \vdots & \end{pmatrix} = T_1^{\mathrm{T}} \begin{pmatrix} \langle\phi_1^{12}|\boldsymbol{S}_1\cdot\boldsymbol{S}_2|\phi_1^{12}\rangle & \langle\phi_1^{12}|\boldsymbol{S}_1\cdot\boldsymbol{S}_2|\phi_2^{12}\rangle & \dots \\ \langle\phi_2^{12}|\boldsymbol{S}_1\cdot\boldsymbol{S}_2|\phi_1^{12}\rangle & \langle\phi_2^{12}|\boldsymbol{S}_1\cdot\boldsymbol{S}_2|\phi_2^{12}\rangle & \dots \\ \vdots & \vdots & \end{pmatrix} T_1. \quad (6.19)$$

Another similar example is the ρ_2 operator, which appears in the linear part of the Cornell potential for the 31 pair of quarks. To obtain its matrix representation in the $|\phi_i^{12}\rangle$ basis we can perform the same trick; obtain the representation of the ρ operator in the 12 basis and use the generalised transformation matrices to get,

$$\begin{pmatrix} \langle\phi_1^{12}|\rho_2|\phi_1^{12}\rangle & \langle\phi_1^{12}|\rho_2|\phi_2^{12}\rangle & \dots \\ \langle\phi_2^{12}|\rho_2|\phi_1^{12}\rangle & \langle\phi_2^{12}|\rho_2|\phi_2^{12}\rangle & \dots \\ \vdots & \vdots & \end{pmatrix} = T_2^{\mathrm{T}} \begin{pmatrix} \langle\phi_1^{12}|\rho|\phi_1^{12}\rangle & \langle\phi_1^{12}|\rho|\phi_2^{12}\rangle & \dots \\ \langle\phi_2^{12}|\rho|\phi_1^{12}\rangle & \langle\phi_2^{12}|\rho|\phi_2^{12}\rangle & \dots \\ \vdots & \vdots & \end{pmatrix} T_2. \quad (6.20)$$

6.3 Components of the Total wavefunction

In this section, we will describe what determines the symmetries of the colour, flavour, spin and space components of the total baryon wavefunction. Each of these components can be symmetric or antisymmetric, or neither in the case of the flavour wavefunction, under the interchange of pairs of quarks. In order to understand how to construct symmetrised basis sets, let us look into what determines the symmetry of each component of the total wavefunction.

6.3.1 Colour

The colour wavefunction is always totally antisymmetric under the interchange of any pair of quarks.

6.3.2 Flavour

In the case where all quarks are different, the flavour wavefunction will neither be symmetric nor antisymmetric under the exchange of any pair of quarks.

For the case of two equal quarks, if the identical quarks are the heavy ss, cc or bb pairs then the flavour wavefunction will only be symmetric under the interchange of those quarks.

However, if the two identical quarks are the up and the down quark, the flavour wavefunction can be either symmetric or antisymmetric. This is because we assume an SU(2) (u, d) flavour symmetry, due to their masses being approximately equal. This gives rise to an Isospin doublet. The up and down quarks can combine to form either a singlet or a triplet state, with the triplet being a symmetric state and the singlet being antisymmetric. In flavour SU(2), the baryon multiplets that arise are

$$\left.\begin{aligned} |I, I_z\rangle = |0,0\rangle = \frac{1}{\sqrt{2}}(ud - du) \end{aligned}\right\} \text{ antisymmetric isospin 0 singlet,} \tag{6.21}$$

$$\left.\begin{aligned} |1,1\rangle &= uu \\ |1,0\rangle &= \frac{1}{\sqrt{2}}(ud + du) \\ |1,-1\rangle &= dd \end{aligned}\right\} \text{ symmetric isospin 1 triplet.} \tag{6.22}$$

In our work, the models that we use, assume the triplet states to be degenerate, resulting in only two separate states originating from the SU(2) approximate symmetry.

Those two separate states will be referred to as $\Lambda_q(udq)$ and $\Sigma_q(uuq)$ with q being either the charm or the bottom quark, in our work.

Lastly, in the case of all equal quarks, where we will only be looking at ccc and bbb combinations, the flavour wavefunction will be totally symmetric under the interchange of any pair of identical quarks. See Tab. 6.1 for a summary.

Baryon	12	23	31	I
All quarks different	–	–	–	–
(qq)q′ (q = s, c or b)	S	–	–	–
Λ_q(udq) (q = c or b)	A	–	–	0
Σ_q(uuq) (q = c or b)	S	–	–	1
(qqq) (q = c or b)	S	S	S	–

Table 6.1: Symmetry of the flavour wave function under the interchange of each quark pair for different quark configurations, I = Isospin, q′ represents a quark different from q, A=Antisymmetric, S=Symmetric and the symbol '–' means not applicable.

6.3.3 Spin

The spin wavefunction which we denote as $|S_{ij}S\rangle$, can be symmetric or antisymmetric under the interchange of quarks i and j depending on the quantum number $\boldsymbol{S}_{ij} = \boldsymbol{S}_i + \boldsymbol{S}_j$. Each quark possesses spin $S_i = \frac{1}{2}$, two quarks can combine to produce an antisymmetric singlet state with spin $S_{ij} = 0$ or a symmetric triplet state with spin

$S_{ij} = 1$, i.e. $\mathbf{\frac{1}{2}} \otimes \mathbf{\frac{1}{2}} = \mathbf{0} \oplus \mathbf{1}$, or in more detail,

$$\left.\begin{aligned} |S_{ij}, M_s^{ij}\rangle = |0,0\rangle = \frac{1}{\sqrt{2}}(\uparrow\downarrow - \downarrow\uparrow) \end{aligned}\right\} \text{ antisymmetric spin 0 singlet,} \tag{6.23}$$

$$\left.\begin{aligned} |1,1\rangle &= \uparrow\uparrow \\ |1,0\rangle &= \frac{1}{\sqrt{2}}(\uparrow\downarrow + \downarrow\uparrow) \\ |1,-1\rangle &= \downarrow\downarrow \end{aligned}\right\} \text{ symmetric spin 1 triplet.} \tag{6.24}$$

where M_s^{ij} is the projection of S_{ij}, the up and down arrows represent a spin up or spin down quark, respectively. Therefore, the symmetry of the spin wavefunction is determined by the quantum number S_{ij}, if it is 0 it means it is antisymmetric and if 1, it is symmetric under the interchange of quarks i and j. Similarly, as in flavour, we treat the triplet spin states as degenerate, as the models that we work with are not sensitive to the projections of spin.

6.3.4 Space

The spatial basis functions are constructed from coupled SHO wavefunctions. A coupled SHO basis function in the 12 basis is given as a Clebsch-Gordan sum of a product of SHO wavefunctions

$$\langle \boldsymbol{\rho}, \boldsymbol{\lambda} | nl, NL : \Lambda\mathcal{M}\rangle = \sum_{mM} \langle lmLM|\Lambda\mathcal{M}\rangle \langle \boldsymbol{\rho}|nlm\rangle \langle \boldsymbol{\lambda}|NLM\rangle, \tag{6.25}$$

There also exist spatial basis sets defined for the 23 and 31 coordinate basis

$$\langle \boldsymbol{\rho_1}, \boldsymbol{\lambda_1} | n_1 l_1, N_1 L_1 : \Lambda\mathcal{M}\rangle = \sum_{m_1 M_1} \langle l_1 m_1 L_1 M_1|\Lambda\mathcal{M}\rangle \langle \boldsymbol{\rho_1}|n_1 l_1 m_1\rangle \langle \boldsymbol{\lambda_1}|N_1 L_1 M_1\rangle, \tag{6.26}$$

$$\langle \boldsymbol{\rho_2}, \boldsymbol{\lambda_2} | n_2 l_2, N_2 L_2 : \Lambda\mathcal{M}\rangle = \sum_{m_2 M_2} \langle l_2 m_2 L_2 M_2|\Lambda\mathcal{M}\rangle \langle \boldsymbol{\rho_2}|n_2 l_2 m_2\rangle \langle \boldsymbol{\lambda_2}|N_2 L_2 M_2\rangle. \tag{6.27}$$

The symmetry of the spatial basis function in Eq. (6.25) under the interchange of quarks 1 and 2 is determined by the orbital angular momentum coupled to the $\boldsymbol{\rho}$ coordinate, namely the quantum number l. The spatial wavefunction is symmetric/antisymmetric under the interchange of particles 1 and 2 when l is even/odd, we have illustrated this in Fig. 2.3.

If only quarks 1 and 2 are identical, then the symmetry constraint is only imposed on the spatial basis functions in the 12 basis, constraining the value of l. However, if all quarks are identical, then this also limits the other two spatial basis defined for the 23 and 31 coordinate basis shown in Eqs. (6.26) and (6.27). When all quarks are identical this constraints not only l but also the quantum numbers l_1 and l_2. Therefore, the more identical quarks there are in our system, the more restricted our pool of spatial basis functions will become.

6.4 The Three Separate Cases

In this section, we will discuss how we will construct the symmetrised basis $|\varphi_a\rangle$ for baryons containing zero, two and three identical quarks. The $|\varphi_a\rangle$ sets will be dependent on the symmetry of the flavour wavefunction and the number of identical quarks present in the system.

We note that the method we are using for dealing with equal quarks has mainly been developed with the three-equal-quarks case in mind. Nevertheless, for consistency we will use the same method for obtaining the appropriately symmetrised spin-space basis sets $|\varphi_a\rangle$ for the two remaining cases (zero and two identical quarks).

6.4.1 General Method

What we are mainly interested in is obtaining the symmetrised Hamiltonian matrix H_φ defined as

$$H_\varphi = \begin{pmatrix} \langle\varphi_1|H|\varphi_1\rangle & \langle\varphi_1|H|\varphi_2\rangle & \dots \\ \langle\varphi_2|H|\varphi_1\rangle & \langle\varphi_2|H|\varphi_2\rangle & \dots \\ \vdots & \vdots & \end{pmatrix}, \tag{6.28}$$

which is ensured to obey the Pauli exclusion principle. The general approach for obtaining H_φ will start with building the Hamiltonian H_ϕ

$$H_\phi = \begin{pmatrix} \langle\phi_1|H|\phi_1\rangle & \langle\phi_1|H|\phi_2\rangle & \dots \\ \langle\phi_2|H|\phi_1\rangle & \langle\phi_2|H|\phi_2\rangle & \dots \\ \vdots & \vdots & \end{pmatrix}, \tag{6.29}$$

we note that H_ϕ breaks up into diagonal blocks with equal J, P, Λ and S quantum numbers, where $P = (-1)^{l+L}$ is the parity of a state. Thus, we will preemptively only construct single blocks of H_ϕ and when generating a set of $|\phi_i\rangle$ basis functions we will ensure that the set only contains states with equal J, P, Λ and S quantum numbers. Note that Λ and S are good quantum numbers, only because the considered Hamiltonians do not include the spin-orbit or tensor terms, but only the spin-spin term. Had we also included those terms, H_ϕ would break up into blocks of equal J and P quantum numbers but not necessarily equal Λ and S.

Let us present here an example of a spin-space basis set $\{|\phi_i\rangle\}$ which we will generate using our code with the following quantum numbers $J^P = \frac{1}{2}^+$, $\Lambda = 0$ and $S = \frac{1}{2}$ with $\gamma \leq 2$, where $\gamma = 2(n+N)+l+L$. For this combination of inputs, the code generates

all the states satisfying those conditions,

$$\{|\phi_i\rangle\} = \begin{bmatrix} n & l & N & L & \Lambda & S_{12} & S \\ 0 & 0 & 0 & 0 & 0 & 0 & 1/2 \\ 0 & 0 & 0 & 0 & 0 & 1 & 1/2 \\ 0 & 0 & 1 & 0 & 0 & 0 & 1/2 \\ 0 & 0 & 1 & 0 & 0 & 1 & 1/2 \\ 0 & 1 & 0 & 1 & 0 & 0 & 1/2 \\ 0 & 1 & 0 & 1 & 0 & 1 & 1/2 \\ 1 & 0 & 0 & 0 & 0 & 0 & 1/2 \\ 1 & 0 & 0 & 0 & 0 & 1 & 1/2 \end{bmatrix}. \tag{6.30}$$

There are 8 space-spin basis functions $|\phi_i\rangle$ in total satisfying the chosen quantum numbers. We could generate a larger set of spin-space basis functions for a better approximation by increasing the threshold γ which limits the number of spin-space basis functions. However, for this demonstration it will suffice to use $\gamma \leq 2$. You can check that all states in (6.30) satisfy the selected quantum numbers.

The relation between H_φ and H_ϕ can be obtained by using the expansion in Eq. (6.6), the element of H_φ then can be expressed as

$$\langle\varphi_{a'}|H|\varphi_a\rangle = \sum_{ii'}\langle\varphi_{a'}|\phi_{i'}\rangle\langle\phi_{i'}|H|\phi_i\rangle\langle\phi_i|\varphi_a\rangle = \varphi^\dagger_{a'} H_\phi \varphi_a, \tag{6.31}$$

with

$$\varphi_a \equiv \begin{pmatrix} \langle\phi_1|\varphi_a\rangle \\ \langle\phi_2|\varphi_a\rangle \\ \vdots \end{pmatrix}. \tag{6.32}$$

We can substitute (6.31) into (6.28) to obtain

$$H_\varphi = \begin{pmatrix} \varphi_1^\dagger H_\phi \varphi_1 & \varphi_1^\dagger H_\phi \varphi_2 & \dots \\ \varphi_2^\dagger H_\phi \varphi_1 & \varphi_2^\dagger H_\phi \varphi_2 & \dots \\ \vdots & \vdots & \end{pmatrix} = \begin{pmatrix} \varphi_1^\dagger \\ \varphi_2^\dagger \\ \vdots \end{pmatrix} H_\phi \begin{pmatrix} \varphi_1 & \varphi_2 & \dots \end{pmatrix} = \varphi^\dagger H_\phi \varphi, \tag{6.33}$$

where

$$\varphi \equiv \begin{pmatrix} \varphi_1 & \varphi_2 & \dots \end{pmatrix} \equiv \begin{pmatrix} \langle \phi_1 | \varphi_1 \rangle & \langle \phi_1 | \varphi_2 \rangle & \dots \\ \langle \phi_2 | \varphi_1 \rangle & \langle \phi_2 | \varphi_2 \rangle & \dots \\ \vdots & \vdots & \end{pmatrix}, \tag{6.34}$$

i.e. φ is the matrix of expansion coefficients defined previously in Eq. (6.6). In fact, Eq. (6.33) can be generalised to any operator $\mathcal{O}$ as

$$\mathcal{O}_\varphi = \varphi^\dagger \mathcal{O}_\phi \varphi, \tag{6.35}$$

where any operator in the $|\phi_i\rangle$ basis can be transformed into an operator in the symmetrised $|\varphi_a\rangle$ basis by using the φ transformation matrices.

We note that the spin-space basis expansions are supposed to be over infinite sets but of course we truncate the expansion to deal with finite sums. After truncating the number N_ϕ of states in the $|\phi_i\rangle$ basis, the number of states in the $|\varphi_a\rangle$ basis is $N_\varphi \leq N_\phi$. Thus φ as defined in Eq. (6.34) will not in general be a square matrix. To summarise, the pipeline for obtaining H_φ in all cases is shown in Fig. (6.1).

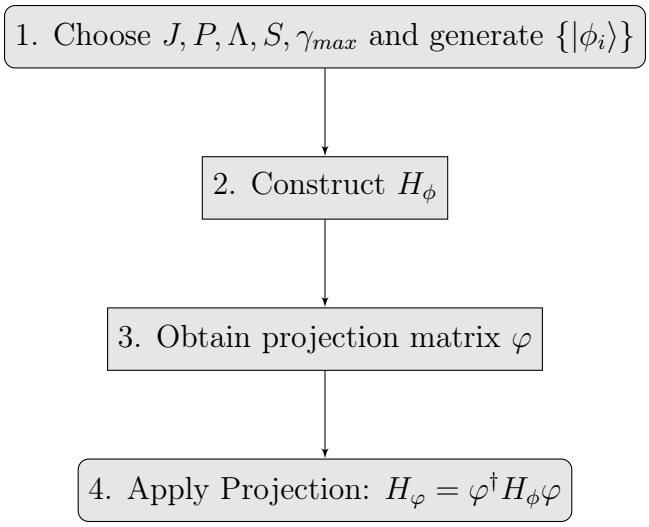

Figure 6.1: A simplified procedure flowchart for obtaining H_φ using our code.

The missing link that remains, is obtaining the matrix φ which will take us from H_ϕ to H_φ. To give a feel for what one might expect, in the case with no equal quarks, the φ matrix will just be an identity matrix as no additional symmetry constraints need to be imposed on the $|\phi_i\rangle$ basis. We will show how to obtain φ for each separate case in the following sections.

6.4.2 No Identical Quarks

Starting with the trivial case where all quarks are different, which is true for e.g. the Ξ_c(usc) baryon, composed of three different quarks; up, strange and charm. The flavour wavefunction of this state is neither symmetric nor antisymmetric under the interchange of any pair of quarks, meaning there are no restrictions on the symmetry of the spin-space basis wavefunctions. In this case, we have $\langle\phi_i|\varphi_a\rangle = \delta_{ia}$, meaning that the φ matrix is just the identity matrix. And H_ϕ is equal to H_φ.

6.4.3 Two Identical Quarks

Because the spatial basis functions are defined in the 12 coordinate basis, when dealing with baryon states containing two identical quarks, it will be most convenient to label the two identical quarks as quarks 1 and 2.

As an example, we will use the Ω_c(ssc) baryon state whose flavour wave function is symmetric under the interchange of flavour labels of quarks 1 and 2 (the ss pair). As such, we must ensure that the spin-space basis functions are also symmetric under the interchange of the spin and space labels of quarks 1 and 2.

To impose the symmetry constraints on the $|\phi_i\rangle$ basis, we will define the permutation operator P_{12} which interchanges the spin and spatial labels of quarks 1 and 2. The operator is defined as

$$P_{12}|\phi_i\rangle = (-1)^{S_{12}+l+1}|\phi_i\rangle, \tag{6.36}$$

where $|\phi_i\rangle$ are eigenstates of the P_{12} operator. Note that the symmetry of the spin-space wavefunctions under the interchange of particles 1 and 2 is dependant on the quantum numbers S_{12} and l, see sections 6.3.3 and 6.3.4 for more details.

In the example set of spin-space basis functions in Eq. (6.30) we see that the first state from the top is antisymmetric ($P_{12} = -1$) under the interchange of quarks 1 and 2, the second one is symmetric ($P_{12} = +1$) etc. Note that we could at this point manually pick out the symmetric spin-space states and use them to construct H_φ. However, the same approach would not be possible in the case with three equal quarks, thus for completeness, we will use a more general method for obtaining H_φ which involves obtaining the φ matrix. This will allow us to extend this approach naturally to the three-identical-quark case.

In general, to extract the eigenstates $|\phi_i\rangle$ with eigenvalues $P_{12} = \pm 1$, we will define

operators $Q_{12}^{\pm}$ which we will use to obtain states $|\varphi_a\rangle$

$$Q_{12}^{\pm} = \frac{1}{2}(P_{12} \pm 1). \tag{6.37}$$

If we have a set of space-spin basis functions $|\phi_i\rangle$ which are a mixture of $P_{12} = \pm 1$ states, we can use $Q_{12}^{\pm}$ to project out only the $P_{12} = \pm 1$ states. Since in our example the flavour wavefunction is symmetric, we will be using the Q_{12}^{+} operator. First, we will obtain its matrix representation in the $|\phi_i\rangle$ basis

$$Q_{12}^{+} = \begin{pmatrix} \langle\phi_1|Q_{12}^{+}|\phi_1\rangle & \langle\phi_1|Q_{12}^{+}|\phi_2\rangle & \dots \\ \langle\phi_2|Q_{12}^{+}|\phi_1\rangle & \langle\phi_2|Q_{12}^{+}|\phi_2\rangle & \dots \\ \vdots & \vdots & \end{pmatrix}. \tag{6.38}$$

As the operator Q_{12}^{+} does not mix $|\phi_i\rangle$ states, it will be a matrix with 1s or 0s on the diagonal and 0s everywhere else. We can use our code to generate the Q_{12}^{+} matrix which for the particular set of spin-space basis functions given in (6.30) gives

$$Q_{12}^{+} = \begin{pmatrix} 0 & 0 & 0 & 0 & 0 & 0 & 0 & 0 \\ 0 & 1 & 0 & 0 & 0 & 0 & 0 & 0 \\ 0 & 0 & 0 & 0 & 0 & 0 & 0 & 0 \\ 0 & 0 & 0 & 1 & 0 & 0 & 0 & 0 \\ 0 & 0 & 0 & 0 & 1 & 0 & 0 & 0 \\ 0 & 0 & 0 & 0 & 0 & 0 & 0 & 0 \\ 0 & 0 & 0 & 0 & 0 & 0 & 0 & 0 \\ 0 & 0 & 0 & 0 & 0 & 0 & 0 & 1 \end{pmatrix}. \tag{6.39}$$

Comparing (6.39) and (6.30) we can see that Q_{12}^{+} only projects out the symmetric basis functions. The 1s represent the states we want to keep and 0s the states to reject i.e. states which violate the Pauli exclusion principle. From (6.39) we see that there is a total of 4 symmetric spin-space basis states in the list of states in Eq. (6.30) and they are in positions 2, 4, 5 and 8.

Next, we will discuss how we can use the Q_{12}^{+} matrix to obtain φ defined previously in Eq. (6.34). Since $|\phi_i\rangle$ are eigenstates of Q_{12}^{+}, we can extract all the eigenvectors of Q_{12}^{+} matrix with the eigenvalue equal to 1. Those eigenstates will be exactly the

eigenstates that we want for our calculations:

$$Q_{12}^{+}|\phi_i\rangle = \lambda_i|\phi_i\rangle. \tag{6.40}$$

The φ matrix can then be composed out of the eigenvectors of the Q_{12}^{+} operator with $\lambda_i = 1$. In this example, there are four such eigenstates, We can use our code to generate φ, giving us

$$\varphi = \begin{pmatrix} \varphi_1 & \varphi_2 & \varphi_3 & \varphi_4 \end{pmatrix} = \begin{pmatrix} 0 & 0 & 0 & 0 \\ 0 & 0 & 0 & 1 \\ 0 & 0 & 0 & 0 \\ 0 & 0 & 1 & 0 \\ 0 & 1 & 0 & 0 \\ 0 & 0 & 0 & 0 \\ 0 & 0 & 0 & 0 \\ 1 & 0 & 0 & 0 \end{pmatrix}. \tag{6.41}$$

We can now use the generated φ matrix to produce the Hamiltonian $H_\varphi = \varphi^\dagger H_\phi \varphi$ which will be a 4×4 matrix. In summary, we went from an 8×8 Hamiltonian H_ϕ to an appropriately symmetrised 4×4 Hamiltonian H_φ. The Pauli exclusion principle has limited the number of spin-space basis functions that we are allowed to use.

Note that in the case of the Λ_c(udc) baryon whose flavour wavefunction is *antisymmetric* under the interchange of quarks 1 and 2, the spin-space basis functions must be antisymmetric. In which case we would use the Q_{12}^{-} operator and the matrix φ would be composed out of the eigenvectors of Q_{12}^{-} matrix with the eigenvalues $\lambda_i = 1$.

In conclusion, for two identical quarks, The symmetrised set $|\varphi_a\rangle$ is simply a a subset of the $|\phi_i\rangle$ set. The case with three identical quark will be more complicated because making the wavefunctions symmetric under the interchange of quarks 1 and 2 does not ensure that the wavefunctions will be symmetric under interchange of the identical pairs 23 and 31. In this case the set $|\varphi_a\rangle$ will no longer simply be a subset of the $|\phi_i\rangle$ basis but will involve linear combinations of $|\phi_i\rangle$ wavefunctions.

6.4.4 Three Identical Quarks

For baryon states with three identical quarks whose flavour wavefunctions will be totally symmetric, we will need the spin-space basis states to also be totally symmetric. Meaning they must be eigenstates of not only the operator P_{12} but also of operators P_{23} and P_{31}. We need spin-space basis states which satisfy

$$P_{12} = P_{23} = P_{31} = 1. \tag{6.42}$$

Note that if we can find a state satisfying

$$P_{12} = P_{23} = 1, \tag{6.43}$$

then $P_{31} = 1$ is automatic. Thus we want to select the eigenstates of the operator $Q_{12}^{+}Q_{23}^{+}$ with eigenvalue $+1$. Note,

$$Q_{12}^{+}Q_{23}^{+} = \tfrac{1}{2}(P_{12}+1)\tfrac{1}{2}(P_{23}+1). \tag{6.44}$$

So we want to construct states $|\varphi_a\rangle$ constrained to satisfy

$$Q_{12}^{+}Q_{23}^{+}|\phi_a\rangle = \lambda_a|\phi_a\rangle, \tag{6.45}$$

with $\lambda_a = 1$. In order to obtain a matrix representation of the $Q_{12}^{+}Q_{23}^{+}$ operator we will need to use the generalised transformation matrices defined previously in Eq. (6.18) to write the operator Q_{23}^{+} as

$$Q_{23}^{+} = T_1^{\mathrm{T}} Q_{12}^{+} T_1, \tag{6.46}$$

$$\therefore Q_{12}^{+}Q_{23}^{+} = Q_{12}^{+} T_1^{\mathrm{T}} Q_{12}^{+} T_1. \tag{6.47}$$

Given that we can obtain the matrices T_1 and with the knowledge that we can obtain the Q_{12}^{+} matrix which we have shown an example of in Eq. (6.39), we can thus obtain

the matrix representation of $Q_{12}^{+}Q_{23}^{+} = Q_{12}T_1^{\mathrm{T}}Q_{12}T_1$. We can use our code to generate this matrix for us which (up to 2 decimal places) returns

$$Q_{12}^{+}T_1^{T}Q_{12}^{+}T_1 = \begin{pmatrix} 0. & 0. & 0. & 0. & 0. & 0. & 0. & 0. \\ -0.43 & 0.25 & 0. & 0. & 0. & 0. & 0. & 0. \\ 0. & 0. & 0. & 0. & 0. & 0. & 0. & 0. \\ 0. & 0. & -0.11 & 0.44 & 0.27 & 0.15 & -0.32 & -0.19 \\ 0. & 0. & -0.15 & 0.27 & 0.63 & -0.22 & 0.15 & -0.27 \\ 0. & 0. & 0. & 0. & 0. & 0. & 0. & 0. \\ 0. & 0. & 0. & 0. & 0. & 0. & 0. & 0. \\ 0. & 0. & -0.32 & -0.19 & -0.27 & -0.15 & -0.11 & 0.44 \end{pmatrix}. \quad (6.48)$$

The above matrix only contains a single eigenvector φ_a with the desired eigenvalue $\lambda_a = 1$. This eigenstate is given as

$$\varphi_a = \begin{pmatrix} 0 \\ 0 \\ 0 \\ 1/2 \\ \sqrt{1/2} \\ 0 \\ 0 \\ -1/2 \end{pmatrix}. \quad (6.49)$$

In the case of three identical quarks, out of the whole set of spin-space basis functions listed in Eq. (6.30), we can only generate a single totally symmetric spin-space basis function. The totally symmetric spin-space basis function is a linear combination of the wavefunctions found in the $\{|\phi_i\rangle\}$ set listed in Eq. (6.30).

The Hamiltonian matrix $H_\varphi = \varphi^\dagger H_\phi \varphi$ is then only a 1×1 matrix, which of course is not enough to obtain a reliable approximation of the spin-space wavefunction for any baryon state. We must therefore consider a much larger set of spin-space basis functions $\{|\phi_i\rangle\}$ by increasing the energy threshold γ. In our calculations we will consider basis sets with at least 100 $|\phi_i\rangle$ spin-space basis functions in order to still have a large enough representation in the $|\varphi_a\rangle$ set.

6.5 Similarities and Differences with Existing Method

In this section, we will discuss the similarities and differences between our method for solving the three-body problem, with a focus on baryons, and the method proposed by Silvestre et al. [1]. Firstly, both our approaches rely on the principles of the variational method which means expanding a trial wavefunction onto a finite subset of the infinite set of SHO basis wavefunctions. In both of our methods the three-body system is parameterised by two Jacobi coordinates, meaning we need to use coupled SHO basis functions, see Eq. (2.21), i.e. two separate sets of SHO basis functions. Also, both our approaches rely on using the Talmi-Moshinsky coefficients for transforming the coupled SHO wavefunctions between different Jacobi frames, necessary for computing complex integrals that would otherwise be mathematically cumbersome to deal with.

One of the achievements of the work presented by Silvestre et al. is the possibility of tuning the size parameters of both sets of SHO basis functions, independently. This gives their method more flexibility which as mentioned in their paper is especially important for asymmetric systems where the masses of the three particles are very different. However, this brings with it an added layer of complexity by having to optimise both size parameters simultaneously, which is a three-dimensional optimisation problem as opposed to a two-dimensional as is the case in our approach. However, when we come to compare our results with literature in Ch. 7 we will find that using a single size parameter for both SHO basis sets did not negatively impact results as we will still be able to accurately reproduce results found in the literature obtained using a different numerical method for solving three-body problems.

Additionally, in the method proposed by Silvestre et al. their calculation of the Talmi-Moshinsky coefficients is tied to the size parameters, meaning that the coefficients need to be recalculated each time any of the size parameters change, which can be costly. In our method, the Talmi-Moshinsky coefficients are only tied to the masses of the particles, meaning that for a given three-body system we only need to

calculate the Talmi-Moshinsky coefficients once and not have to recalculate them in the optimisation part of the calculation.

Furthermore, although Silvestre mentions that the method in their paper could also be applied to systems including spin interactions, they have only shown their work applied to spin-averaged models. In our work we show how the method can be implemented for spin-dependent models such as the one in Ch. 7. This involves not only using spatial basis functions, i.e. the coupled SHO basis functions but also considering the spin basis functions, adding an extra layer of complexity.

The main similarities and differences have been summarised in Tab. 6.2.

Description	Ours	Silvestre et al. [1]
• Uses variational method	✓	✓
• Uses SHO wavefunctions as basis functions	✓	✓
• Uses Moshinsky coefficients	✓	✓
• Number of optimisable size parameters	1	2
• Needs to recalculate Moshinsky coefficients every time size parameters change	✗	✓
• Includes spin	✓	✗

Table 6.2: Similarities and differences between our method for solving the three-body problem using the variational method and Silvestre et al.'s method [1].

7 Three-Body Cornell Potential - Baryons

In this chapter, we will solve a baryon potential model previously solved in Ref. [2]. Our approaches for solving the model numerically are different, however, we are mainly interested in agreement between our results to ensure that the variational method that we have developed specifically for baryons in Ch. 6 works. More specifically, before we move on to solving baryon models at finite temperature we want to ensure that our method for constructing the symmetrised spin-space basis sets outlined in Ch. 6 works as intended.

We will start this chapter by outlining the potential model and then obtain results for some of the observables that were computed in the paper, aiming to reproduce his results.

7.1 Baryon Model

In this section, we will describe the baryon potential, which will be the potential found in Ref. [2]. The model we will be solving is denoted as the AL1 model in the paper.

In Eq. (2.35), we have obtained the Hamiltonian describing a general three-body

system with particles related by pairwise central potentials expressed in dimensionless variables. We will write the Hamiltonian here for our convenience,

$$\begin{aligned} H_{\text{three-body}} = \sum_{i=1}^{3} m_i + \omega_\rho(2n + l + \tfrac{3}{2}) - \tfrac{1}{2}\omega_\rho\rho^2 \\ + \omega_\lambda(2N + L + \tfrac{3}{2}) - \tfrac{1}{2}\omega_\lambda\lambda^2 \\ + V_{12}(\rho_3) + V_{23}(\rho_1) + V_{31}(\rho_2). \end{aligned} \tag{7.1}$$

The pairwise central potential used to describe the quark-antiquark interactions is given in Ref. [2] as

$$V_{ij}^{q\bar{q}}(r_k) = -\frac{\kappa}{r_k} + \sigma r_k - K + \frac{8\kappa'}{3m_i m_j \pi^{1/2} r_0^3} \exp\big(-\tfrac{1}{r_0^2} r_k^2\big) \boldsymbol{S}_i \cdot \boldsymbol{S}_j, \tag{7.2}$$

with

$$r_0(m_i, m_j) = A\Big(\frac{2m_i m_j}{m_i + m_j}\Big)^{-B}. \tag{7.3}$$

However, what we are interested in is the quark-quark interaction which is defined as $V_{ij}^{qq} = \frac{1}{2} V_{ij}^{q\bar{q}}$ where the $\frac{1}{2}$ comes from a $\boldsymbol{\lambda}_i \boldsymbol{\lambda}_j$ colour dependence [2]. On top of the potential, the paper explains that a phenomenological three-body contribution will be deducted from the final energies of states. The justification for this term is that it leads to very good results. The contribution is defined as

$$V_{123} = \frac{C}{m_1 m_2 m_3}. \tag{7.4}$$

The parameters of the model are then given as

$$\begin{aligned} m_u = m_d = 0.315\text{GeV};\ m_s = 0.577\text{GeV};\ m_c = 1.836\text{GeV};\ m_b = 5.227\text{GeV}; \\ \kappa = 0.5069;\ \sigma = 0.1653\text{GeV}^2;\ K = 0.8321\text{GeV};\ \kappa' = 1.8609; \\ A = 1.6553\text{GeV}^{B-1};\ B = 0.2204;\ C = 2.02 \cdot 10^{-3}\text{GeV}^4. \end{aligned} \tag{7.5}$$

7.2 Optimisation Procedure

In this section, we will demonstrate the optimisation procedure for the case of baryons. Which means finding the most optimum value for the variational parameter ω for a given baryon state. The optimisation procedure in the three-body case will be very similar as the one previously seen in the meson case, chapters 3 and 5. Following the principles of the variational method (see Sec. 2.1), we will obtain the optimum value of ω using a golden section search algorithm described previously in Sec. 2.6.

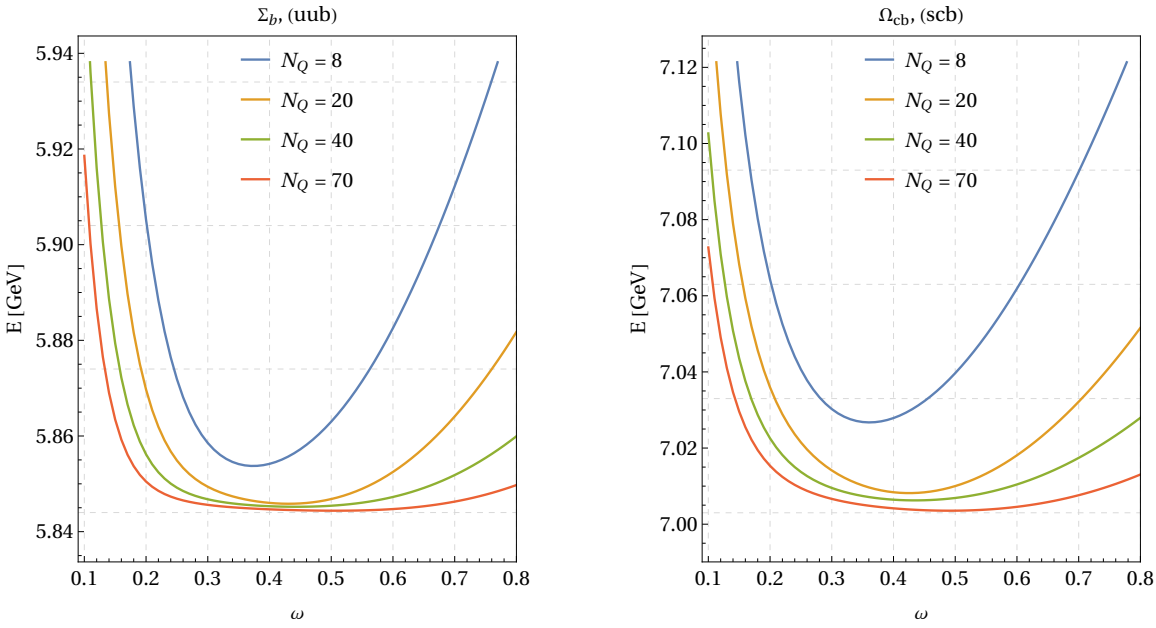

Figure 7.1: Plotting the optimisation procedure of two distinct baryon states. Showing increasing stability as number of basis functions (N_Q) increases.

The variational method will always give energies that are slightly above the "true" value. How much above the "true" value will be dependent on the number of basis functions we use for the approximation. The more basis functions we use, the closer we get to the true value. The plots in Fig. 7.1 demonstrate the stability of the results. As we increase the number of spin-space basis functions N_Q, the minimum value of energy decreases. We can see that if we continued to increase the number of basis functions the minimum energy would only decrease by a few MeV. Eventually a point

will be reached where increasing the number of basis functions decreases the energy by an insignificant amount. At this point we can be confident that the generated results are stable. When calculating various observables we will make sure to use enough basis functions to yield stable results.

7.3 Results

In this section, we will compare the results obtained using our code with ones presented in Ref. [2]. We will be comparing various different observables starting with the masses of the baryons and moving on to expectation values of; the wavefunction at the origin, the rms radii of different quark pairs for different baryon states. As well as the mass mean-square radius of different baryons. We will also show diagrams of the shapes of different baryon states deduced from the obtained rms radii expectation values between quarks.

7.3.1 Masses

In Tab. 7.1, we compare ground state ($J^P = \frac{1}{2}^+$) baryon masses obtained using our method with other works and the Particle Data Group (PDG) records. Note that the model we solved in our work has been taken from Ref. [2], thus we expect to reproduce their results. We divided the table into three sections, where the first section is reserved for baryons with all different quarks. The second section, contains baryon states which are composed of two identical quarks and one different quark, and the last section contains baryon states with all identical quarks.

The size of the set of spin-space basis functions we have used for our predictions is determined by the the maximum energy of the basis states γ_{max}. We only consider

spin-space basis functions with energies $\gamma \leq \gamma_{max}$. In chapter 6 we have shown an example of a spin-space basis set where we have chosen $\gamma_{max} = 2$ which has yielded 8 spin-space basis functions $|\phi_i\rangle$ (see Eq. 6.30)). For our ground state mass predictions here, we have used $\gamma_{max} = 14$ yielding us 240 spin-space basis functions. However, as discussed in chapter 6, for baryons with two or three identical quarks, the pool of basis functions is reduced due to the Pauli exclusion principle. Yielding only 120 spin-space basis functions for baryons with two equal quarks and only 31 for baryons with three identical quarks.

Baryon	Our Work	Ref. [2]	Ref. [27]	PDG
Ξ_c(usc)	2464	2467	2466	2467.71 ± 0.23
Ξ_b(usb)	5802	5806	5806	5791.90 ± 0.50
Ξ_{cb}(ucb)	6914	6915	7011	-
Ω_{cb}(scb)	7002	7003	7136	-
Λ_c(udc)	2279	2285	2268	2286.46 ± 0.14
Σ_c(uuc)	2454	2455	2455	2453.97 ± 0.14
Ω_c(ssc)	2674	2675	2718	2695.20 ± 1.70
Ξ_{cc}(ccu)	3606	3607	3676	3621.60 ± 0.40
Ω_{cc}(ccs)	3708	3710	3815	-
Λ_b(udb)	5632	5638	5612	5619.69 ± 0.17
Σ_b(uub)	5844	5845	5833	5810.56 ± 0.25
Ω_b(ssb)	6033	6034	6081	6045.20 ± 1.20
Ω_{ccb}(ccb)	8018	8019	8245	-
Ξ_{bb}(bbu)	10195	10194	10340	-
Ω_{bb}(bbs)	10267	10267	10454	-
Ω_{bbc}(bbc)	11217	11217	11535	-
Ω_{ccc}(ccc)	4799	4799	5325	-
Ω_{bbb}(bbb)	14401	14398	15097	-

Table 7.1: Comparing masses obtained using our method with other works and the Particle Data Group (PDG) records. Note the model we solved in our work has been taken from Ref. [2], thus we expect to reproduce their results. First section contains baryons with all different quarks, second section contains baryons with two equal quarks and last section contains baryons with all equal quarks. Same number of quanta used for each group of baryons, ($2n+l+2N+L \leq 14$,) but different number of basis functions. For first group there are 240 basis functions, 120 for two-equal-mass case and for all-equal-mass case we have a total of 31 basis functions.

Looking at Tab. 7.1, we find that we are able to reproduce the results obtained in Ref. [2]. The largest mass difference observed is found in the Λ_c(udc) baryon, our method predicts its mass to be 6 MeV less than found in Ref. [2]. An interesting observation is that for the lighter baryon states, our predictions tend to be lower than ones found in Ref. [2], and for the heavier states, our predictions either agree or are only slightly higher than in Ref. [2], as is the case for the two heavy baryons Ξ_{bb}(bbu) or Ω_{bbb}(bbb).

The masses obtained in Ref. [27] listed in Tab. 7.1 were obtained using a very similar variational approach to ours, however, with a significantly lower number of basis functions used, this could explain the rather large disparity between our results and the fact that that masses obtained by Ref. [27] are higher than the ones obtained in our work. This could in part be explained by the fact that the variational method obtains an upper bound on the particle mass, and the more basis functions used, the closer the result will be to the model's ground truth. Since we have used a much larger set of basis functions our results are expected to lie closer to the true baryon mass predicted by the model. On the other hand, the disparity could also be in part due to the use of different models that were solved by us and Ref. [27].

7.3.2 Mass Mean-Square Radius

In this section, we will compare our calculation of the mass mean-square radius with the results found in Ref. [2], for different baryons. We will also give our results of the root mean square (r.m.s.) radius for each pair of quarks in a given baryon.

In Ref. [2], the mass mean-square radius which is an observable used to analyse the overall size of a baryon is defined as

$$\langle R_m^2 \rangle = \langle \Psi | \sum_{i=1}^{3} \frac{m_i}{M} (\boldsymbol{x}_i - \boldsymbol{\mathcal{R}})^2 | \Psi \rangle. \tag{7.6}$$

Where, $\boldsymbol{\mathcal{R}}$ is the centre of mass (c.o.m.) coordinate of the three-body system and $\boldsymbol{x}_i$ are the positions of the three quarks in the system. M is the total mass of all quarks.

The quantity $(\boldsymbol{x}_i - \boldsymbol{\mathcal{R}})$ is related to $\boldsymbol{R}_i$ as follows,

$$(\boldsymbol{x}_i - \boldsymbol{\mathcal{R}}) = -\frac{m_j + m_k}{M} \boldsymbol{R}_i. \tag{7.7}$$

Therefore, we can express $\langle R_m^2 \rangle$ in terms of $\boldsymbol{R}_i$'s

$$\langle R_m^2 \rangle = \sum_{i=1}^{3} \frac{m_i}{M} \left(\frac{m_j + m_k}{M} \boldsymbol{R}_i \right)^2 . \tag{7.8}$$

This expression for the mass mean-square radius is linear in $\boldsymbol{R}$, making integrals easy. We have also obtained results for the root mean square radius between each pair of quarks which we define as $\langle r_i^2 \rangle^{1/2}$. We compare our results of $\langle R_m^2 \rangle$ with Ref. [2] in Tab. 7.2 where we also give values of r_{rms} for each unique pair of quarks.

Table 7.2: Results of the root mean square radius (r_{rms}) between different pairs of quarks in baryons, given in femtometers and as ratios. Table also contains comparison of the mass mean-square radius $\langle R_m^2 \rangle$ obtained using our numerical method compared with results found in Ref. [2].

	Pair	r_{rms} (fm)	r_{rms} (ratios)	$\langle R_m^2 \rangle_{\text{Ours}}$ [fm^2]	$\langle R_m^2 \rangle_{\text{Silv}}$ [fm^2]
Λ_c(udc)	ud	0.7699	1	0.105	0.104
	uc	0.7072	0.92		
Σ_c(uuc)	uu	0.924	1	0.121	0.121
	uc	0.751	0.81		
Λ_b(udb)	ud	0.764	1	0.045	0.045
	ub	0.675	0.88		
Σ_b(uub)	uu	0.930	1	0.055	0.054
	ub	0.739	0.79		
Ξ_c(usc)	us	0.729	1	0.104	0.104
	uc	0.702	0.96		
	sc	0.612	0.84		
Ω_c(ssc)	ss	0.721	1	0.108	0.108
	sc	0.611	0.85		
Ξ_b(usb)	us	0.721	1	0.048	0.048
	ub	0.668	0.93		
	sb	0.567	0.79		
Ω_b(ssb)	ss	0.721	1	0.055	0.054
	sb	0.583	0.81		
Ξ_{cc}(ucc)	uc	0.688	1	0.083	0.083
	cc	0.477	0.69		
Ξ_{cb}(ucb)	uc	0.677	1	0.046	0.046
	ub	0.662	0.98		
	cb	0.400	0.59		
Ξ_{bb}(ubb)	ub	0.657	1	0.33	0.33
	bb	0.296	0.45		

Ω_{cc}(scc)	sc	0.575	1	0.79	0.78
	cc	0.466	0.81		
Ω_{cb}(scb)	sc	0.560	1	0.46	0.045
	sb	0.537	0.96		
	cb	0.390	0.70		
Ω_{bb}(sbb)	sb	0.524	1	0.032	0.032
	bb	0.289	0.55		
Ω_{ccc}(ccc)	cc	0.455	1	0.069	0.069
Ω_{ccb}(ccb)	cc	0.426	1	0.041	0.040
	cb	0.368	0.86		
Ω_{cbb}(cbb)	cb	0.342	1	0.028	0.028
	bb	0.269	0.787		
Ω_{bbb}(bbb)	bb	0.248	1	0.021	0.021

In Tab. 7.3, we compare the same pair of quarks found in different baryons. We find that the distance between a pair of quarks changes depending the on the mass of the third quark, generally decreasing as the third quark increases in mass. As expected, we also see that the size of the baryon, defined by the observable $\langle R_m^2 \rangle$ decreases for heavier baryon states.

	uu	ud	us	uc	ub	ss	sc	sb	cc	cb	bb	$\sqrt{\langle R_m^2 \rangle}$(fm)
Λ_c(udc)	-	0.770	-	0.707	-	-	-	-	-	-	-	0.324
Σ_c(uuc)	0.924	-	-	0.751	-	-	-	-	-	-	-	0.348
Λ_b(udb)	-	0.764	-	-	0.675	-	-	-	-	-	-	0.212
Σ_b(uub)	0.930	-	-	-	0.739	-	-	-	-	-	-	0.232
Ξ_c(usc)	-	-	0.729	0.702	-	-	0.612	-	-	-	-	0.322
Ω_c(ssc)	-	-	-	-	-	0.721	0.611	-	-	-	-	0.329
Ξ_b(usb)	-	-	0.721	-	0.668	-	-	0.567	-	-	-	0.219
Ω_b(ssb)	-	-	-	-	-	0.721	-	0.583	-	-	-	0.232
Ξ_{cc}(ucc)	-	-	-	0.688	-	-	-	-	0.477	-	-	0.288
Ξ_{cb}(ucb)	-	-	-	0.677	0.662	-	-	-	-	0.400	-	0.214
Ξ_{bb}(ubb)	-	-	-	-	0.657	-	-	-	-	-	0.296	0.182
Ω_{cc}(scc)	-	-	-	-	-	-	0.575	-	0.466	-	-	0.279
Ω_{cb}(scb)	-	-	-	-	-	-	0.560	0.537	-	0.390	-	0.212
Ω_{bb}(sbb)	-	-	-	-	-	-	-	0.524	-	-	0.289	0.179
Ω_{ccc}(ccc)	-	-	-	-	-	-	-	-	0.455	-	-	0.263
Ω_{ccb}(ccb)	-	-	-	-	-	-	-	-	0.426	0.368	-	0.200
Ω_{cbb}(cbb)	-	-	-	-	-	-	-	-	-	0.342	0.269	0.167
Ω_{bbb}(bbb)	-	-	-	-	-	-	-	-	-	-	0.248	0.145

Table 7.3: The $r_{\rm rms} \equiv \langle r_i^2 \rangle^{1/2}$ [fm], for each pair of quarks in a given baryon.

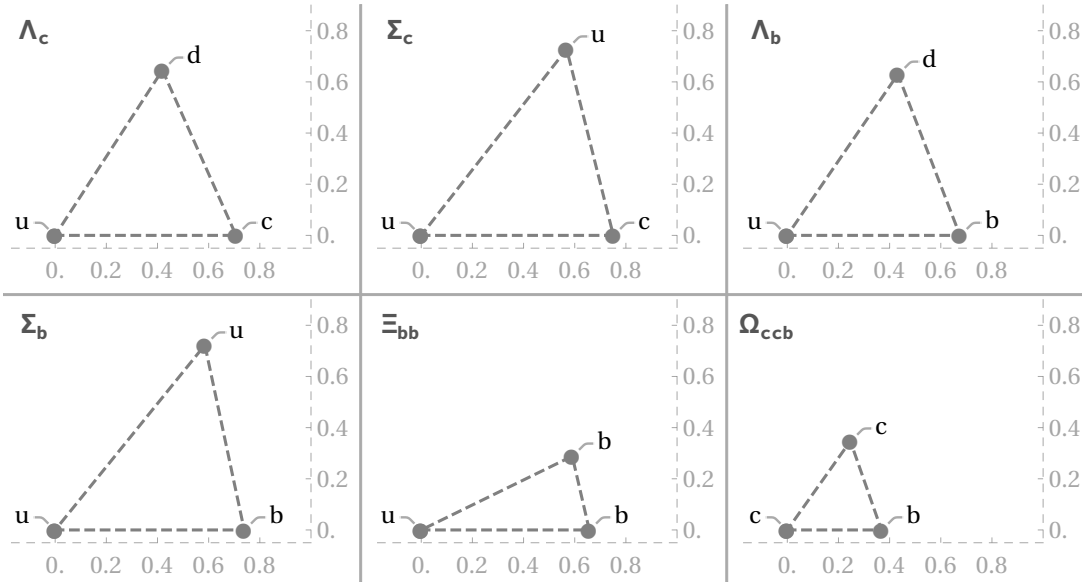

Figure 7.2: Visualisation of expectation values of the $r_{\text{rms}} = \langle r^2 \rangle^{1/2}$ (the distance between each pair of quarks in a baryon) for different baryons. Drawn to scale presented in femtometers (fm).

In Fig. 7.2, we plot the relative distances between quarks showing the estimated shapes of different baryons in their ground states. We note that the plots are drawn to scale, moreover, all shapes are plotted on the same scale to be able to compare the shapes of different baryons. In Fig. 7.3 we show how the shape of the Λ_c(udc) baryon changes for different excited states. In Fig. 7.4 we show the same style of plots but for excited states of the Ξ_{bb}(ubb) baryon. We can see that the b-quarks clump closer together and the u-quark sits further away, this is most prominent for the $n = 0$ and $n = 4$ excited states.

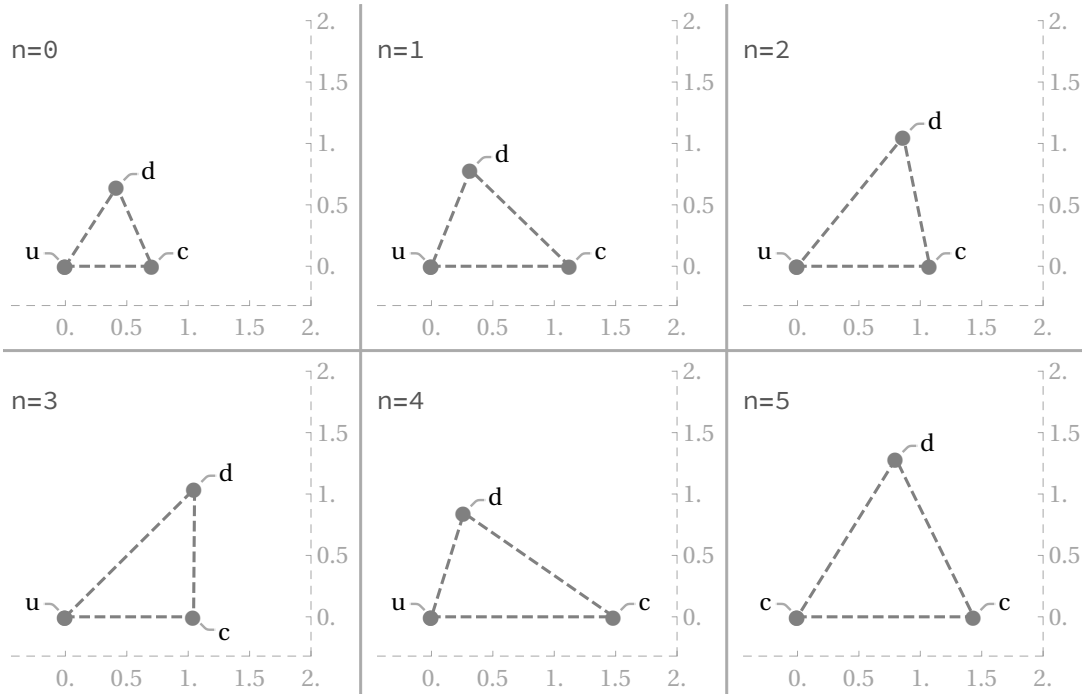

Figure 7.3: Visualisation of how the r_{rms} radius for each pair of quarks changes for different excited states of the Λ_c baryon. $n = 0$ is the ground state, $n = 1$ is the first excited state, and so on. Scale presented in femtometers (fm).

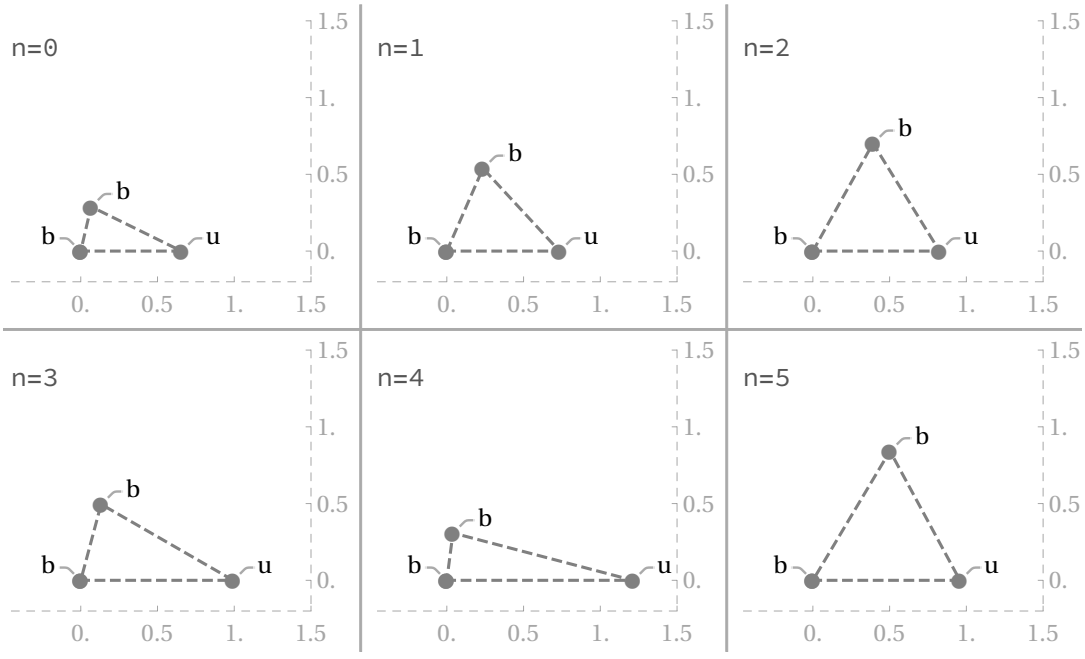

Figure 7.4: Visualisation of how the r_{rms} radius for each pair of quarks changes for different excited states of the Ξ_{bb} baryon, $n = 0$ is the ground state, $n = 1$ is the first excited state, and so on. Scale presented in femtometers (fm).

7.3.3 Ladder Plots

In this final section, we compare the plots of excited states with results found in Ref. [2]. The paper showcases plots of various excited baryon states showing their energies for both negative and positive parity baryons with $\frac{1}{2} \leq J \leq \frac{7}{2}$.

However, no numerical result tables of the masses of these states have been provided, together with the ladder plots, we only made comparisons between ours and those found in the paper by-eye. By comparing our results we have found a good degree of agreeableness.

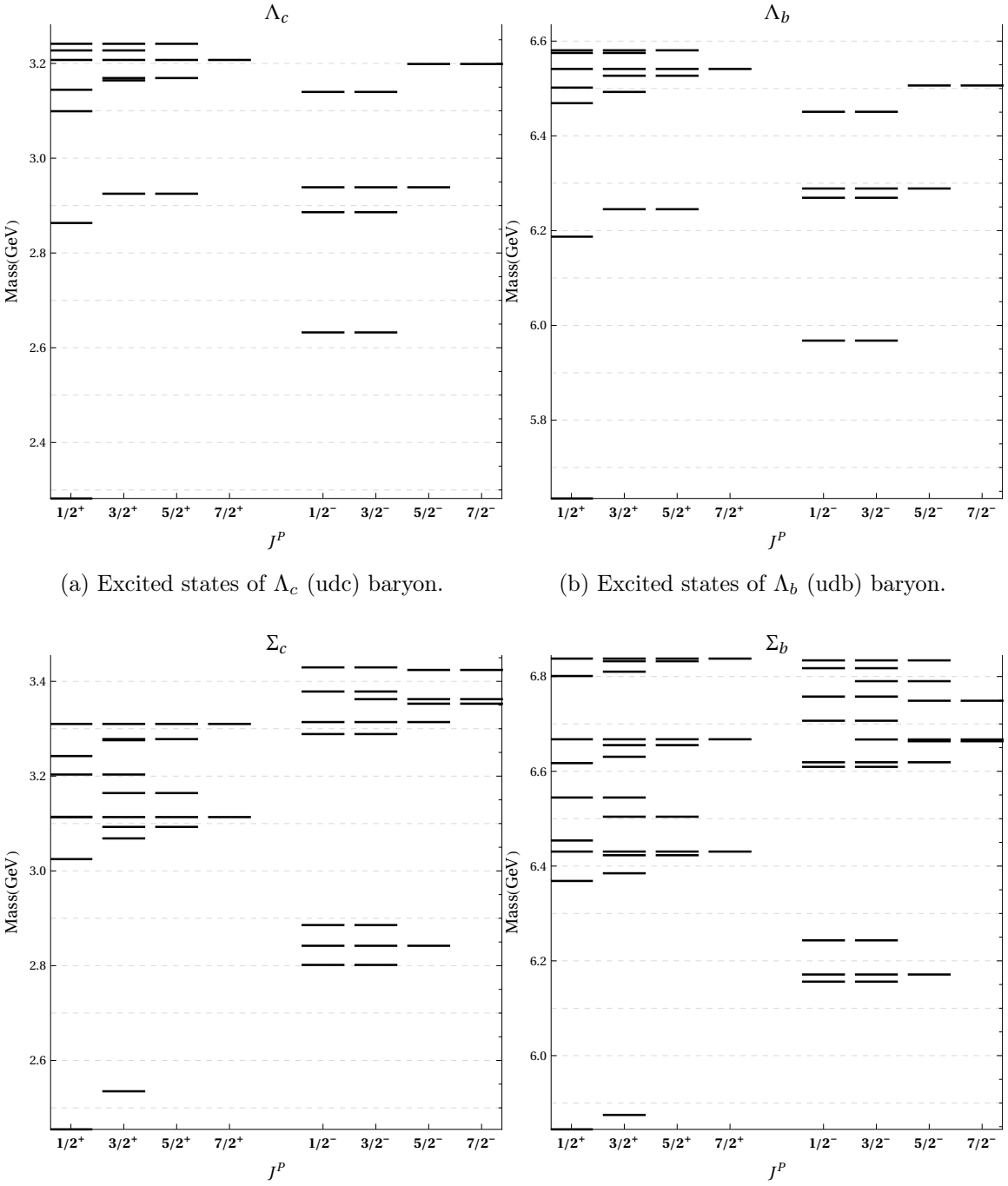

(a) Excited states of Λ_c (udc) baryon.

(b) Excited states of Λ_b (udb) baryon.

(c) Excited states of Σ_c (uuc) baryon.

(d) Excited states of Σ_b (uub) baryon

Figure 7.5: Excited states of single-heavy-quark baryons. The y-axis in each plot starts from the mass of the ground state of that baryon. We only show excited states which are up to 1 GeV above the ground state.

In Fig. 7.5 we plot the excited states of baryons with a single heavy quark. The

y-axis starts from the ground state of each baryon and and we only include excited states that are up to 1 GeV above the ground state. We would like to note that if we take a look at the patterns of the excited states of the Λ_c and the Λ_b baryons, they are approximately similar. This is expected since the only difference between the two states is the mass of the third quark which is responsible for slightly different signatures. For example, if we look at the two degenerate negative parity states with $J^P = \frac{1}{2}^-, \frac{3}{2}^-$ we see that those appear both in the Λ_c and Λ_b baryons, and then above those two states, there is a collection of 5 states (2 degenerate states and above them 3 degenerate states) however, in the Λ_b baryon they seem to be closer together in energy than in the Λ_c baryon. Similar patterns can be seen if we compare the Σ_c and the Σ_b baryons.

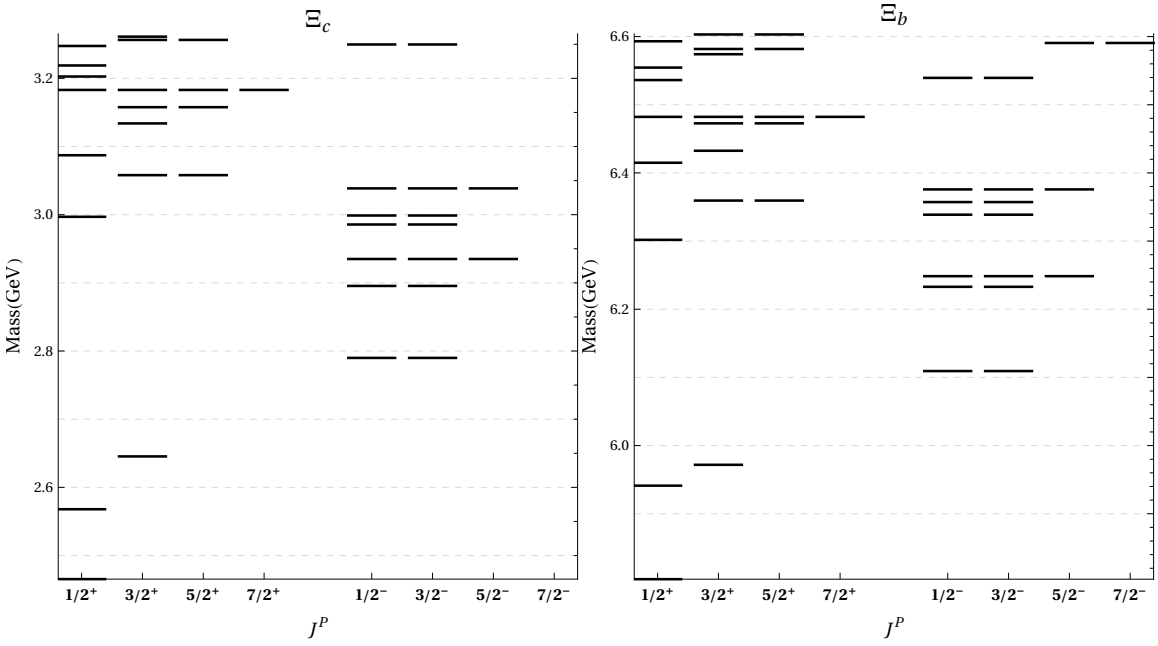

(a) Excited states of Ξ_c (usc) baryon.

(b) Excited states of Ξ_b (usb) baryon.

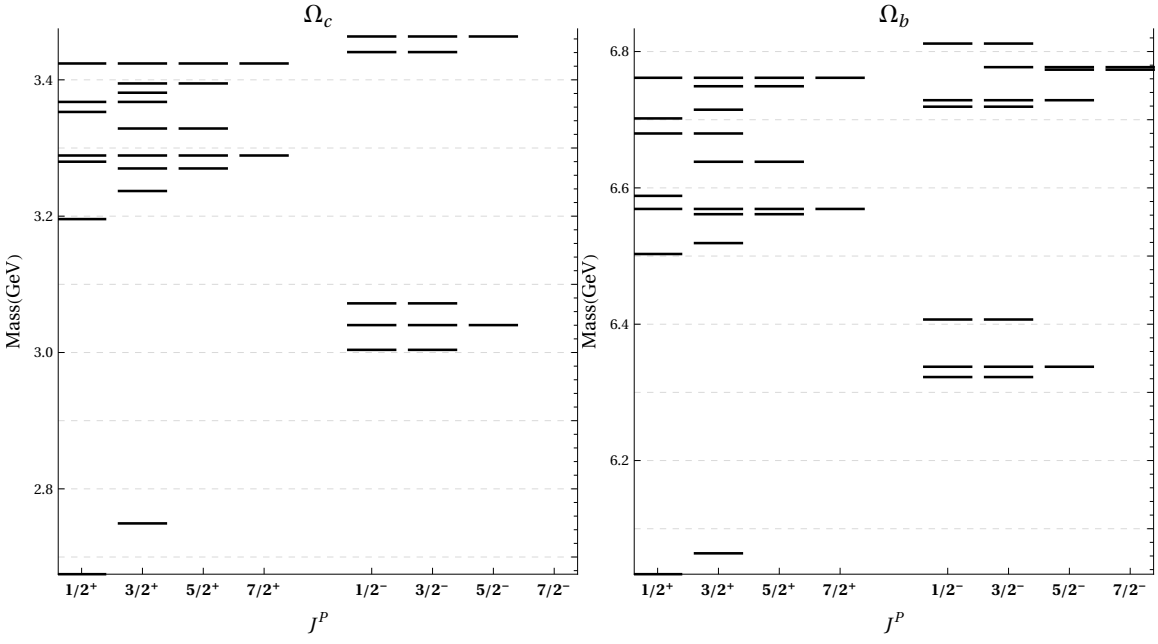

(c) Excited states of Ω_c (ssc) baryon.

(d) Excited states of Ω_b (ssb) baryon

Figure 7.6: Excited states of baryons of type (usQ) in the upper part and (ssQ) in the lower part. The y-axis in each plot starts from the mass of the ground state of that baryon. We only show excited states which are up to 0.8 GeV above the ground state.

In Fig. 7.6 we plot the same ladder plots but for usq baryons in the top two plots and ssq in the bottom two with q being either the c or b quarks. As in the previous plots, the y-axis start from the ground state energy and we include all states that are up to 0.8 GeV above the ground states. We would like to one more time draw the attention to the general patterns between the excited states of the Ξ_c and Ξ_b baryons and likewise for the Ω_c and Ω_b baryons. The excited states have similar patterns because the only difference between each of the two states is the mass of the third quark. Again, we have found a good degree of agreeableness between ours and ones found in Ref. [2] for the baryons and their excited states presented in this figure.

8

Mesons at Finite Temperature

In this chapter, we will discuss two different temperature dependent meson models. We will demonstrate the features of the potentials and how temperature affects the various meson observables, such as meson mass or size in each of the two potentials. The potentials considered in this chapter will be spin-independent, therefore the obtained results will correspond to spin-averaged meson states.

We will be using the same temperature dependent potentials when we come to baryons at finite temperature in Ch. 9. Since this area is relatively unexplored, this chapter will serve as a precursor for our results of baryons at finite temperature. We will be drawing parallels between mesons and baryons in the two chapters to establish a strong case for our baryon results at finite temperature.

In this chapter, we will first present a simpler finite temperature model (Sec. 8.1) and then a relatively more complex one (Sec. 8.2). The latter has been obtained and solved by Karsch et al. [52], we will aim to find solutions to the model with our standard approach using the variational method and we will compare our results with the paper in order to ensure that our method is correct. For the simpler, model presented first, we do not have any prior results to guide us. We use the simpler model because it is relatively easy to implement, and as our main goal is to study baryons at finite temperature, it will serve as a good place to start.

8.1 Simple T-dependent Potential

In this section we will use a simple temperature dependent model, where the temperature dependence appears in the form of a temperature dependent string tension $\sigma(T) = \sigma[1 - (T/T_C)^2]^{1/2}$, where T_C is a critical temperature at which the string tension vanishes. This model was proposed by Pisarski et al. in Ref. [68]. We will use it to compute masses of various mesonic states as a function of T/T_C.

8.1.1 Potential Description

The full temperature-dependant meson potential used in this section is a modified version of the Cornell potential based on a temperature-dependent string tension proposed in Ref. [68] and is given as,

$$V(r,T) = -\frac{\alpha}{r} + \left(\sigma\sqrt{1 - T^2/T_C^2}\right)r, \tag{8.1}$$

where, $\alpha = 0.471$, $\sigma = 0.192\text{GeV}^2$, $m_c = 1.320\text{GeV}$ and $m_b = 4.746$ GeV. We see that at $T = 0$ we recover the standard Cornell potential. At $T = T_C$, the string tension completely vanishes and the potential is no longer confining. When $T = T_C$ the potential at infinity is simply $V(\infty, T_C) = 0$ if we ignore the mass of the quarks. This means that the energy of any bound states at $T = T_C$ will be below 0 and the energy of all other states will lie in the continuum regime. The parameters for this model have been borrowed from Ref. [52] which outlines the potential that will be used in Sec. 8.2. Due to the similarity of the two models we are able to use the same model parameters for both, this results in the two models being equivalent at zero temperature, this is useful for comparing the two models.

In Fig. 8.1 we illustrate the potential specified in Eq. (8.1). The first feature of the

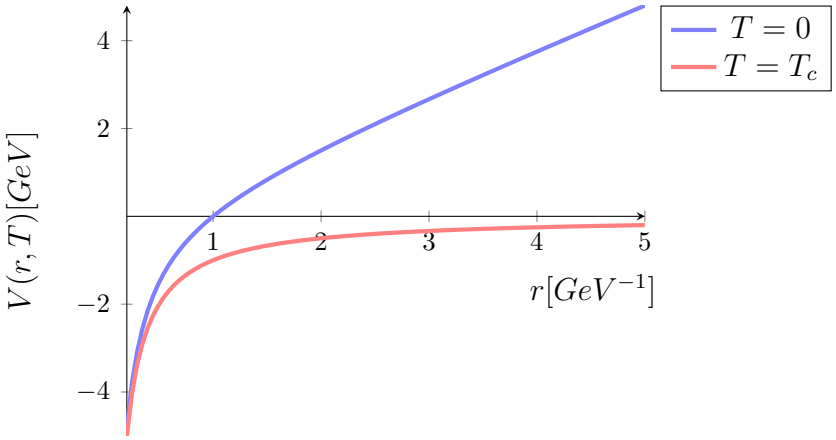

Figure 8.1: Plot of Eq. (8.1) at $T = 0$ and $T = T_C$ with $\alpha = \sigma = 1$, demonstrates "flattening" of the potential as temperature increases.

potential that we notice is that increasing the temperature T leads to a flattening of the potential. In the figure, we see that the potential tends to zero as $T \to T_C$. The temperature parameter T suppresses the linear (confining) term of the potential. Therefore, this temperature dependent model allows us to study the influence of the linear part of the potential on meson observables. In the next section we will see how the masses of various mesons change as a function of T/T_C.

8.1.2 Results

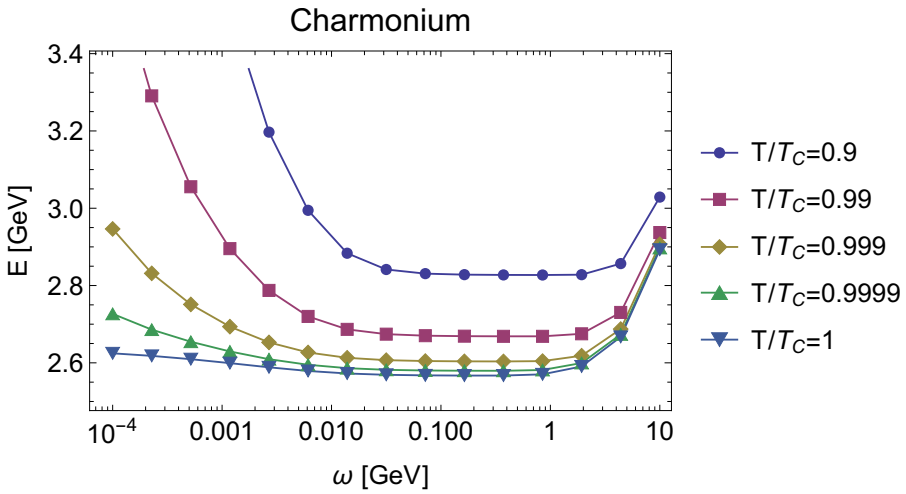

Figure 8.2: Energy of the charmonium ground state as a function of ω for various temperatures as a fraction of T_C.

First, we will showcase the variational method for this model. The variational method relies on diagonalising the Hamiltonian matrix and finding an optimum value of ω such that the eigenvalue of interest is minimised. In Fig. 8.2 we show the energy of the charmonium ground state as a function of ω for various values of T/T_C. In the plot we can see that a minimum energy can be obtained at all temperatures including the critical temperature ($T/T_C = 1$). The presence of a minimum is indicative of bound states. Although the minimum is not as pronounced at critical temperature as it is at $T/T_C = 0.9$, we are still able to identify a minimum. Therefore, for this model we still possess bound states even at critical temperature. We are pointing this out because when we come to the second temperature-dependent model in Sec. 8.1, at a certain value of the effective temperature parameter $\mu(T)$, we will not be able to identify a minimum, the energy will decrease monotonically with ω. Which is how we will be able identify the critical point for that model.

Let us now look at how this potential affects the masses of various meson states. In Fig. 8.3 we plot the masses of various excitations of the charmonium ($c\bar{c}$) state as a

function of T/T_C.

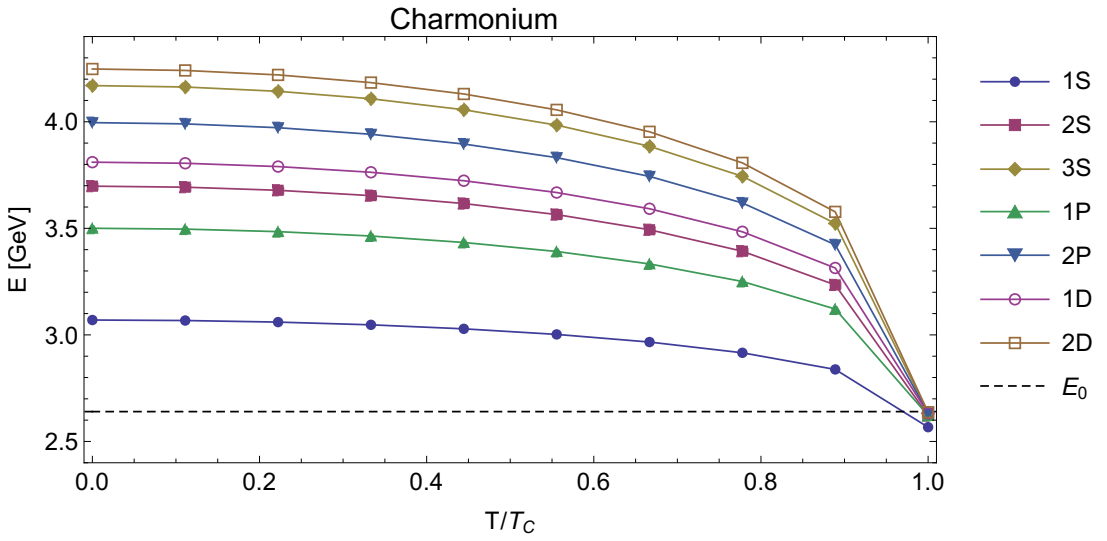

Figure 8.3: Charmonium state masses as function of T/T_C for the potential in Eq. (8.1), $E_0 = 2m_c$

What we find is the mass of the $c\bar{c}$ states decreases as temperature increases. We also plot in Fig. 8.3 the line $E_0 = 2m_c$. And we find that, at critical temperature, all the states fall under the line. This happens because bound states must have an energy less than or equal to the potential at infinity. At $T = T_C$ the potential at infinity is equal to $2m$ (the linear term vanishes and the Coulomb term is proportional to $1/r$ which goes to zero as $r \to \infty$) therefore in this model the only terms that remain are the masses of the quarks.

In Fig. 8.4 we make a similar plot as the one above but for the bottomonium states. We see a similar pattern with all the states falling below the line $E_0 = 2m_b$ at $T = T_C$.

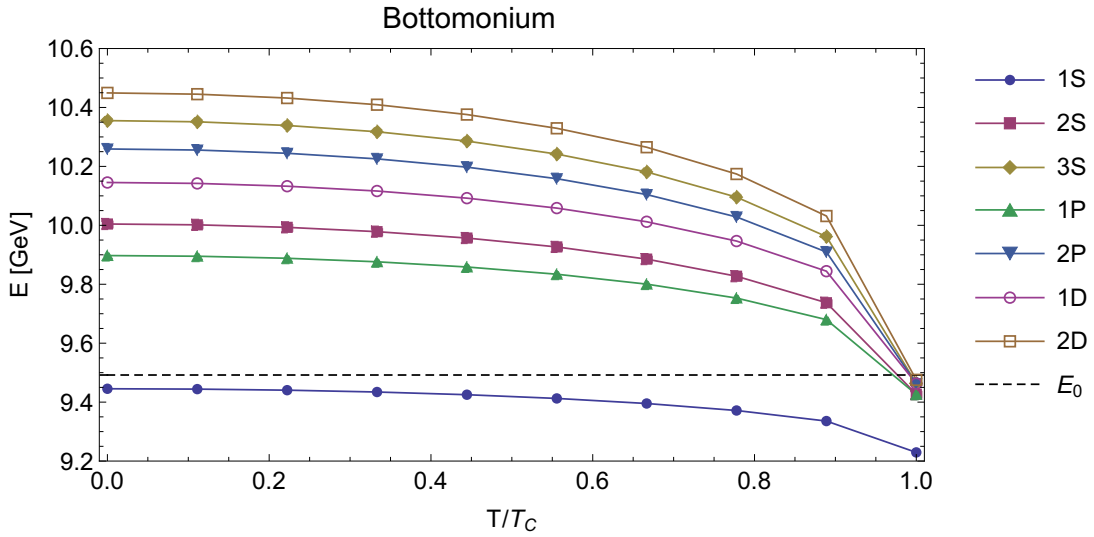

Figure 8.4: Bottomonium state masses as function of T/T_C for the potential in Eq. (8.1), $E_0 = 2m_b$.

8.2 Debye Mass Screened Potential

In this section we will be solving a second finite temperature meson model. In this model both the linear and the Coulomb part of the confining potential are affected by colour charge screening. We use the same potential as found in a paper by Karsch et al. (1996) [52]. We will first describe the potential and then present our obtained results for various observables and compare them with the results presented in the paper.

8.2.1 Potential Description

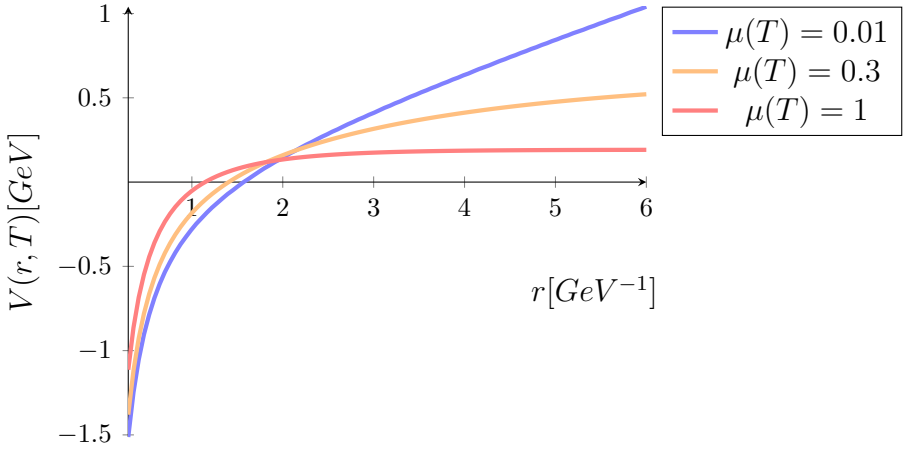

Figure 8.5: Plot of Eq. (8.2) at different $\mu(T)$ with $\sigma = 0.192$GeV and $\alpha = 0.471$, demonstrates "flattening" of the potential as $\mu(T)$ increases.

The screened potential that we will be using in this section is described in Ref. [52] as

$$V(r,T) = -\frac{\alpha}{r}e^{-\mu(T)r} + \frac{\sigma}{\mu(T)}(1 - e^{-\mu(T)r}), \tag{8.2}$$

where $\mu(T) = 1/r_D(T)$, $\mu(T)$ will be referred to as the screening mass and $r_D(T)$ is the screening length. The parameters of this model are given as $\sigma = 0.192\text{GeV}^2$, $\alpha = 0.471$, $m_c = 1.320$ GeV and $m_b = 4.746$ GeV [52]. The same model parameters have been used previously in Sec. 8.1, thus the potentials in Eqs. (8.1) and (8.2) are the same when $\mu(T) = T = 0$.

Since $\mu(T)$ completely contains the temperature dependence of the model, we will sometimes refer to $\mu(T)$ as the effective temperature parameter. A few examples of Eq. (8.2) with different values of $\mu(T)$ have been shown in Fig. 8.5. The effect of colour charge screening is similar to the one seen in the first potential in Fig. 8.1; increasing the effective temperature paramter $\mu(T)$ leads to a flattening of the potential. Note that, at $\mu(T) = 0$ the Cornell potential is recovered.

One new property of this potential when compared to the one in Eq. (8.1) is that the critical point, i.e. a point at which a state is deemed to be deconfined is not so trivial. In Sec. 8.1, the temperature parameter has been defined as a fraction of the critical temperature, with $T/T_C = 1$ being the critical point, there was never a need for identifying T_C explicitly. For the potential we will be using in this section, determining a critical point $\mu(T = T_C) \equiv \mu_c$ is necessary. Each state will have a unique value of μ_c at which it dissociates. In the paper, Karsch et al. [52] obtained this through the dissociation energy defined as

$$E_{\text{dis}}(\mu) = 2m + \frac{\sigma}{\mu} - E(\mu), \tag{8.3}$$

which is positive for bound states and negative for the continuum [52]. The dissociation energy is defined as the value of the potential at infinity ($r = \infty$) minus $E(\mu)$, where $E(\mu)$ is the energy of a meson state at temperature $\mu(T)$, obtained by diagonalising the Hamiltonian. The critical point μ_c is then defined as

$$E_{\text{dis}}(\mu_c) = 0. \tag{8.4}$$

The values of μ_c for various meson states have been obtained by Karsch et al. and are given in Tab. 8.1. We will be using our own method for determining the critical value μ_c which will be based around the variational method. We will define μ_c as the point at which we no longer can find a minimum in the E vs. ω curves. This is illustrated in Fig. 8.6. We will also be using the boundary between bound and continuum states defined as $2m + \sigma/\mu$ to ensure that our method accurately identifies μ_c.

8.2.2 Results

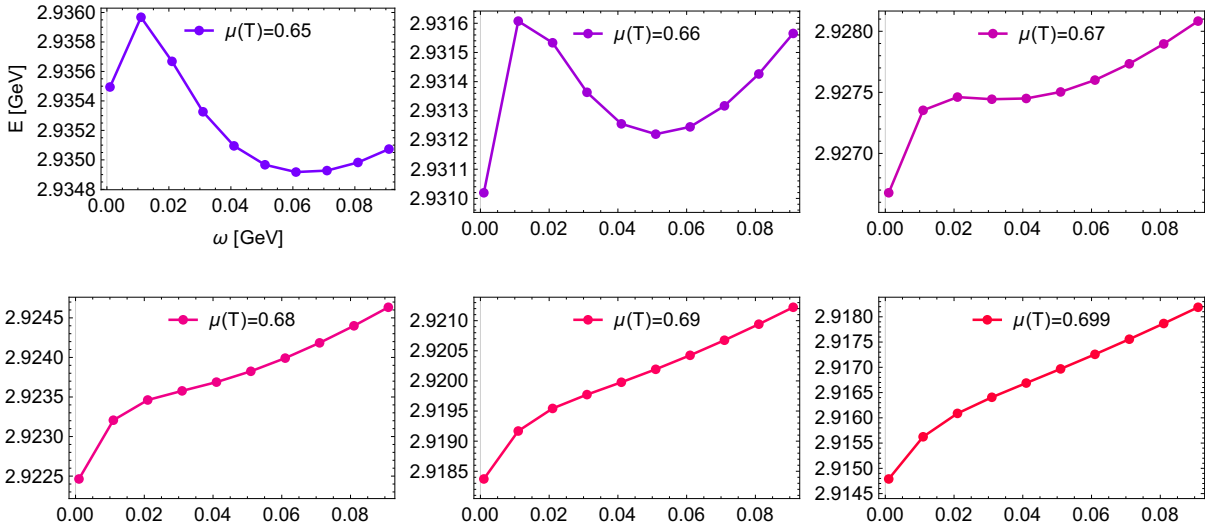

Figure 8.6: Energy of the charmonium ($c\bar{c}$) ground state as a function of ω at different temperatures $\mu(T)$. For these plots we have used only 10 basis functions $N_\phi = 10$.

First, let us discuss the variational method for this temperature dependent model. As an example we will take a look at plots of E vs. ω for the ground state of charmonium ($c\bar{c}$) at different values of $\mu(T)$ as illustrated in Fig. 8.6. The variational method relies on finding the minimum of a states energy as we vary the variational parameter ω. What we see in the plots is that such a minimum only exists up to a certain value of $\mu(T)$, after which point the energy of the state decreases monotonically as ω decreases. We will define the last value of $\mu(T)$ for which a minimum can be identified as μ_c, the point at which the state dissociates. In Ref. [52], Karsch et al. estimate the critical point for the $c\bar{c}$ ground state to be $\mu_c = 0.699$GeV. They do this by using Eq. 8.4 to find at what point the state dissociates. Using our analysis, we find the critical point for the $c\bar{c}$ ground state to be at $\mu_c = 0.67$GeV. Similarly for other meson states, we find our estimates of μ_c to be lower than ones found by Karsch et al.

In the next set of figures, we show that for most calculations for low lying excited

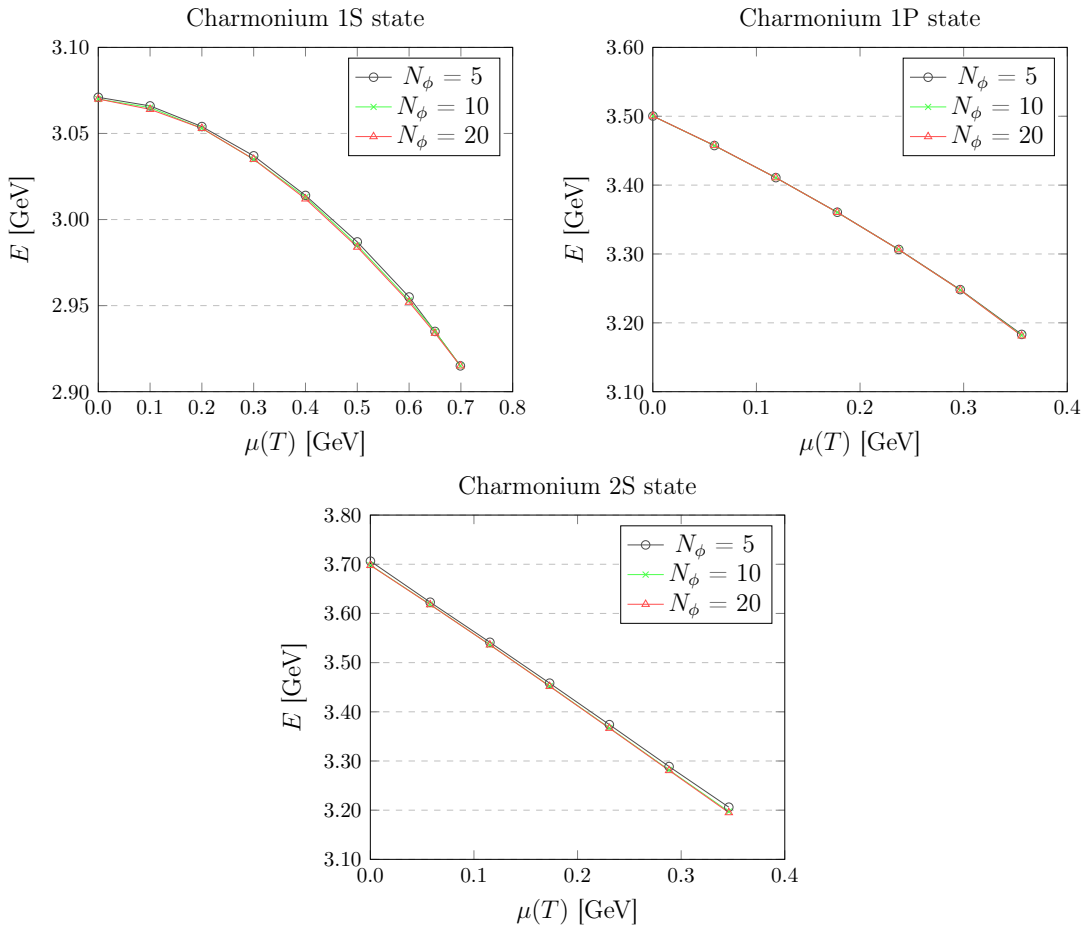

Figure 8.7: Plots showing the energy of the $c\bar{c}$ ground state, and the 1P and 2S excited states as a function of $\mu(T)$, until dissociation occurs, for different numbers of basis functions N_ϕ

states, like the 1S, 1P and 2S states, which are the states we will be focusing on for this model, it is sufficient to use 10 to 20 basis functions to approximate the observable of those states. In Fig. 8.7 we show the energy of three different excitations of the charmonium meson as a function of the screening parameter $\mu(T)$ until the state dissociates. For each plot we show the approximations obtained using 5, 10 and 20 basis functions. We find that the energies for these states overlap showing that there are no significant changes to the results when considering more basis functions, as such, we will be using between 10-20 basis functions for most calculations for this model.

In Fig. 8.8, we plot the *optimised* value of the variational parameter which we denote

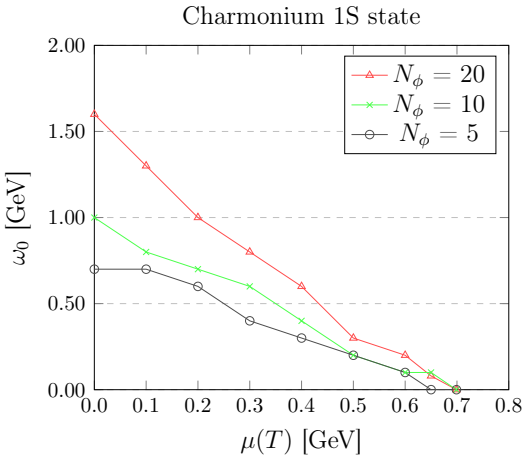

Figure 8.8: On the left, is the energy of the $c\bar{c}$ 1P state as a function of $\mu(T)$ for different numbers of basis functions N_ϕ. On the right, is the same plot but for the 2S state.

as ω_0 as a function of temperature for different numbers of basis functions for the $c\bar{c}$ ground state. We see that the general trend is that the value of ω_0 decreases as temperature increases. Since ω_0 is negatively correlated with the size of the SHO basis functions, this is an indication of the $c\bar{c}$ state getting larger in size as temperature increases. What is also reassuring is that around critical temperature the value of ω_0 tends to 0, indicating that at that point the state becomes infinitely large and can be considered no longer bound.

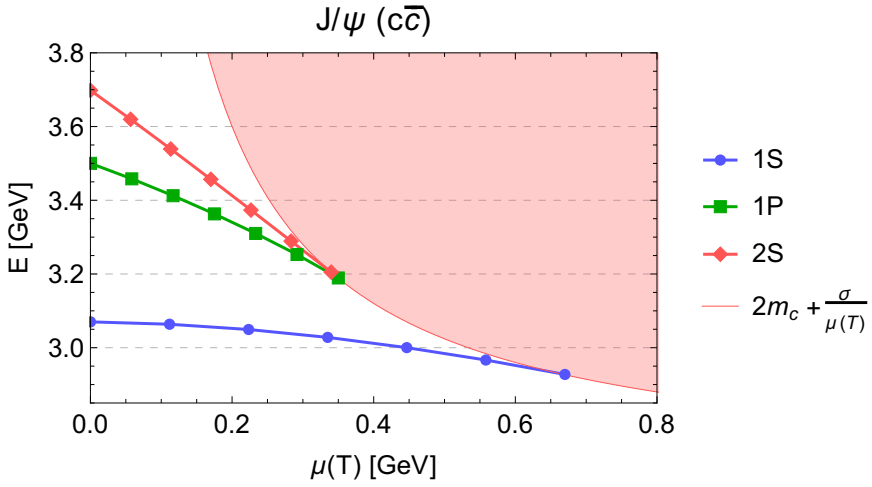

Figure 8.9: Energy of the ground and two excited $c\bar{c}$ states as a function of the effective temperature parameter $\mu(T)$. The red region represents an area where bound states no longer exist, $E_{\text{dis}}(\mu) > 0$, defined in Eq. (8.3).

In Fig. 8.9, we plot the masses of various excited states of charmonium as a function of $\mu(T)$ up to our identified value of μ_c recorded in Tab. 8.1. We also plot the boundary between the bound and unbound states defined by Eq. (8.3). As we see in the plot, we were able to correctly identify the value of μ_c using our method as no state enters the red region but only meets it. We also find in Fig. 8.9, that the masses of the $c\bar{c}$ ground and excited states decrease as $\mu(T)$ increases. We also see that the masses of the excited states decrease more rapidly compared to the energy of the ground state seeming to be more sensitive to temperature effects.

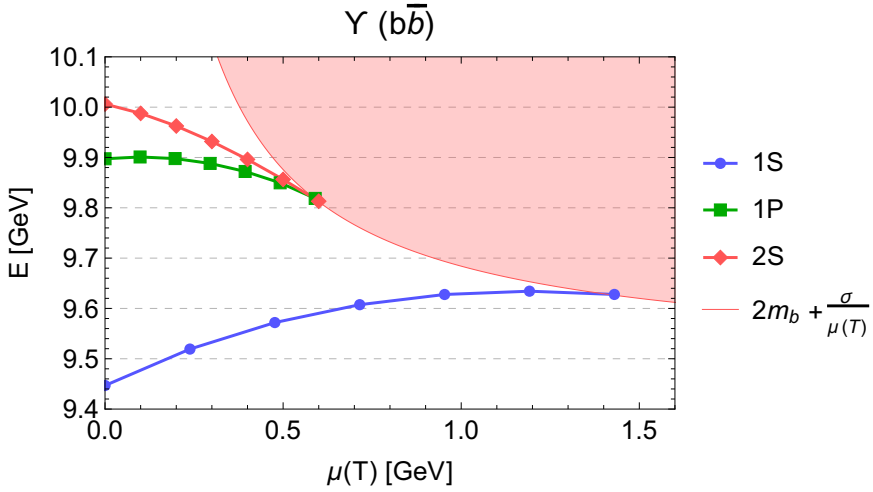

Figure 8.10: Energy of the ground and two excited $b\bar{b}$ states as a function of the effective temperature parameter $\mu(T)$. The red region represents an area where bound states no longer exist, $E_{\text{dis}}(\mu) > 0$, defined in Eq. (8.3).

In Fig. 8.10 we obtain similar predictions as shown in Fig. 8.9 but for the states of the $b\bar{b}$ meson. Contrary to the $c\bar{c}$ meson, in this plot we can see the mass of the ground $b\bar{b}$ state increase as temperature increases. This is believed to be the case because the $b\bar{b}$ ground state is relatively small, approximately half the size of the $c\bar{c}$ ground state (see Tab. 8.2). This makes it more sensitive to the short range part of the potential i.e. the Coulomb part. The decrease in mass of a state can be attributed to the flattening of the linear part of the potential as established in Sec. 8.1. Because the $b\bar{b}$ ground state is relatively small, it is not sensitive to long range effects. At small temperatures it is more sensitive to the short range Coulomb type interaction

which has the opposite effect. We can see that after about $\mu(T) = 1.2$GeV the mass of the ground state starts to decrease, this fits with our interpretation since at higher temperatures the size of the state increases, after which point the meson becomes more sensitive to the linear part of the potential causing the mass to decrease.

		M_{ours} [GeV]	M_{ref} [GeV]	M^c_{ours} [GeV]	M^c_{ref} [GeV]	μ_c^{ours} [GeV]	μ_c^{ref} [GeV]
$c\bar{c}$	1S	3.070	3.070	2.926	2.915	0.670	0.699
	1P	3.500	3.500	3.182	3.198	0.356	0.342
	2S	3.698	3.698	3.196	3.177	0.346	0.357
$b\bar{b}$	1S	9.445	9.445	9.627	9.615	1.441	1.565
	1P	9.898	9.897	9.815	9.829	0.599	0.558
	2S	10.005	10.005	9.810	9.778	0.606	0.671

Table 8.1: Comparing masses at zero and at critical $\mu(T)$, with results obtained by Karsch et al. [52].

In Tabs. 8.1 and 8.2 we compare our results of masses and root-mean-square (rms) radii for various meson ground and excited states with the results obtained by Karsch et al. [52]. We find that our masses at $\mu(T) = 0$ agree with the literature very well. Comparing the masses at critical screening mass μ_c we find that our results differ, this is mostly due to the disparity between our obtained μ_c values. In most cases we predict the state to melt sooner than estimated by Karsch et al. The opposite is true for the $1P$ state, we predict the state to melt at a higher value of $\mu(T)$ than Ref. [52] for both the charmonium and bottomonium mesons.

		r_{ours} (fm)	r_{ref} (fm) [52]
$c\bar{c}$	1S	0.453	0.453
	1P	0.696	0.696
	2S	0.875	0.875
$b\bar{b}$	1S	0.226	0.226
	1P	0.408	0.408
	2S	0.509	0.509

Table 8.2: Comparing our estimate of the r.m.s. radius ($\sqrt{\langle r^2 \rangle}$) at $\mu(T) = 0$ with results obtained by Karsch et al. [52].

In Tab. 8.3, we compare the zero-temperature masses of spin-averaged mesons with the work of others. We find good agreement between different models used. In

Tab. 8.4, we compare the obtained critical values of μ_c obtained by different authors. Very similar models are used for all four columns of the table to study the critical temperature of mesons, those are mainly based on the work of Karsch et al. [52]. However, the authors of Ref. [69] consider relativistic corrections to the model to study the dissociation of mesons. They find that the dissociation energy increases when relativistic corrections are taken into account.

		M (GeV) Our Work	M (GeV) [52]	M (GeV) [14]	M (GeV) [8]
$c\bar{c}$	1S	3.070	3.070	3.097	3.095
	1P	3.500	3.500	3.519	3.522
	2S	3.698	3.698	3.685	3.684
$b\bar{b}$	1S	9.445	9.445	9.433	9.460
	1P	9.898	9.897	9.933	-
	2S	10.005	10.005	10.028	10.016

Table 8.3: Comparing our zero-temperature masses [GeV] of spin-averaged mesons with the work of others.

		μ_c (GeV) Our Work	μ_c (GeV) [52]	μ_c (GeV) [70]	μ_c (GeV) [69]
$c\bar{c}$	1S	0.670	0.699	0.70	0.895
	1P	0.356	0.342	0.34	0.450
	2S	0.346	0.357	0.36	0.455
$b\bar{b}$	1S	1.441	1.565	1.55	1.665
	1P	0.599	0.558	0.57	0.700
	2S	0.606	0.671	0.66	0.720

Table 8.4: Comparing the obtained critical temperature [GeV] of spin-averaged mesons with the work of others.

9 Baryons at finite temperature

In this chapter, we will present our results for two different temperature-dependent baryon models. The baryon models will be obtained by modifying the baryon potential outlined in Eq. (7.2) to include temperature effects. We will be using the same model parameters for the temperature-dependent models as specified in Eq. (7.5). Such that, in the special "zero-temperature" case we will be able to recover said model and obtain same observable values as presented in Ch. 7.

The modifications to the temperature-independent baryon model will be based on two temperature-dependent models we have previously seen in Ch. 8 when working with mesons at finite temperature. One difference between mesons and baryons at finite temperatures is that for the meson case we did not include any hyperfine interactions i.e. the models were spin-independent. However, for baryons at finite temperature we will be including the same spin-spin term that has been considered in the original baryon potential in Eq. (7.2).

9.1 Simple T-Dependent Potential

In this section we will present the first temperature dependent baryon potential model, it is a simple model because it only takes into account how the string tension is affected by temperature. The model depends on a temperature dependent string tension proposed in Ref. [68]. The string tension slowly vanishes as $T \to T_C$ where T is temperature and T_C is some critical temperature at which the string tension vanishes completely. With this model we will be able to isolate the effect of the linear term in the potential and see its effect on the different properties of various baryons. We understand that the linear dependence in the potential is responsible for confinement thus it will be interesting to see what happens as the term gets suppressed until eventually it vanishes. We note that we have seen a similar model previously used for mesons in Sec. 8.1.

9.1.1 Potential Description

For this model the potential between a quark and an antiquark is defined as

$$V_{ij}^{q\bar{q}}(r_k, T) = -\frac{\kappa}{r_k} + \Big(\sigma\sqrt{1-\tfrac{T^2}{T_C^2}}\Big)r_k - K + \frac{8\kappa'}{3m_i m_j \pi^{1/2} r_0^3}\exp\big(-\tfrac{1}{r_0^2}r_k^2\big)\boldsymbol{S}_i\cdot\boldsymbol{S}_j. \quad (9.1)$$

This model is similar to the one seen in the meson case, see Eq. (8.1). Because we want to adapt this potential for baryons we need the corresponding quark-quark potential which is defined as

$$V_{ij}^{qq}(r_k, T) = \frac{1}{2}V_{ij}^{q\bar{q}}(r_k, T), \quad (9.2)$$

where the factor of a half comes from the $\boldsymbol{\lambda}_i\boldsymbol{\lambda}_j$ colour dependence [2]. The total potential for all pairs of particles in the three-body baryon system is then given as

$$V(r_1, r_2, r_3, T) = \frac{1}{2}\Big(V_{12}^{q\bar{q}}(r_3, T) + V_{23}^{q\bar{q}}(r_1, T) + V_{31}^{q\bar{q}}(r_2, T)\Big) \tag{9.3}$$

When $T < T_C$, the model contains an infinite number of bound states, this is due to the presence of the linear part of the potential, consequently, there are no unbound states in this case.

However, at $T = T_C$, the linear term in the potential vanishes, in which case, the model then contains an infinite number of bound states *and* an infinite number of unbound states. The energies of the bound states will lie below E_∞, which is defined as

$$E_\infty = \sum_{i=1}^{3} m_i + V(r_1 = r_2 = r_3 = \infty, T = T_C) - \frac{C}{m_1 m_2 m_3}, \tag{9.4}$$

which is the value of the potential with quarks being infinitely far apart and by default at $T = T_C$, plus the rest masses of the quarks and reduced by the factor $\frac{C}{m_1 m_2 m_3}$ which is the three-body contribution, discussed in Sec. 7.1 and specified in Eq. (7.5). From the definition in Eq. (9.4) and using Eqs. (9.3) and (9.1), we get

$$E_\infty = \sum_{i=1}^{3} m_i - \frac{3}{2}K - \frac{C}{m_1 m_2 m_3}, \tag{9.5}$$

where the potential, as the relative distances between quarks go to infinity and at $T = T_C$, is reduced to the constant $\frac{3}{2}K$. The spectrum of the bound states which lie below E_∞ will resemble the spectrum of the hydrogen atom since at $T = T_C$ the linear term vanishes and all that is left is the Coulomb term and the spin-spin term. It is important to note that this is only an artefact of this model and not a true representation of what happens to baryons at $T = T_C$.

9.1.2 Results

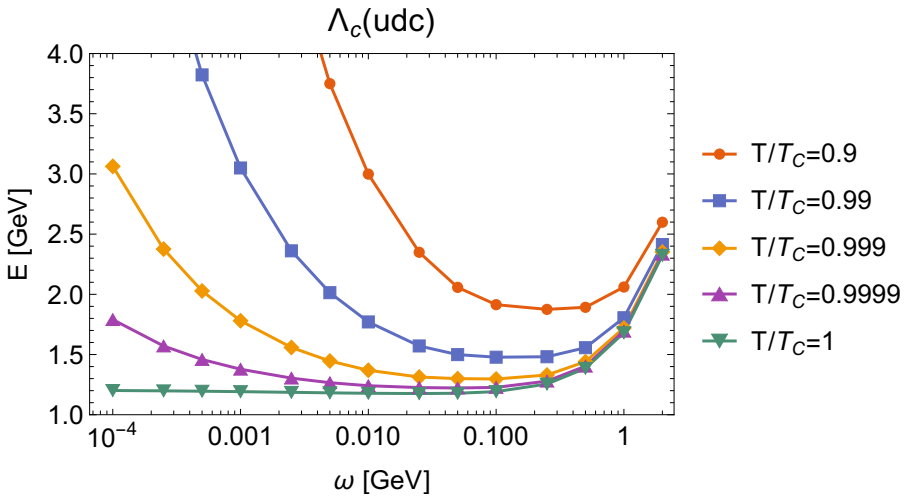

Figure 9.1: A plot of the $J^P = \frac{1}{2}^+$, Λ_c baryon state energies using the potential in Eq. (9.1) at different T/T_C as function of ω plotted on a log scale.

First, we will illustrate the E vs. ω curves which we use to obtain the energies of our states via the variational method. We use the curves to obtain an optimum value of the variational parameter ω by finding the minimum of such plots. In Fig. 9.1 we plot the energy vs. ω for the ground state of the Λ_c baryon. We find that a minimum exists at each value of T/T_C. Upon closer inspection, i.e. taking a closer look at the $T/T_C = 1$ curve in Fig. 9.1, we also find that a minimum exists at $T/T_C = 1$, indicating the presence of bound states even at critical temperature, for this model. This is expected as we have mentioned previously that we should still expect bound states due to the remaining Coulomb term in the potential. We note that this plot is also very similar to the one seen in the corresponding meson case in Fig. 8.2.

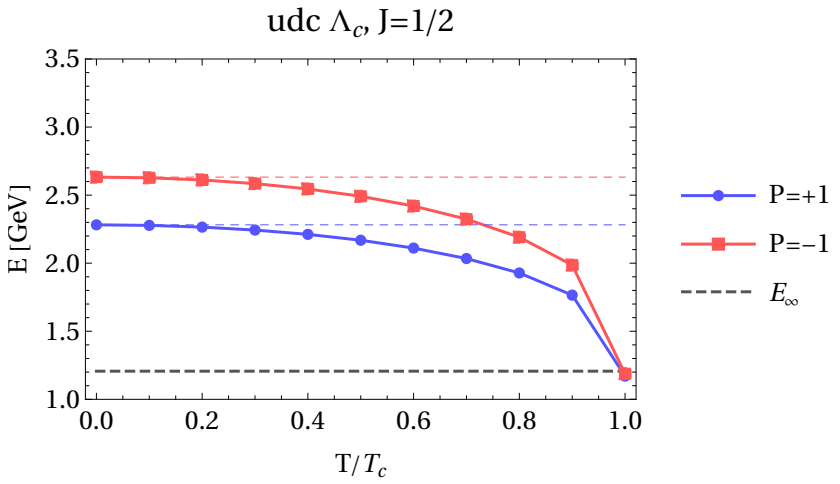

Figure 9.2: Energy of the negative and positive parity Λ_c, $J = 1/2$ baryon ground states as function of T/T_C.

In the next series of Figures (9.2 $\rightarrow$ 9.5), we plot the energy of various baryon ground states as a function of T/T_C comparing the masses of the positive and negative parity states. We also plot the quantity defined in Eq. (9.5) which is the value of the potential at infinity. We find that the mass of both the positive and negative parity baryons decreases as temperature T increases. When critical temperature is reached the mass of the state falls below E_∞ marked on the plots.

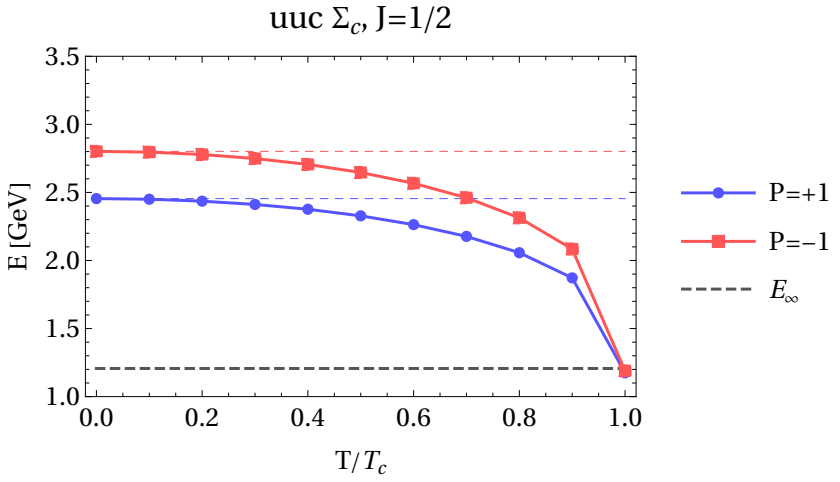

Figure 9.3: Energy of the negative and positive parity Σ_c, $J = 1/2$ baryon states as function of T/T_C.

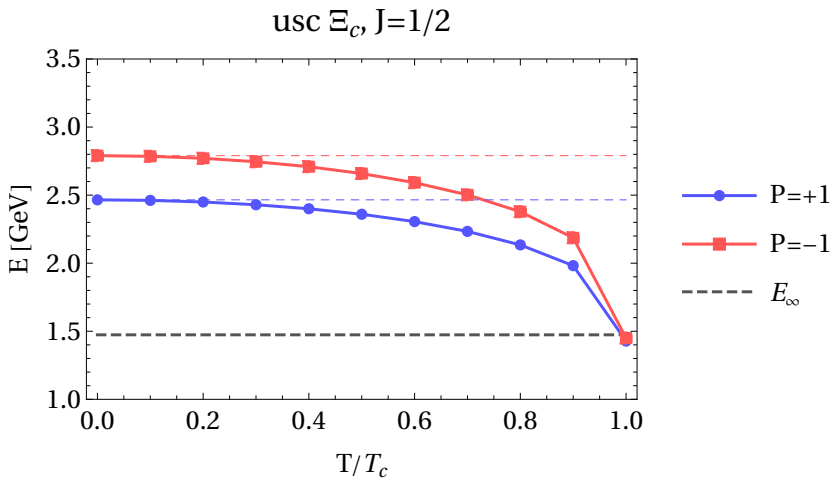

Figure 9.4: Energy of the negative and positive parity Ξ_c, $J = 1/2$ baryon states as function of T/T_C.

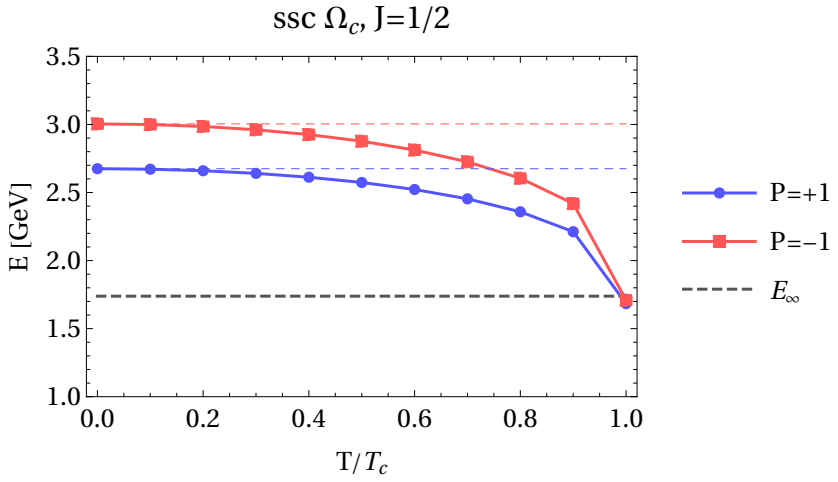

Figure 9.5: Energy of the negative and positive parity Ω_c, $J = 1/2$ baryon states as function of T/T_C.

We can conclude that the flattening of the linear part of the potential leads to a decrease of a states energy. This will become important later when we come to the second temperature dependent model in Sec. 9.2, where both the Coulomb and the linear term will be affected by colour charge screening. We will find that in the second model the mass of some of the heavier baryon states will actually increase as we increase the effective temperature parameter, as we know this cannot be due to the flattening of the linear part of the potential, the increase in energy will occur due

to the change in the Coulomb part of the potential. This makes sense because only the heavier baryons will exhibit an increase in their energy, and these are the baryons whose form factor is relatively small, therefore, being more sensitive to the potential at small r which is Coulombic in nature and not the linear part which happens at large r.

In Fig. 9.6 we plot the energy of the ground and some of the excited states of the Λ_c baryon with $J^P = 1/2^+$ as a function of T/T_C. We see that all of them follow a similar pattern and all fall below the line which marks E_∞ as defined in Eq. (9.5).

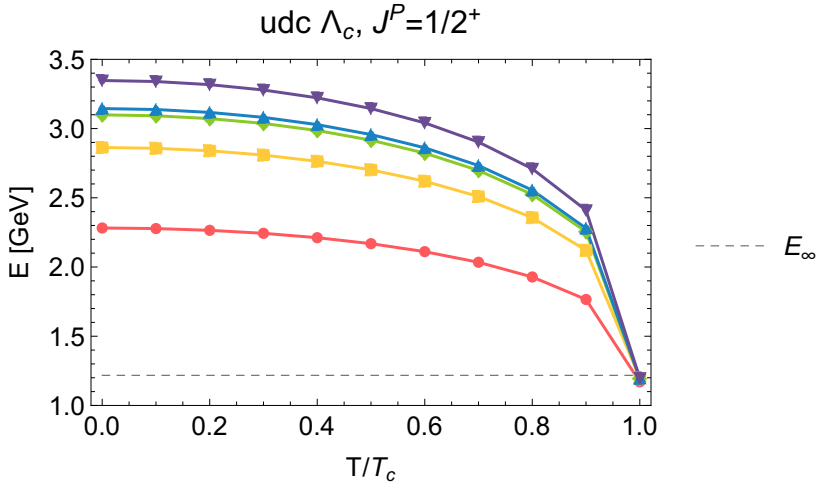

Figure 9.6: Energy of the ground and several excited states of the of the Λ_c baryon as a function of T/T_C.

9.2 Debye Mass Screened Potential

In this section we will present a second temperature dependent baryon model based on the potential proposed in Ref. [52]. Previously we have used this potential in our chapter on mesons at finite temperature in Sec. 8.2. We will describe the potential as well as obtain and discuss the predictions of various baryon observables as a function of the screening mass parameter $\mu(T)$.

9.2.1 Potential Description

The temperature dependence for this model will be completely contained by the screening/Debye mass parameter $\mu(T)$, where $\mu(T) = 1/r_D(T)$ and $r_D(T)$ is the inverse screening length [52]. There exists a vast literature space devoted to describing the relation between the Debye mass $\mu(T)$ and the physical temperature T, some examples include Refs. [71] and [72]. However, performing this translation is beyond the scope of this work, as such, we will express our observables as a function of $\mu(T)$. We will sometimes refer to $\mu(T)$ as an effective temperature parameter. Similarly as in Sec. 9.1 we will modify the baryon potential used in Ch. 7 to include effects of colour charge screening. The modified baryon potential is the following

$$V_{ij}^{q\bar{q}}(r_k) = \\ -\frac{\kappa}{r_k}e^{-\mu(T)r_k} + \frac{\sigma}{\mu(T)}(1 - e^{-\mu(T)r_k}) - K + \frac{8\kappa'}{3m_i m_j \pi^{1/2} r_0^3}\exp\big(-\tfrac{1}{r_0^2}r_k^2\big)\boldsymbol{S}_i \cdot \boldsymbol{S}_j, \quad (9.6)$$

where as usual $V_{ij}^{qq} = \frac{1}{2}V_{ij}^{q\bar{q}}$ and all the parameters of the temperature dependent potential are the same as the ones specified in Eq. (7.5). Unlike in the case of the simple temperature-dependent potential used in in Sec. 9.1, the critical point at which the state gets deconfined will have to be determined and will be different for each baryon state. The critical point will be determined as the point at which we can no longer find a minimum energy of a state. We have used the same method previously for meson in Sec. 8.2.2. We will revisit it for the baryon case in the section that follows. Another method for determining the critical point would be through the dissociation energy as has been proposed by Karsch et al. in Ref. [52]. For the baryon Hamiltonian with the potential specified in Eq. (9.1) the dissociation energy is defined as

$$E_{\text{dis}}(\mu) = \sum_{i=1}^{3} m_i + \frac{3}{2}\Big(\frac{\sigma}{\mu} - K\Big) - \frac{C}{m_1 m_2 m_3} - E(\mu), \quad (9.7)$$

which is the value of the potential at $r = \infty$ minus the energy of the baryon state $E(\mu)$ at effective temperature $\mu(T)$ obtained by diagonalising the Hamiltonian. For values of σ, K and C see the list of model parameters in Eq. (7.5). Critical temperature is then defined as

$$E_{\text{dis}}(\mu_c) = 0. \tag{9.8}$$

We can use Eq. (9.7) to plot the quantity

$$E_{\text{dis}}(\mu) + E(\mu) = \sum_{i=1}^{3} m_i + \frac{3}{2}\left(\frac{\sigma}{\mu} - K\right) - \frac{C}{m_1 m_2 m_3}, \tag{9.9}$$

which is the boundary between allowed bound states and dissociated states. We have illustrated the analogue of this quantity in the meson case, see Figs. 8.9 and 8.10. We will use $E_{\text{dis}} + E(\mu)$ as a guide to ensure that our primary method for determining μ_c works correctly. We should not find any states surviving above the boundary $E_{\text{dis}}(\mu) + E(\mu)$. For examples, see Figs. 9.9 $\rightarrow$ 9.12.

9.2.2 Results

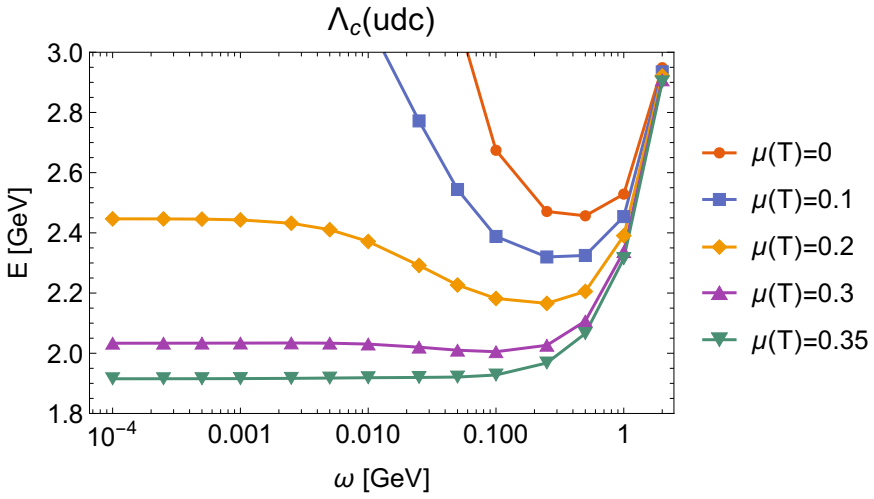

Figure 9.7: A plot of the Λ_c baryon ground state energies using the potential in Eq. (9.6) at different $\mu(T)$ as function of ω plotted on a log scale.

In Fig. 9.7 we illustrate our method for obtaining the critical value μ_c. We define μ_c as the the value of $\mu(T)$ for which there no longer exists a minimum in the E vs. ω curve. In the plot we see that at low values of $\mu(T)$ there exists a clear defined minimum energy. However, at $\mu(T) = 0.35\text{GeV}$, this is no longer the case, the energy continues to fall monotonically as ω decreases. Since at $\mu(T) = 0.35\text{GeV}$ we can no longer identify a minimum, the critical value of $\mu(T)$ must lie somewhere between $\mu(T) = 0.3\text{GeV}$ and $\mu(t) = 0.35\text{GeV}$.

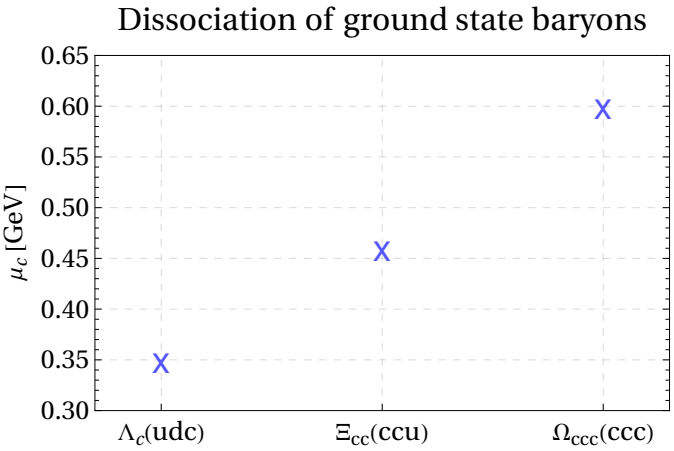

Figure 9.8: Determined critical screening mass for different charmed baryons

In Fig. 9.8 we plot the critical screening mass μ_c for different charmed baryons. We choose baryons which are only composed of up/down and charm quarks with increasing content of charm quarks. We see that as the number of charm quarks increases, so does the value μ_c at which the state melts. We can see that heavier states which are generally bound closer together tend to dissociate at higher $\mu(T)$ values.

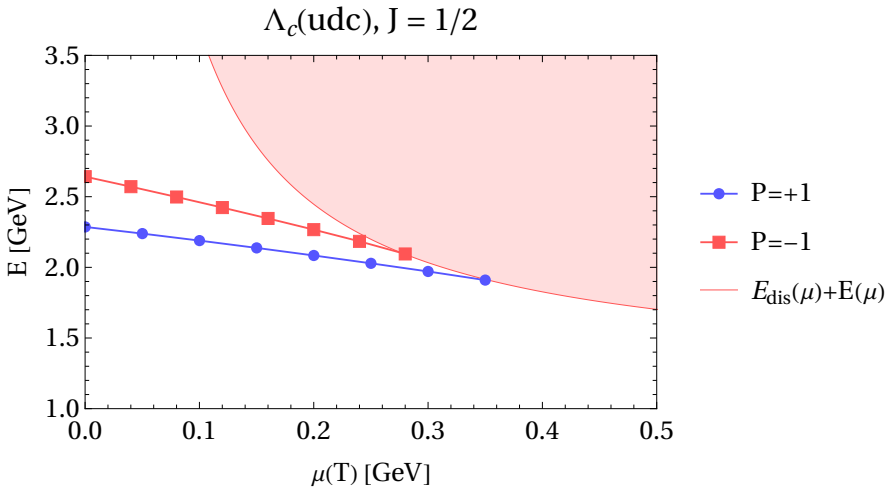

Figure 9.9: Mass of the positive and negative parity states of the Λ_c(udc) baryon with total angular momentum $J = \frac{1}{2}$ as a function of $\mu(T)$.

Next, in Figs. 9.9 $\rightarrow$ 9.12, we plot the mass of the positive and negative parity ground states for different baryons as a function of $\mu(T)$ up to critical screening mass μ_c. We find that our determined values of μ_c coincide very well with the dissociation energy curve defined in Eq. (9.9). We also find that for most states, their mass decreases as $\mu(T)$ increases. The exception is the Ω_{bbb} baryon whose mass actually increases for both the positive and negative parity states presented. This is a similar behaviour as we have seen with the heavy bottomonium meson ground state, whose mass also exhibited an increase as $\mu(T)$ increased, see Fig. 8.10. Another feature we see in Figs. 9.9 $\rightarrow$ 9.12 is that in all cases the negative parity ground states dissociate sooner than the positive parity ones.

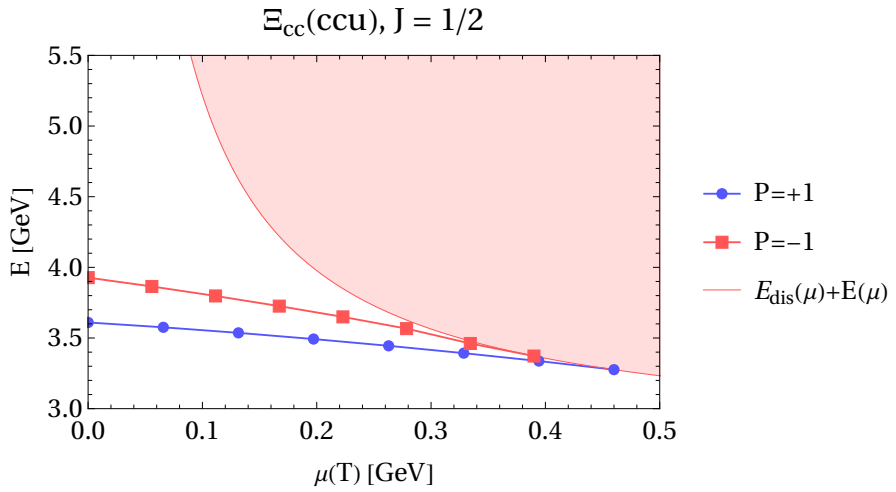

Figure 9.10: Mass of the positive and negative parity ground states of the $\Xi_{cc}(\mathrm{ccu})$ baryon with total angular momentum $J = \frac{1}{2}$ as a function of $\mu(T)$.

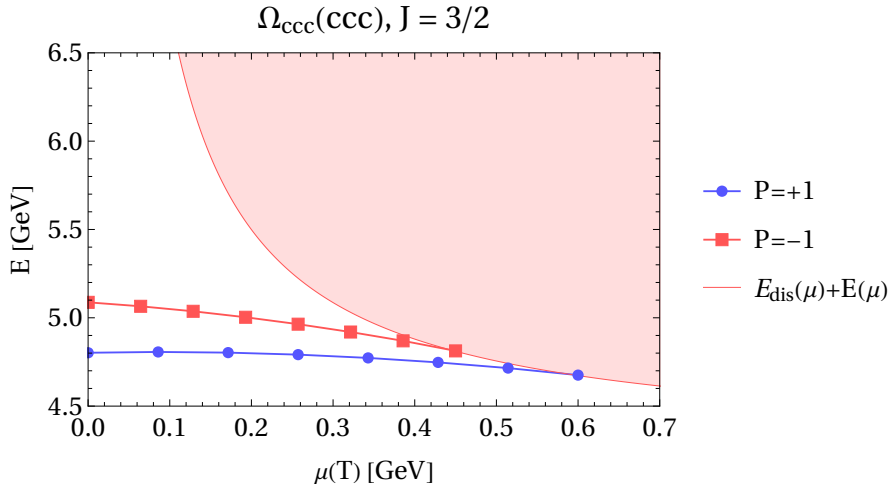

Figure 9.11: Mass of the positive and negative parity ground states of the Ω_{ccc} baryon with total angular momentum $J = \frac{3}{2}$ as a function of $\mu(T)$.

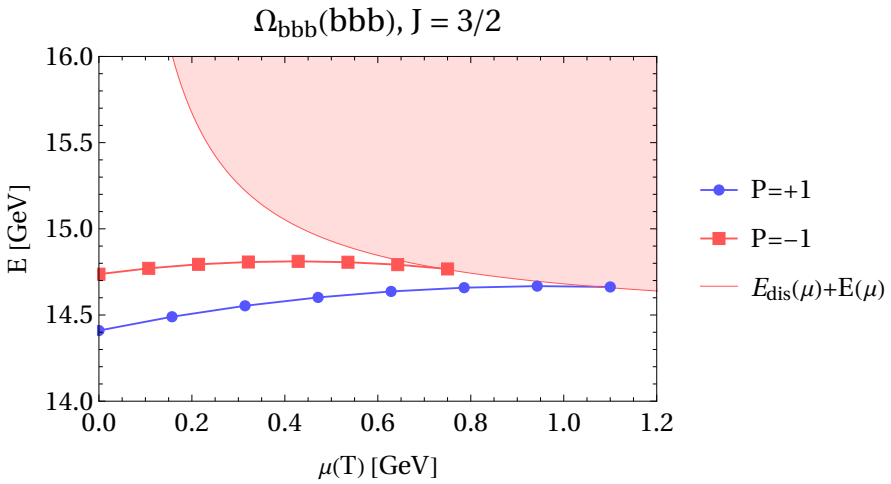

Figure 9.12: Mass of the positive and negative parity ground states of the Ω_{bbb} baryon with total angular momentum $J = \frac{3}{2}$ as a function of $\mu(T)$.

In Fig. 9.13 we plot the mass mean square radius $\langle R_m^2 \rangle$ as defined in Eq. (7.8) for three different charmed baryons as a function of $\mu(T)$. This observable is a good proxy for the overall size of the baryon [2]. We see that as expected, the size of the baryon increases as $\mu(T)$ increases until the baryon eventually becomes infinite in size which happens around the determined value of μ_c for each baryon.

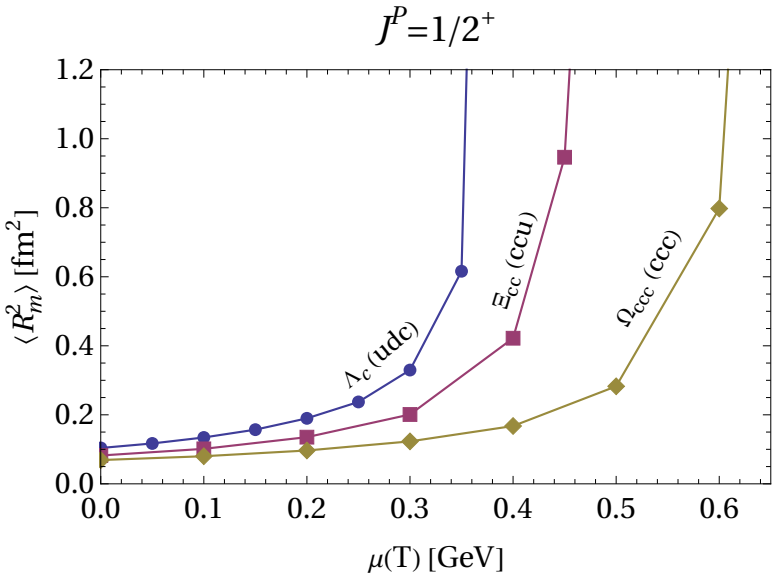

Figure 9.13: Mass mean square radius as defined in Eq. (7.8) for different charmed baryons as a function of $\mu(T)$.

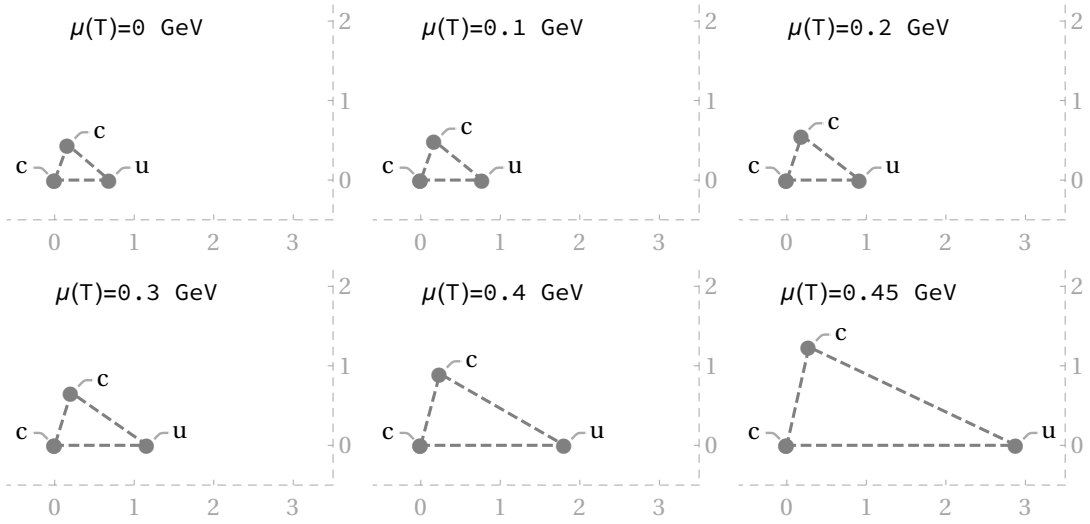

Figure 9.14: Shape of $\Xi_{cc}(\text{ccu})$, $J^P = 1/2^+$ ground state at different values of $\mu(T)$. The scale is in units of femtometers (fm).

In Fig. 9.14 we aim to illustrate the shape of the $\Xi_{cc}(\text{ccu})$, $J^P = 1/2^+$ baryon as we increase $\mu(T)$ up to just before μ_c. We do this by plotting the observable $\sqrt{\langle r_i^2 \rangle}$ which is the r.m.s. radius of each pair of quarks and we plot it in femtometers (fm) where each plot uses the same scale. We see that the state grows but we also see that the rate at which the cc pair of quarks separates is slower than the separation of the u quark from the c quarks. In other words, the cc pair seem to be bonded more tightly than a cu pair and are less sensitive to $\mu(T)$. We see this more clearly in Fig. 9.15 where we plot the distance between the two pairs of quarks (cc and cu), we see that the distance between the cu pairs grows faster than the distance between the cc pair as we increase $\mu(T)$.

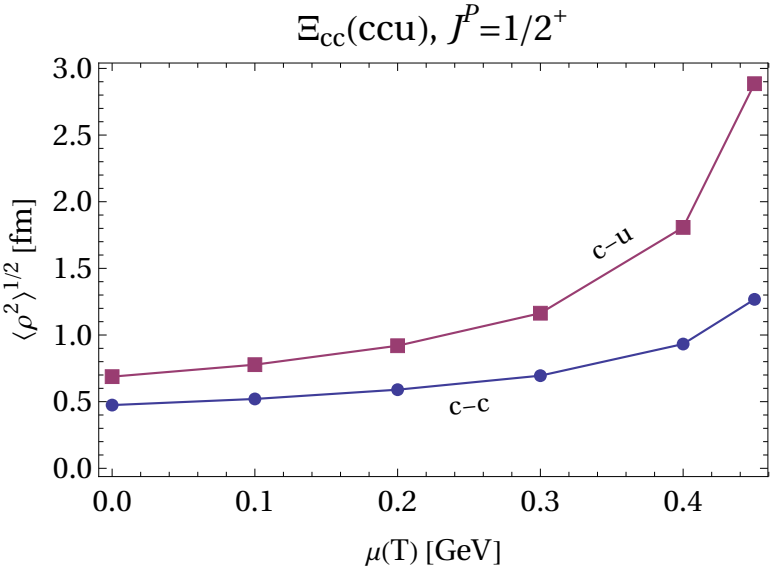

Figure 9.15: The separation between the two pairs of quarks (cc and cu) in the Ξ_{cc}(ccu) baryon as a function of $\mu(T)$ up to μ_c.

In Fig. 9.16, we illustrate the critical value of μ_c for different hadrons. This is our predicted order of melting of various hadrons inside the QGP. Given that the relation between μ_c and T can be obtained, this could potentially be used as a thermometer for the quark-gluon plasma. To make the plot more readable, we staggered the lines which mark the μ_c values of hadrons. We only show the μ_c values of ground state baryons $J^P = \frac{1}{2}^+$ for the $\Lambda_c(udc)$ and $\Xi_{cc}(ucc)$ baryons, and $J^P = \frac{3}{2}^+$ for the Ω_{ccc} and Ω_{bbb} baryons. We only show the μ_c values of spin-averaged meson states, obtained earlier in Ch. 8. Our "thermometer" should however only be treated as a toy model since the potential models used to obtained these quantities are somewhat naive in that they do not take into account any relativistic corrections and the interquark models are based on our understanding of colour screening in the 1980s, it would be interesting to produce a similar plot with more up to date models including relativistic corrections to the energy, as it has been shown in Tab. 8.4, they can quite significantly influence the dissociation energy of hadrons.

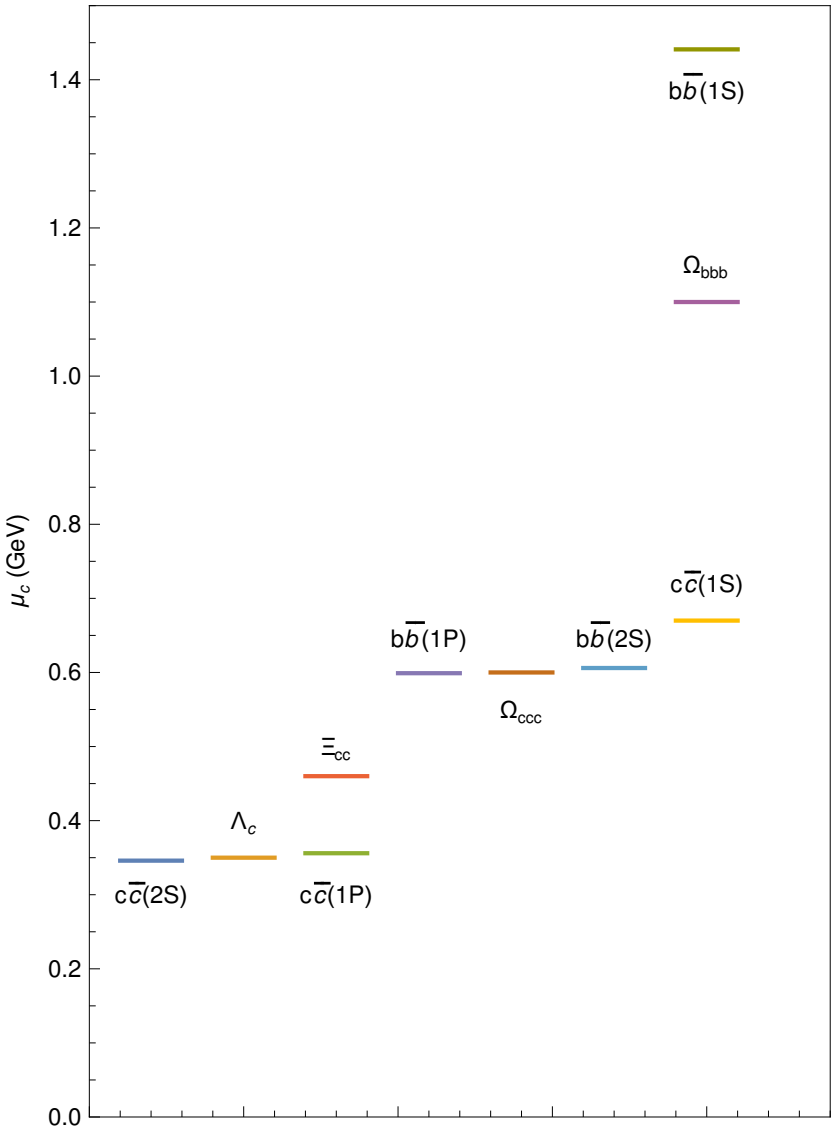

Figure 9.16: The critical value of μ_c obtained using our numerical method for various ground baryon and some excited meson states.

This concludes our chapter on baryons at finite temperature. Comparing our results to mesons at finite temperature we find that the baryons exhibit similar behaviour to mesons. We can conclude that the variational approach together with the Talmi-transformations provides a very effective method for solving three-body problems.

10 Conclusion

The goal of our work was to study hadrons at finite temperature using potential models. We implemented our own version of the variational method which has also been proposed by Silvestre et al. in Ref. [1]. It is one of many methods used to numerically solve three-body potential models. We extended this method to include the spin degrees of freedom as well as used it to study temperature and spin-dependent non-relativistic baryon potential models. In this thesis, a very general and useful methodology has been developed to study a large range of three-body potential models which include spin interactions. We demonstrated our method for building symmetrised spin-space basis sets necessary to satisfy the Pauli exclusion principle for baryon systems with zero, two and three identical quarks.

In Ch. 9, using the variational method, we solved two different temperature-dependent baryon potential models with a spin-spin hyperfine interaction term. We investigated how the mass and the size/shape of baryons change in the two potential models due to temperature effects. We also developed a method for determining the critical point at which a baryon state deconfines, determined by the value $\mu(T)$ at which a minimum energy of a state no longer exists. This method is specific to the variational method and potentials described in Secs. 8.2 and 9.2. In our analysis, we observed that the energies of most baryons decrease as they tend towards deconfinement, with the exception of very heavy and low lying states whose energy in fact increases as a

function of $\mu(T)$. We found that heavier, lower lying states tend to be less sensitive to the effects of colour charge screening. The baryon bound state radii become larger as temperature increases in all cases. We also found that heavier, lower lying baryon states deconfine at higher values of $\mu(T)$.

One current limitation of our work is the ability to compare results with lattice QCD simulations. For this, we still need a way of relating the screening mass parameter $\mu(T)$ present in potentials used in Secs. 8.2 and 9.2, directly to a temperature parameter T. Those relations have previously been considered and there exists a large body of literature dedicated to this problem, some examples that deal with this can be found in [60, 71–74]. However, due to time constraints we have not been able to make that link possible.

Future work could focus on bridging the gap between lattice QCD simulations and $\mu(T)$-dependent potential models used in this work. Furthermore, including the spin-orbit and tensor terms in the baryon potential, would allow us to better understand the baryon spectrum at finite temperature, those terms can be added with very little changes to the current method used in this work. It would also be good to calculate the root mean square of the velocity operator as a fraction of the speed of light $\langle v^2 \rangle^{1/2}/c$ for different systems, this would allow us to investigate the validity of the non-relativistic limit, particularly important for lighter hadrons.

Furthermore, for some time now, the focus of potential models at finite temperature has shifted towards models which go beyond $T = T_C$, it would be interesting to see if we could study these models using the variational method.

References

[1] B. Silvestre-Brac et al. "Quantum three body problems using harmonic oscillator bases with different sizes". In: (2020). arXiv: 2003.11028 [quant-ph].

[2] B. Silvestre-Brac. "Spectrum and static properties of heavy baryons". In: *Few Body Syst.* 20 (1996), pp. 1–25.

[3] Jia-Jun Wu et al. "Nucleon Excited States from Lattice QCD and Hamiltonian Effective Field Theory". In: (2018).

[4] J. Kogut and Leonard Susskind. "Vacuum polarization and the absence of free quarks in four dimensions". In: *Phys. Rev. D* 9 (12 1974), pp. 3501–3512.

[5] E. Eichten et al. "Spectrum of Charmed Quark-Antiquark Bound States". In: *Phys. Rev. Lett.* 34 (6 1975), pp. 369–372.

[6] Eve Kovacs. "Lattice predictions for the interquark potential". In: *16th Rencontres de Moriond: Session 2: New Flavours and Hadron Spectroscopy*. 1981, pp. 45–51.

[7] E. Eichten et al. "Charmonium: Comparison with Experiment". In: *Phys. Rev. D* 21 (1980), p. 203.

[8] John L. Richardson. "The Heavy Quark Potential and the Upsilon, J/psi Systems". In: *Phys. Lett. B* 82 (1979), pp. 272–274.

[9] C. Quigg and Jonathan L. Rosner. "Inverse Scattering and the Υ Family". In: *AIP Conf. Proc.* 68 (1981). Ed. by Loyal Durand and Lee G. Pondrom, pp. 719–724.

[10] D. B. Lichtenberg and J. G. Wills. "Heavy Meson Spectra With a New Phenomenological Potential". In: *Nuovo Cim. A* 47 (1978), p. 483.

[11] E. Eichten and Frank L. Feinberg. "Spin-Dependent Forces in Heavy-Quark Systems". In: *Phys. Rev. Lett.* 43 (17 1979), pp. 1205–1208.

[12] Ted Barnes. "A Strangeonium Potential Model With Complete Sigma (v^2/c^2) Hyperfine Splittings". In: *Z. Phys. C* 11 (1981), p. 135.

[13] Suraj N. Gupta, Stanley F. Radford, and Wayne W. Repko. "Quarkonium spectra and quantum chromodynamics". In: *Phys. Rev. D* 26 (11 1982), pp. 3305–3308.

[14] R. K. Bhaduri, L. E. Cohler, and Y. Nogami. "A Unified Potential for Mesons and Baryons". In: *Nuovo Cim. A* 65 (1981), pp. 376–390.

[15] Gunnar S. Bali, Klaus Schilling, and Armin Wachter. "Complete $O(v^2)$ corrections to the static interquark potential from SU(3) gauge theory". In: *Phys. Rev. D* 56 (5 1997), pp. 2566–2589.

[16] Li Bai-Qing and Chao Kuang-Ta. "Bottomonium Spectrum with Screened Potential". In: *Communications in Theoretical Physics* 52.4 (2009), 653–661.

[17] Suraj N. Gupta, Stanley F. Radford, and Wayne W. Repko. "Semirelativistic potential model for charmonium". In: *Phys. Rev. D* 31 (1 1985), pp. 160–163.

[18] L. P. Fulcher. "Matrix representation of the nonlocal kinetic energy operator, the spinless Salpeter equation and the Cornell potential". In: *Phys. Rev. D* 50 (1994), pp. 447–453.

[19] Alan J. Sommerer et al. "Relativistic meson spectroscopy and in-medium effects". In: *Physics Letters B* 348.3-4 (1995), pp. 277–282.

[20] Suraj N. Gupta and James M. Johnson. "B_c spectroscopy in a quantum-chromodynamic potential model". In: *Physical Review D* 53.1 (1996), pp. 312–314.

[21] D. Ebert, R. N. Faustov, and V. O. Galkin. "Properties of heavy quarkonia and B_c mesons in the relativistic quark model". In: *Phys. Rev. D* 67 (1 2003), p. 014027.

[22] "Observation of new Ω_c^0 states decaying to the $\Xi_c^+ K^-$ final state". In: (2023). arXiv: `2302.04733 [hep-ex]`.

[23] Si-Qiang Luo and Xiang Liu. "Newly observed Ωc(3327): A good candidate for a D-wave charmed baryon". In: *Phys. Rev. D* 107.7 (2023), p. 074041. arXiv: 2303.04022 [hep-ph].

[24] Nathan Isgur and Gabriel Karl. "P-wave baryons in the quark model". In: *Phys. Rev. D* 18 (11 1978), pp. 4187–4205.

[25] Nathan Isgur and Gabriel Karl. "Ground-state baryons in a quark model with hyperfine interactions". In: *Phys. Rev. D* 20 (5 1979), pp. 1191–1194.

[26] B F Tynemouth. "Spin-dependent hyperfine interactions in the positive-parity non-strange excited baryons". In: *Journal of Physics G: Nuclear Physics* 9.5 (1983), p. 497.

[27] W. Roberts and Muslema Pervin. "Heavy baryons in a quark model". In: *International Journal of Modern Physics A* 23.19 (2008), pp. 2817–2860. eprint: https://doi.org/10.1142/S0217751X08041219.

[28] Zhen-Yang Wang et al. "Spectra of charmed and bottom baryons with hyperfine interaction*". In: *Chinese Physics C* 41.9 (2017), p. 093103.

[29] Xin-Zhen Weng, Xiao-Lin Chen, and Wei-Zhen Deng. "Masses of doubly heavy-quark baryons in an extended chromomagnetic model". In: *Phys. Rev. D* 97 (5 2018), p. 054008.

[30] Ming-Sheng Liu, Qi-Fang Lü, and Xian-Hui Zhong. "Triply charmed and bottom baryons in a constituent quark model". In: *Phys. Rev. D* 101.7 (2020), p. 074031. arXiv: 1912.11805 [hep-ph].

[31] Nasrin Salehi and Afsaneh Abareshi. "A new approach for triply heavy Ω_{ccc} and Ω_{bbb} baryons spectroscopy in the nonrelativistic quark model". In: *Eur. Phys. J. Plus* 137.12 (2022), p. 1298.

[32] D. B. Lichtenberg et al. "Baryon Masses in a Relativistic Quark - Diquark Model". In: *Phys. Rev. Lett.* 48 (1982), p. 1653.

[33] J. L. Basdevant and S. Boukraa. "Baryon masses in relativistic potential models". In: *Zeitschrift fur Physik C Particles and Fields* 30.1 (1986), pp. 103–114.

[34] R. N. Faustov and V. O. Galkin. "Triply heavy baryon spectroscopy in the relativistic quark model". In: *Phys. Rev. D* 105.1 (2022), p. 014013. arXiv: 2111.07702 [hep-ph].

[35] H Satz. "The Transition from Hadron Matter to Quark-Gluon Plasma". In: *Annual Review of Nuclear and Particle Science* 35.1 (1985), pp. 245–270. eprint: https://doi.org/10.1146/annurev.ns.35.120185.001333.

[36] Gert Aarts et al. "Nucleons and parity doubling across the deconfinement transition". In: *Phys. Rev. D* 92.1 (2015), p. 014503. arXiv: 1502.03603 [hep-lat].

[37] Gert Aarts et al. "Light baryons below and above the deconfinement transition: medium effects and parity doubling". In: *JHEP* 06 (2017), p. 034. arXiv: 1703.09246 [hep-lat].

[38] Gert Aarts et al. "Hyperons in thermal QCD: A lattice view". In: *Phys. Rev. D* 99.7 (2019), p. 074503. arXiv: 1812.07393 [hep-lat].

[39] G. Aarts et al. "Properties of the QCD thermal transition with Nf=2+1 flavors of Wilson quark". In: *Phys. Rev. D* 105.3 (2022), p. 034504. arXiv: 2007.04188 [hep-lat].

[40] Gert Aarts et al. "Open charm mesons at nonzero temperature: results in the hadronic phase from lattice QCD". In: (2022). arXiv: 2209.14681 [hep-lat].

[41] H R Schmidt and Jürgen Schükraft. "The physics of ultra-relativistic heavy-ion collisions". In: *J. Phys. G* 19 (1993), pp. 1705–1796.

[42] Jurgen Schukraft and Reinhard Stock. "Toward the Limits of Matter: Ultra-relativistic nuclear collisions at CERN". In: *Adv. Ser. Direct. High Energy Phys.* 23 (2015), pp. 61–87. arXiv: 1505.06853 [nucl-ex].

[43] Ulrich W. Heinz and Maurice Jacob. "Evidence for a new state of matter: An Assessment of the results from the CERN lead beam program". In: (2000). arXiv: nucl-th/0002042.

[44] I. Arsene et al. "Quark gluon plasma and color glass condensate at RHIC? The Perspective from the BRAHMS experiment". In: *Nucl. Phys. A* 757 (2005), pp. 1–27. arXiv: nucl-ex/0410020.

[45] B.B. Back et al. "The PHOBOS perspective on discoveries at RHIC". In: *Nuclear Physics A* 757.1 (2005). First Three Years of Operation of RHIC, pp. 28–101.

[46] J. Adams et al. "Experimental and theoretical challenges in the search for the quark–gluon plasma: The STAR Collaboration's critical assessment of the evidence from RHIC collisions". In: *Nuclear Physics A* 757.1 (2005). First Three Years of Operation of RHIC, pp. 102–183.

[47] K. Adcox et al. "Formation of dense partonic matter in relativistic nucleus-nucleus collisions at RHIC: Experimental evaluation by the PHENIX collaboration". In: *Nucl. Phys. A* 757 (2005), pp. 184–283. arXiv: nucl-ex/0410003.

[48] T. Matsui and H. Satz. "J/ψ Suppression by Quark-Gluon Plasma Formation". In: *Phys. Lett. B* 178 (1986), pp. 416–422.

[49] M. C. Abreu et al. "J/ψ and ψ' production in the NA38 experiment". In: *29th Rencontres de Moriond: QCD and High-energy Hadronic Interactions*. 1994, pp. 639–644.

[50] J. Tran Thanh Van, ed. *Hadrons, quarks and gluons. proceedings, hadronic session of the 22nd Recontres de Moriond, les arcs, France, March 15-21, 1987*. Gif-Sur-Yvette: Ed. Frontieres, 1987.

[51] Helmut Satz. "Colour screening in SU(N) gauge theory at finite temperature". In: *Nuclear Physics A* 418 (1984), pp. 447–465.

[52] F. Karsch, M. T. Mehr, and H. Satz. "Color Screening and Deconfinement for Bound States of Heavy Quarks". In: *Z. Phys. C* 37 (1988), p. 617.

[53] Hans Joos and Istvan Montvay. "The screening of colour charge in the numerical hopping-parameter expansion". In: *Nuclear Physics* 225 (1983), pp. 565–578.

[54] P. W. M. Evans, C. R. Allton, and J.-I. Skullerud. "Ab initio calculation of finite-temperature charmonium potentials". In: *Phys. Rev. D* 89 (7 2014), p. 071502.

[55] Chris Allton et al. "The Charmonium Potential at Non-Zero Temperature". In: (2015). arXiv: 1505.06616 [hep-lat].

[56] Thomas Spriggs et al. "Thermal interquark potentials for bottomonium using NRQCD from the HAL QCD method". In: *PoS* LATTICE2021 (2022), p. 569. arXiv: 2112.09092 [hep-lat].

[57] Taesoo Song, Kyong Chol Han, and Che Ming Ko. "Charmonium production in relativistic heavy-ion collisions". In: *Phys. Rev. C* 84 (3 2011), p. 034907.

[58] Su Houng Lee et al. "Free energy versus internal energy potential for heavy-quark systems at finite temperature". In: *Phys. Rev. D* 89 (9 2014), p. 094015.

[59] Philipp Gubler, Taesoo Song, and Su Houng Lee. "D meson mass and heavy quark potential at finite temperature". In: *Phys. Rev. D* 101 (11 2020), p. 114029.

[60] Peng Cheng et al. "Calculation of dissociation temperature of nucleon using Gaussian expansion method". In: *Phys. Rev. D* 98 (11 2018), p. 116010.

[61] Abu-Shady, M. and Ikot, A. N. "Dissociation of nucleon and heavy baryon in an anisotropic hot and dense QCD medium using Nikiforov-Uvarov method". In: *Eur. Phys. J. Plus* 135.5 (2020), p. 406.

[62] David J. Griffiths and Darrell F. Schroeter. *Introduction to Quantum Mechanics*. 3rd ed. Cambridge University Press, 2018.

[63] B.H. Bransden and C.J. Joachain. *Quantum Mechanics*. Prentice Hall, 2000. ISBN: 9780582356917.

[64] I.S. Gradshteyn and I.M. Ryzhik. *Table of Integrals, Series, and Products*. Seventh Edition. Boston: Academic Press, 2007, pp. 247–617. ISBN: 978-0-12-373637-6.

[65] Igal Talmi. *Nuclear spectroscopy with harmonic oscillator wave-functions*. Basel, 1952.

[66] B. Buck and A.C. Merchant. "A simple expression for the general oscillator bracket". In: *Nuclear Physics A* 600.3 (1996), pp. 387 –402.

[67] D.A. Varshalovich, A.N. Moskalev, and V.K. Khersonskii. *Quantum Theory of Angular Momentum: Irreducible Tensors, Spherical Harmonics, Vector Coupling Coefficients, 3nj Symbols*. World Scientific, 1988. ISBN: 9789971509965.

[68] Robert D. Pisarski and Orlando Alvarez. "Strings at Finite Temperature and Deconfinement". In: *Phys. Rev. D* 26 (1982), p. 3735.

[69] Yu-Bing Dong. "Study of the relativistic effect on heavy quarkonium properties in a thermal environment". In: *J. Phys. G* 22 (1996), pp. 591–599.

[70] Bo Liu and Yu-Bing Dong. "Quark binding potential and Debye screening length". In: *Commun. Theor. Phys.* 26 (1996), pp. 425–432.

[71] Yannis Burnier and Alexander Rothkopf. "Complex heavy-quark potential and Debye mass in a gluonic medium from lattice QCD". In: *Physical Review D* 95.5 (2017).

[72] M. Laine, P. Schicho, and Y. Schröder. "A QCD Debye mass in a broad temperature range". In: *Physical Review D* 101.2 (2020).

[73] Mujeeb Hasan et al. "Landau Damping in a strong magnetic field: Dissociation of Quarkonia". In: *Nuclear Physics A* 995 (2018).

[74] M. Abu-shady, Taha Abdel-Karim, and Emad Khokha. "Binding Energies and Dissociation Temperatures of Heavy Quarkonia at Finite Temperature and

Chemical Potential in the N -Dimensional Space". In: *Advances in High Energy Physics* 2018 (2018).